

**INFLUENCE OF CHEMICAL AND PHYSICAL PROPERTIES OF
POORLY-ORDERED SILICA ON REACTIVITY AND RHEOLOGY OF
CEMENTITIOUS MATERIALS**

by

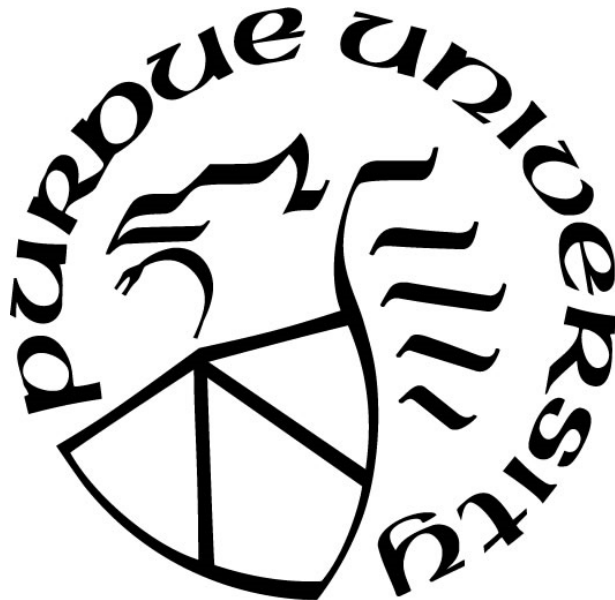
Jedediah F. Burroughs

A Dissertation

Submitted to the Faculty of Purdue University

In Partial Fulfillment of the Requirements for the degree of

Doctor of Philosophy



Lyles School of Civil Engineering

West Lafayette, Indiana

December 2019

**THE PURDUE UNIVERSITY GRADUATE SCHOOL
STATEMENT OF COMMITTEE APPROVAL**

Dr. John E. Haddock, Chair

Lyles School of Civil Engineering

Dr. Luna Lu

Lyles School of Civil Engineering

Dr. Jan Olek

Lyles School of Civil Engineering

Dr. Jameson D. Shannon

Geotechnical and Structures Laboratory, U.S. Army Engineer Research and
Development Center

Dr. W. Jason Weiss

School of Civil and Construction Engineering, Oregon State University

Approved by:

Dr. Dulcy M. Abraham

Head of the Graduate Program

*To Griffin, Riley, and ones we have not met yet
Keep the faith, work hard, and chase your dreams*

ACKNOWLEDGMENTS

First, I would like to say thank you to Jesus Christ for blessing me with the opportunity to pursue this degree. I know that nothing happens outside Your purview, and I am thankful for the many blessings You bestow upon me each day. I would also like to thank everyone who has spent time in prayer for me during this process. It is impossible to know everyone who lifted me up during this time, but I am grateful you did.

I would like to thank the U.S. Army Engineer Research and Development Center for selecting me to participate in the long-term training program, without which this opportunity would not be possible. I know many qualified candidates apply for this opportunity each year, and I am grateful that you chose me. To the Board of Directors of the Geotechnical and Structures Laboratory, thank you for the continued guidance and support through this process. Thank you for holding the internal program reviews every six months to remind me the need to continue progressing each day.

I would like to thank my advisors, Prof. John Haddock and Prof. Jason Weiss, for their diligent work and guidance through this entire process. Thank you for putting up with me and my nonlinear trains of thought. Thank you for supporting me during this degree program, even though things followed a nontraditional route. I would also like to thank my committee of Prof. Jan Olek, Prof. Luna Lu, and Dr. Jameson Shannon for their helpful discussions and suggestions as to how to improve this research.

I would have never had the opportunity to pursue this doctorate without the foundation that was laid by my undergraduate and master's degrees at the University of Alabama. I would like to thank all the professors along the way who challenged and motivated me to think about engineering in a different way. I would especially like to thank Prof. Michael Triche, Prof. Jim Richardson, and Prof. Jialai Wang for everything you did for me along the way. Thank you and Roll Tide!

Thank you to all my other colleagues at the Concrete and Materials Branch who have helped me along the way. To Dr. Charles Weiss, Dr. Todd Rushing, and Chris Moore, thank you for your mentorship and encouragement over the last few years, even before I ever applied to Purdue. Your experiences and expertise have proven invaluable to me. Thank you to Brian Green and Dr. Robert Moser for being sounding boards and reality checks for all of my crazy ideas. To all of you who helped with experimentation and data collection, I say thank you. I will surely forget someone if I try to list everyone, but I truly appreciate everyone's assistance.

My experience at Purdue would not have been nearly as fulfilling if it were not for everyone from East Tipp Baptist Church under the leadership of Bro. Joel Flowers. To Stan and Lucinda Turlo, thank you for all you did for me while I was in Indiana. You have a beautiful family, and you made me feel at home.

I am nothing without my family, so I would like to thank my father Phil and mother Patti for your continued support. I know you have sacrificed to provide me with opportunities you could not have yourself. I hope I have made you proud. To my brother Andrew, you know you are my

best friend in the world, and I could not have done this without you. Thank you for all of the hours on the phone talking about absolutely nothing that helped to keep me sane through this entire process. I know I may not be the best at saying it, but I love each one of you and cannot imagine my life without you.

Lastly, to my wife Mindi, I could never fully express what you mean to me. You have a way of giving me the words of support and encouragement exactly when I need them. You have supported me through all the positive and negative emotions I have had during this roller coaster ride. I love you more and more each day.

This work was funded under the U.S. Army Basic Research Program under PE 61102, Project T22, Task 02, “Material Modeling for Force Protection,” and was managed and executed at the U.S. Army Engineer Research and Development Center. Permission to publish was granted by the Director, Geotechnical and Structures Laboratory.

TABLE OF CONTENTS

LIST OF TABLES.....	10
LIST OF FIGURES	11
LIST OF SYMBOLS	13
ABSTRACT.....	16
1. INTRODUCTION	19
1.1 Motivation.....	19
1.2 Pilot Study.....	20
1.3 Literature Review.....	23
1.3.1 Historical Perspective	23
1.3.2 Industry Perspective.....	24
1.3.3 Academic Perspective.....	24
1.3.4 Commentary	28
2. MATERIALS CHARACTERIZATION.....	29
2.1 Material Types	29
2.1.1 Cement.....	29
2.1.2 Inert Aggregates/Fillers	29
2.1.3 Silica Fumes.....	29
2.1.4 High-Range Water Reducing Admixtures.....	30
2.1.5 Mix Water.....	31
2.2 Characterization Methods.....	31
2.2.1 Physical Characterization	31
2.2.1.1 Specific Gravity.....	31
2.2.1.2 Bulk Density	32
2.2.1.3 Particle Size Analysis	33
2.2.1.4 Specific Surface Area	33
2.2.1.5 Absorption Capacity.....	35
2.2.1.5.1 Statistical Approximation.....	36
2.2.1.5.2 Atmospheric Absorption.....	37
2.2.1.5.3 Vacuum Filtration	38

2.2.1.5.4	Dynamic Vapor Sorption	40
2.2.2	Chemical Characterization.....	41
2.2.2.1	X-Ray Diffraction.....	41
2.2.2.2	X-Ray Fluorescence	42
2.2.2.3	Loss on Ignition	43
2.3	Characterization Results	44
2.3.1	Class H Cement	44
2.3.2	Silica Sand	45
2.3.3	Silica Powder	46
2.3.4	Silica Fumes.....	47
2.3.4.1	SF1	52
2.3.4.2	SF2.....	54
2.3.4.3	SF3.....	56
2.3.4.4	SF4.....	58
2.3.4.5	SF5.....	60
2.3.4.6	SF6.....	62
2.3.4.7	SF7.....	64
2.3.4.8	SF8.....	66
2.4	Conclusions.....	68
3.	HYDRATION EFFECTS.....	70
3.1	Calorimetry Experiments	70
3.2	Hydration Modeling.....	76
3.2.1	Powers-Brownyard Model Expansion.....	76
3.2.2	Reduction of Surface Area.....	81
3.2.3	Paste Thickness Model	83
3.2.3.1	Comparison to Similar Models.....	84
3.3	Application of Paste Thickness Model	85
3.3.1	Comparing Paste Thickness Model with Experimental Results.....	86
3.3.2	Discussion of Results.....	87
3.4	Conclusions.....	89
4.	MULTILINEAR RHEOLOGICAL MODEL	91

4.1	Rheological Experiments	91
4.1.1	Methodology	91
4.1.2	Herschel-Bulkley Model.....	94
4.1.3	Rheological Testing Results	95
4.2	Model Development.....	97
4.3	Model Validation	98
4.4	Conclusions.....	100
5.	WATER THICKNESS MODEL.....	101
5.1	Introduction.....	101
5.2	Model Development.....	102
5.2.1	Comparison to Existing Models	104
5.3	Comparison of Experimental and Analytical Results.....	104
5.4	Conclusions.....	108
6.	CONCLUSIONS	109
6.1	Project Summary.....	109
6.2	Recommended Future Work.....	110
	APPENDIX A. PRELIMINARY STUDY	111
	APPENDIX B. QUANTITATIVE XRD WHOLE PATTERN FITS	120
	APPENDIX C. DYNAMIC VAPOR SORPTION ANALYSIS	140
	APPENDIX D. POWERS-BROWNYARD HYDRATION MODEL RESULTS.....	141
	REFERENCES	155

LIST OF TABLES

Table 1.1. Chemical composition of silica fumes used in pilot study	21
Table 1.2. Bench-scale planetary mixing results	22
Table 2.1. Silica fumes studied.....	30
Table 2.2. Example calculation for statistical approximation of absorption capacity	37
Table 2.3. XRF scan parameters.....	43
Table 2.4. Class H cement characterization results	45
Table 2.5. Silica sand characterization results.....	46
Table 2.6. Silica powder characterization results	46
Table 2.7. Physical characterization data for silica fumes.....	48
Table 2.8. Absorption capacity estimates by mass for silica fumes	49
Table 2.9. Relative ranks of absorption capacity estimates	50
Table 2.10. Amorphous content of silica fumes from quantitative XRD	51
Table 2.11. Chemical composition of silica fumes.....	52
Table 3.1. Idealized pozzolanic reactivity mixture proportion.....	70
Table 3.2. Bogue composition of Class H cement.....	78
Table 3.3. Range of mixture proportions.....	86
Table 4.1. ANOVA for rheological testing.....	96
Table 4.2. Significance and regression coefficients for multilinear model	98
Table 4.3. Model validation mixtures with predicted rate indices.....	99
Table 5.1. Goodness-of-fit with and without absorption	105
Table 5.2. Comparison of goodness-of-fit at low and high coating thickness.....	108

LIST OF FIGURES

Figure 1.1. Particle size distributions for silica fumes used in pilot study	21
Figure 2.1. Atmospheric absorption test setup.....	38
Figure 2.2. Vacuum filtration setup	40
Figure 2.3. Representative data with DLP fits (left) and difference curve (right).....	41
Figure 2.4. Class H cement particle size distribution	44
Figure 2.5. Silica sand particle size distribution.....	45
Figure 2.6. Silica powder particle size distribution	46
Figure 2.7. Silica fume particle size distributions.....	47
Figure 2.8. Atmospheric absorption results	51
Figure 2.9. SF1.....	53
Figure 2.10. Dynamic vapor sorption data (left) and hysteresis area analysis (right) for SF1	53
Figure 2.11. XRD patterns for SF1	54
Figure 2.12. SF2.....	55
Figure 2.13. Dynamic vapor sorption data (left) and hysteresis area analysis (right) for SF2	55
Figure 2.14. XRD patterns for SF2.....	56
Figure 2.15. SF3.....	57
Figure 2.16. Dynamic vapor sorption data (left) and hysteresis area analysis (right) for SF3	57
Figure 2.17. XRD patterns for SF3.....	58
Figure 2.18. SF4.....	59
Figure 2.19. Dynamic vapor sorption data (left) and hysteresis area analysis (right) for SF4	59
Figure 2.20. XRD pattern for SF4	60
Figure 2.21. SF5.....	61
Figure 2.22. Dynamic vapor sorption data (left) and hysteresis area analysis (right) for SF5	61
Figure 2.23. XRD patterns for SF5.....	62
Figure 2.24. SF6.....	63
Figure 2.25. Dynamic vapor sorption data (left) and hysteresis area analysis (right) for SF6	63
Figure 2.26. XRD patterns for SF6.....	64

Figure 2.27. SF7.....	65
Figure 2.28. Dynamic vapor sorption data (left) and hysteresis area analysis (right) for SF7	65
Figure 2.29. XRD pattern for SF7	66
Figure 2.30. SF8.....	67
Figure 2.31. Representative dynamic vapor sorption data (left) and hysteresis area analysis (right) for SF8	67
Figure 2.32. XRD pattern for SF8	68
Figure 3.1. Normalized heat flow plots from isothermal calorimetry experiments.....	71
Figure 3.2. Heat flow comparison – SF1, SF2, SF5, and SF8	73
Figure 3.3. Normalized heat release from idealized pozzolanic reactivity tests.....	74
Figure 3.4. Comparison of specific surface area and cumulative heat release	75
Figure 3.5. Example phase diagrams from Powers-Brownyard Model for neat cement paste.....	79
Figure 3.6. Example phase diagrams from Powers-Brownyard Model for cement paste with 10% silica fume	80
Figure 3.7. Effect of silica fume content on α_{∞} for different w/c	81
Figure 3.8. Reduction of particle surface area with hydration.....	82
Figure 3.9. Evolution of specific surface area of cement and silica fume with hydration.....	83
Figure 3.10. Paste thickness model.....	87
Figure 3.11. Example of paste thickness evolution with hydration.....	88
Figure 4.1. High-shear mixing protocol.....	92
Figure 4.2. Example specimen loading and unloading curves.....	93
Figure 4.3. Rate index results	95
Figure 4.4. Multilinear rheological model fit.....	98
Figure 4.5. Multilinear model validation mixture results	99
Figure 5.1. Particles (shown in black) surrounded by volumes of fluid (shown in gray) decreasing from left to right.....	101
Figure 5.2. Relationship between rate index and coating thickness with (right) and without (left) absorption.....	105
Figure 5.3. Volume fractions of water categorized at early age as absorption (left) and coating (right) for SF1	106
Figure 5.4. Rheological results segmented by w/b and silica fume content.....	107

LIST OF SYMBOLS

A – absorption capacity
 $A_{s,bin}$ – surface area in each particle size bin, m^2
 $A_{s,cem,unh}$ – surface area of cement after adjusting for hydration, m^2
 $A_{s,particle}$ – surface area of an individual particle, m^2
 $A_{s,sf,unr}$ – surface area of silica fume after adjusting for reaction, m^2
 $A_{s,sp}$ – surface area of silica powder, m^2
 $A_{s,ss}$ – surface area of silica sand, m^2
 $A_{s,total}$ – total surface area in particle size distribution, m^2
 $A_{s,total,after\ hydration}$ – total surface area in mixture after adjusting for hydration, m^2
 $A_{s,2}$ – particle surface area after hydration, m^2
 $C\bar{S}$ – anhydrite
 C_2S – dicalcium silicate, a cementitious phase also known as belite
 C_3A – tricalcium aluminate, a cementitious phase
 C_3S – tricalcium silicate, a cementitious phase also known as alite
 C_4AF – tetracalcium aluminoferrite, a cementitious phase
DF – degrees of freedom
F – F-test statistic
 G_s – specific gravity
 L – cylinder length, m
MAE – mean absolute error
MS – mean square
P-value – probability
 P_{SF} – mass percentage of total binder that is silica fume
RH – relative humidity
RMSE – root-mean-squared error
 R_1 – inner cylinder radius, m
 R_2 – outer cylinder radius, m
SS – sums of squares
 SSA_{BET} – specific surface area as determined using the BET method, m^2/g
 SSA_{PSD} – specific surface area estimated from particle size distribution, m^2/g
 $V_{assumed}$ – assumed volume of particle size distribution, m^3
 V_c – volume fraction of unhydrated cement
 V_{cement} – volume of cement, m^3
 V_{cs} – volume fraction of chemical shrinkage
 V_{cw} – volume fraction of capillary water
 $V_{cw,total}$ – total volume of capillary water remaining, m^3
 V_{fume} – volume of silica fume, m^3
 V_{gs} – volume fraction of gel solids
 $V_{gs,total}$ – total volume of gel solids produced, m^3
 V_{gw} – volume fraction of gel water
 $V_{gw,total}$ – total volume of gel water produced, m^3

V_{hp} – volume fraction of hydration products
 $V_{hydration\ products}$ – total volume of hydration products produced, m^3
 $V_{particle}$ – volume of an individual particle, m^3
 $V_{paste,total}$ – total paste volume in mixture proportion, m^3
 V_s – volume fraction of unreacted silica fume
 V_{water} – volume of water, m^3
 $V_{water,absorbed}$ – total volume of water absorbed by particles, m^3
 $V_{water,absorbed,sf}$ – total volume of water absorbed by silica fume, m^3
 $V_{water,coating}$ – total volume of free water available to coat particle surfaces, m^3
 $V_{water,HRWRA}$ – total volume of water added as component of HRWRA, m^3
 $V_{water,mix}$ – total volume of water added as water in mixture proportion, m^3
 $V_{water,reaction}$ – total volume of water consumed by hydraulic reactions, m^3
 $V_{water,reaction,cem}$ – total volume of water consumed by hydraulic reaction of cement, m^3
 $V_{water,total}$ – total volume of water in mixture proportion, m^3
 V_1 – initial volume, m^3
 V_2 – final volume, m^3
 a_{AA} – absorption capacity estimated by atmospheric absorption
 a_{SA} – absorption capacity estimated by statistical approximation
 a_{DVS} – absorption capacity estimated by dynamic vapor sorption analysis
 $a_{VF,NM}$ – absorption capacity estimated by vacuum filtration without any additional mixing
 $a_{VF,S}$ – absorption capacity estimated by vacuum filtration after sonicating for 10 minutes
 $a_{VF,100}$ – absorption capacity estimated by vacuum filtration after mixing at 100 RPM for five minutes
 $a_{VF,200}$ – absorption capacity estimated by vacuum filtration after mixing at 200 RPM for five minutes
 $a_{VF,500}$ – absorption capacity estimated by vacuum filtration after mixing at 500 RPM for five minutes
 d – interplanar spacing of crystal lattice, nm
 $d_{particle}$ – diameter of an individual particle, m
 f_c – unconfined compressive strength, MPa
 f_{cement} = volume fraction of cement in mixture proportion
 f_{fume} = volume fraction of cement in mixture proportion
 f_{water} = volume fraction of water in mixture proportion
 f_{vol} – volume fraction in particle size distribution
 k – consistency, $Pa \cdot s^n$
 m – moisture content
 m_c – mass of cement, kg
 m_{HRWRA} – mass of HRWRA, kg
 $m_{required}$ – required mass of particle size distribution
 m_s – mass of silica fume, kg
 m_{sp} – mass of silica powder, kg
 m_{ss} – mass of silica sand, kg
 m_w – mass of water, kg
 n – Herschel-Bulkley rate index

n_{Bragg} – order of reflection
 $n_{measured}$ – rate index measured by rotational rheology
 $n_{particles}$ – number of particles in each size fraction
 $n_{predicted}$ – rate index predicted by multilinear model
 p_{solids} – percentage of solids
 r_{paste} – ratio of paste thickness of mixture proportion to paste thickness of reference proportion
 $r_{strength}$ – ratio of compressive strength of mixture proportion to compressive strength of reference proportion
 r_1 – initial radius, m
 r_2 – final radius, m
 $ss(C_4AF + C_2F)$ – a solid solution formed during the hydration of low alumina cements
 t_{flow} – thickness of water surrounding a particle, m
 t_{paste} – thickness of hydration product surrounding a particle, m
 w/b – water-to-binder ratio, where binder is both cement and silica fume
 w/c – water-to-cement ratio
 w/cm – water-to-cementitious materials ratio
 $w_{gw,c}$ – water trapped in gel pores due to cement hydration
 $w_{gw,s}$ – water trapped in gel pores due to silica fume reaction
 $w_{n,c}$ – nonevaporable water formed due to cement hydration
 $w_{n,s}$ – nonevaporable water formed due to silica fume reaction
 ΔV_c – change in volume due to cement hydration
 ΔV_s – change in volume due to silica fume reaction
 Γ – torque, N·m
 $\Phi_{volumetric}$ – volumetric porosity
 Ω_1 – rotational speed of inner cylinder, rad/s
 α – degree of hydration
 α_c – degree of hydration of cement
 α_r – degree of reaction of silica fume
 α_∞ – ultimate degree of hydration
 β_i – model coefficient
 $\dot{\gamma}$ – shear rate, s⁻¹
 λ – wavelength of incident wave, nm
 τ – shear stress, Pa
 τ_0 – yield stress, Pa
 θ – scattering angle
 ρ – density, kg/m³
 ρ_{bulk} – bulk density, kg/m³
 ρ_c – density of cement, kg/m³
 ρ_s – density of silica fume, kg/m³
 $\rho_{solid,required}$ – required density of solids, kg/m³
 ρ_w – density of water, kg/m³

ABSTRACT

Author: Burroughs, Jedadiah F. PhD

Institution: Purdue University

Degree Received: December 2019

Title: Influence of Chemical and Physical Properties of Poorly-Ordered Silica on Reactivity and Rheology of Cementitious Materials

Committee Chair: Dr. John E. Haddock

Silica fume is a widely used pozzolan in the concrete industry that has been shown to have numerous benefits for concrete including improved mechanical properties, refined pore structure, and densification of the interfacial transition zone between paste and aggregates. Traditionally, silica fume is used as a 5% to 10% replacement of cement; however, newer classes of higher strength concretes use silica fume contents of 30% or greater. At these high silica fume contents, many detrimental effects, such as poor workability and inconsistent strength development, become much more prominent.

In order to understand the fundamental reasons why high silica fume contents can have these detrimental effects on concrete mixtures, eight commercially available silica fumes were characterized for their physical and chemical properties. These included traditional properties such as density, particle size, and surface area. A non-traditional property, absorption capacity, was also determined. These properties or raw material characteristics were then related to the hydration and rheological behavior of pastes and concrete mixtures. Other tests were performed including isothermal calorimetry, which showed that each silica fume reacted differently than other silica fumes when exposed to the same reactive environment. Traditional hydration models

for ordinary portland cement were expanded to include the effects that silica fumes have on water consumption, volumes of hydration products, and final degree of hydration.

As a result of this research, it was determined necessary to account for the volume and surface area of unhydrated cement and unreacted silica fume particles in water-starved mixture proportions. An adjustment factor was developed to more accurately apply the results from hydration modeling. By combining the results from hydration modeling with the surface area adjustments, an analytical model was developed to determine the thickness of paste (hydration products and capillary water) that surrounds all of the inert and unreacted particles in the system. This model, denoted as the “Paste Thickness Model,” was shown to be a strong predictor of compressive strength results. The results of this research suggest that increasing the paste thickness decreases the expected compressive strength of concretes at ages or states of hydration.

The rheological behavior of cement pastes containing silica fume was studied using a rotational rheometer. The Herschel-Bulkley model was fit to the rheological data to characterize the rheological behavior. A multilinear model was developed to relate the specific surface area of the silica fume, water content, and silica fume content to the Herschel-Bulkley rate index. The Herschel-Bulkley rate index is practically related to the ease at which the paste mixes. This multilinear model was shown to have strong predictive capability when used on randomly generated paste compositions.

Additionally, an analytical model was developed that defines a single parameter, idealized as the thickness of water surrounding each particle in the cementitious system. This model, denoted as

the “Water Thickness Model,” incorporated the absorption capacity of silica fumes discovered during the characterization phase of this study and was shown to correlate strongly with the Herschel-Bulkley rate index. The Water Thickness Model demonstrates how small changes in water content can have a drastic effect on the rheology of low w/c or high silica fume content pastes due to the combined effects of surface area and absorption. The effect of additional water on higher w/c mixtures is significantly less.

1. INTRODUCTION

1.1 Motivation

The United States Army Engineer Research and Development Center (ERDC) has long been interested in ultra-high-performance concrete (UHPC). UHPCs routinely reach compressive strengths five to ten times greater than traditional concretes through the optimization of particle packing and a reduction in water-to-cementitious ratio (w/cm). To ensure that UHPCs reach their required mechanical properties, it is necessary to more deeply understand and control the constituent materials. UHPC constituent materials generally consist of cement, fine aggregates, micron-sized inert fillers, and silica fume/other supplementary cementitious materials (SCM). High dosages of high-range water-reducing admixtures (HRWRA) are generally necessary to reach the desired mechanical properties, and most UHPCs incorporate some type of fiber reinforcement to increase tensile properties and toughness.

With the ever-increasing need to be able to use regionally based materials for production, it has never been more important to understand what controls the utility of a constituent material in UHPCs. The focus of this study centered on the use of silica fume, a form of silica that generally exists as amorphous, porous spheres with diameters in the tens to hundreds of nanometers. Though it is available in many parts of the world, silica fume is an industrial byproduct rather than an engineered material; therefore, its composition varies depending on its source.

Depending on material availability, can one silica fume product successfully replace another with minimal effect on UHPC properties? If not, what adjustments to a baseline mixture

proportion are required to meet desired properties? If, after adjusting the mixture proportion, desired properties can still not be met, what characteristics of the silica fume product are limiting the development of the desired properties? What is the acceptable range of raw material properties that will allow for successful implementation into a UHPC so that an engineer can feel confident in the use of the UHPC? These are some of the questions that are to be answered in this research program, specifically with an eye towards silica fume and UHPC. Certainly, conclusions may have broader impact on the entire cementitious material portfolio, but the class of interest is UHPC.

1.2 Pilot Study

Portions of the following section contain text and/or figures and tables previously published in **J.F. Burroughs**, T.S. Rushing, D.A. Scott, and B.A. Williams, “Analyzing Effects of Varied Silica Fume Sources within Baseline UHPC,” in: *Proceedings of the First International Interactive Symposium on UHPC*, Des Moines, IA, 2016.

To begin to answer these questions posed above, a pilot study was performed by the ERDC in 2015 to understand how different silica fume sources performed in a baseline UHPC mixture proportion. In order to isolate the effects of different silica fume sources, all other constituent materials were left constant in the mixture proportion, and the silica fume sources were replaced using 1:1 replacement by mass. Eight silica fume sources were considered in this testing series, including both densified and undensified silica fumes. Basic chemical characterization was performed using x-ray fluorescence (XRF) spectroscopy, and particle size distributions were determined using laser diffraction. Chemical characterization results are shown in Table 1.1, and particle size distributions are shown in Figure 1.1. SF-1 in this study was used as a reference for which to compare all other silica fume results. With the exception of SF-4, all other silica fumes

tested were shown to be at 93% SiO₂, indicating high to very high purity fumes. SF-4 was chosen for study due to its unique chemical composition.

Table 1.1. Chemical composition of silica fumes used in pilot study

Silica Fume	SiO ₂ (%)	CaO (%)	MgO (%)	Na ₂ O (%)	Balance (%)	LOI (%)
SF-1	97.30	0.00	0.06	0.00	2.64	1.35
SF-2	95.04	0.01	0.38	1.79	2.79	1.39
SF-3	93.26	0.00	0.21	1.24	5.29	3.93
SF-4	74.95	17.90	2.89	0.52	3.74	0.89
SF-5	97.21	0.00	0.15	0.16	2.48	1.61
SF-6	96.06	0.00	0.14	0.12	2.68	2.73
SF-7	93.65	0.10	0.37	0.23	5.65	4.47
SF-8	97.42	1.27	0.09	0.01	1.21	0.93

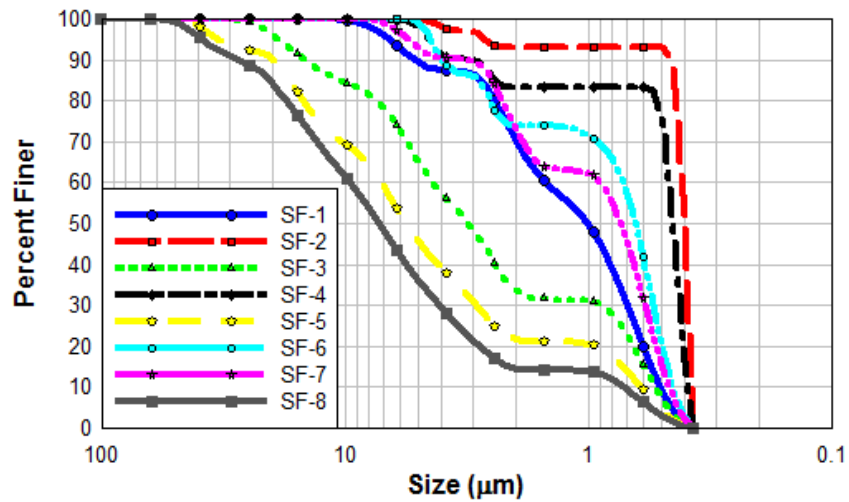


Figure 1.1. Particle size distributions for silica fumes used in pilot study

Initial testing was performed by mixing all batches in a countertop planetary mixer in a temperature-controlled environment. Only three of the eight tested fumes were successfully incorporated into the baseline UHPC matrix by reaching a quasi-liquid state suitable for placement. Four of the other five batches never reached a plastic stage, even after an hour of mixing time. The last batch did reach a plastic stage but failed to transition into a quasi-liquid

state suitable for placement. Measured properties, including mixing time, ASTM C1437 flow percentage [1], density, and compressive strength for the three successful batches are shown in Table 1.2. Mixing time was defined as the time from the first addition of water until a quasi-liquid state suitable for placement was reached. Compressive strength was measured after 14 days of curing, seven at 25°C and 100% humidity and seven at 90°C and 100% humidity.

Table 1.2 shows that SF-2 and SF-7 seemed to outperform the reference SF-1, almost across the board. Each material allowed for more rapid mixing, increased flow, and similar or higher compressive strength. Interestingly, SF-2 was an undensified fume, whereas SF-7 was densified.

Table 1.2. Bench-scale planetary mixing results

Property/Batch	SF-1	SF-2	SF-7
Time – min	14:45	6:15	9:15
Flow - %	57.6	60.6	82.1
ρ – kg/m ³	2372	2337	2390
f_c – MPa	186	185	205

Further testing was performed using additional mixing techniques and larger batch sizes to test the compatibility of the silica fume sources. Additional information on this study can be found in the published conference proceedings [2], here included in Appendix A. The results of this pilot study raised more questions than they answered. Why did only certain silica fumes work in the baseline matrix? Why did SF-5, which is chemically the most similar to SF-1, not successfully incorporate into the baseline matrix? Figure 1.1 indicates that SF-5 is actually coarser than SF-1, which intuitively should ease the mixing process, yet the batch would not successfully mix even with more than three times the required mixing time. The conclusions from this pilot study indicated that one silica fume cannot be used as a simple replacement for another to achieve equivalent material properties of a given UHPC mixture. Further testing with

another lot of one of the silica fumes tested also indicated that much variability can exist from one lot of fume to another, and that this variability can present many problems when using these materials.

The study described in this dissertation was motivated by the questions that arose from the pilot study. Many of those questions are presented above. Fundamentally, can we explain why certain silica fumes work well in UHPCs while others do not? How confident can an engineer be when he or she uses a silica fume product to modify a baseline UHPC matrix? These questions are one and the same, the first from a theoretical perspective and the second from a practical perspective. At its core, that question will be addressed by this study.

1.3 Literature Review

1.3.1 Historical Perspective

Silica fume is a very fine byproduct of the production of silicon or ferrosilicon metals [3], first collected industrially in Norway in 1947 [4]. Bernhardt published the first scientific paper on silica fume's use in concrete in 1952 [5]. By 1978, Norway had created the first standard for direct inclusion of silica fume in concrete [4]. The first major concrete placement with silica fume documented in the United States occurred in 1978 [4], and Buck and Burkes published the first domestic study in 1981 [6]. The first publically bid project in the United States to involve a large silica fume concrete placement was performed by the U.S. Army Corps of Engineers in the 1980s [7].

1.3.2 Industry Perspective

The American Concrete Institute's Committee 234 Silica Fume in Concrete reported that beneficial effects of silica fume include reduction in bleed water, improved particle packing, stronger paste-aggregate interfacial transition zones, and decreased porosity. Drawbacks of silica fume use include an increase in autogenous shrinkage and the necessity of using HRWRA to achieve desired workability [4].

1.3.3 Academic Perspective

Traditionally, silica fume has been used a minor mass replacement of cement, usually between 5% and 10% [4]; however, modern developments in high strength concretes and UHPCs have necessitated the increase in silica fume contents. Russell and Graybeal [8] showed published mixture proportions containing up to 30% silica fume by mass of total binder. In addition to the benefits listed above, silica fume has been used in concretes with durability concerns including alkali-silica reaction [9, 10] and chloride permeability [11, 12].

Many studies have focused on the effects of silica fume on hydration. Papadakis proposed a stoichiometric relationship for the pozzolanic reaction between silica fume and calcium hydroxide [13]. Many studies suggested that silica fume accelerated hydration due to increased surface area for nucleation [14, 15, 16]. Benefits from silica fume hydration have been suggested to last only 24 hours [14, 17], up to seven days [18], and even extended ages [19]. Others showed that silica fume additions delayed strength development up to 28 days for fumes with different fineness [20]. The reactivity of silica fume has been compared to other mineral additives to concrete including traditional supplementary cementitious materials [21], silica

nanoparticles [22, 23, 24], amorphous silica rock [25], and vitreous calcium aluminosulfate [26]. Silica fume was seen as highly reactive when compared to other materials in each case. Zhang and Gjorv [19] showed that increasing silica fume content up to 16% decreased the nonevaporable water content over time, whereas Singh et al. [24] showed that minor additions of silica fume up to 3% increased the nonevaporable water content. Many studies have looked at the hydration products produced from silica fume reaction. Kishar et al. [18] showed the development of calcium-silicate-hydrate (CSH) gel and small ettringite needles. Others showed the development of CSH phases with different densities from those seen in traditional cement hydration [15, 16, 27].

Many studies focused on the benefits of silica fume use in composite materials including increased compressive strength and refined pore structure [28, 29]. Zhang et al. showed that the magnitude of these benefits was greater when undensified silica fume was used rather than densified [30], regardless of curing conditions [31]. Lei et al. [28] showed that increased dispersion of silica fume led to an increase in the mechanical properties of concrete. Wu et al. [29] showed that the mechanical properties of concrete containing silica fume could be negatively influenced by poor workability at increased silica fume contents.

The hydration of cement pastes containing silica fume has been modeled using many different approaches. Powers and Brownyard [32] published one of the first analytical models for the hydration of cement paste that has since been adapted to include the addition of silica fume. The extended Powers-Brownyard model has been used to study autogenous shrinkage in pastes [33] and the development of mechanical properties in concrete [34]. Azad et al. [35] used a

synergistic approach between the Powers-Brownyard model and thermodynamic calculations to improve the accuracy of degree of hydration predictions. Wang [36] modeled the development of mechanical properties by relating the degree of hydration of cement and degree of reaction of silica fume to gel-space ratio. Others have used empirically based models to study the effects of silica fume replacement of cement on hydration [37].

A variety of rheological test methods have been studied using cement pastes and concretes both with and without silica fume. These test methods include ASTM standards such as slump [38], flow table testing [1], and flow cone testing [39]; variations thereof such as modified slump tests [40]; and different rotational rheology methods [41]. Little agreement exists as to the best approach for examining the rheological behavior of cement-based materials.

Many studies have looked at the applicability of certain rheological models for cement pastes containing silica fume, with the Herschel-Bulkley model presented as more representative of the rheology of cement paste with silica fume than more traditional models such as the Bingham plastic model [42, 43, 44]. Mei et al. [44] developed an empirical relationship to describe the rheology of concrete based on the silica fume content and the time after the addition of water, which suggested that increasing silica fume content reduced workability after an optimum content of approximately 5% was reached. Others have developed empirical models relating raw material properties to various rheological characteristics [45, 46, 47]. Vikan et al. [48] suggested that findings from neat cement paste rheology, including increased fineness leading to stiffer pastes and the influence of various chemical additives, could be applicable to pastes with constant silica fume contents. Additional models have been developed to describe the rheology

of cements used in oil well applications [49, 50]. At certain contents, silica fume has been shown to affect concrete rheology similarly to chemical viscosity modifying agents [51]. Much of the published literature concerning the effect of silica fume on the workability of cementitious materials has focused on the compatibility of different high-range water-reducing admixtures with silica fume [42, 52, 53].

Kwan et al. [54] described the theoretical concept of water film thickness as the ratio of volume of water in excess of the porosity between particles and the solid surface area. This concept was studied for mortars consisting of cement and fine aggregate and was shown to correlate strongly with rheological properties. Li and Kwan [55] similarly defined paste film thickness as the volume of paste in excess of the volume of voids between aggregates larger than 75 μm . Paste volume was defined as the total volume of cement, water, and aggregates finer than 75 μm . Compressive strength was shown to increase as paste film thickness increased.

One rapidly growing area of research involving silica fume is its use in UHPC. Russell and Graybeal reported that most UHPC mixture proportions contained silica fume [8]. Some studies have recommended an optimum silica fume content of 20% for UHPC [56], while others suggested no more than 10% to 15% silica fume should be used [57]. The differences are likely related to the specific silica fume used, as research has shown that challenges in workability and strength development can be difficult to overcome depending on the silica fume used [2, 58]. Others have explored whether ternary or quaternary binder systems including silica fume could be used to produce a less expensive UHPC [59].

1.3.4 Commentary

There appears to be a gap in the literature concerning the use of multiple silica fume sources and how their inherent between-source and within-source variabilities affect the hydration kinetics and rheology of cement-silica fume paste. While there is much research concerning the use of a single silica fume source with a single cement source in a specific mixture proportion, experience has shown that success in a single trial is not indicative of a source's performance when applied to a different mixture proportion. Furthermore, the success of a source from one shipment or lot of material is not indicative of future successes, even when used in identical circumstances. There is a lack of knowledge, therefore, in how silica fume fundamentally affects hydration and rheology. This study will focus on the fundamental chemistry, kinetics, and characterization of a constituent material rather than its application in specific mixture proportions. The findings of this study will have implications on the understanding and modeling of all cementitious materials that include silica fume. The largest impact should be on high strength concretes and UHPCs, but the findings should prove beneficial to the concrete and cementitious materials community of practice as a whole.

2. MATERIALS CHARACTERIZATION

Portions of the following section contain text and/or figures and tables previously submitted in **J.F. Burroughs**, C.A Weiss, Jr., J.E. Haddock, and W.J. Weiss, “Modeling early-age rheology of cement-silica fume pastes,” *ACI Materials Journal*, in review.

2.1 Material Types

The baseline UHPC mixture proportion used in this study included four dry constituents and two wet constituents. Each is described in further detail below.

2.1.1 Cement

American Petroleum Institute (API) Class H oil well cement was the primary cementitious material used in this study. Class H cement was used due to its coarser grind and low tricalcium aluminate (C_3A) content. The combination of these factors means that Class H cement can be expected to react more slowly than a more traditional ASTM C150 Type I cement [60].

2.1.2 Inert Aggregates/Fillers

Two inert fillers were included in the baseline mixture proportion: silica sand and silica powder (sometimes called quartz powder). Both materials were chemically identical crystalline forms of silica, with each material being at least 99% SiO_2 . Physical differences in size and shape represented the major difference between these materials.

2.1.3 Silica Fumes

Eight commercially available silica fumes were analyzed in this study. Three of the eight (SF1, SF2, and SF4) were described as undensified silica fumes, meaning little to no processing was

performed on the materials after they were collected as an industrial waste product. The remaining five silica fumes were described as densified silica fumes, meaning pneumatic pressure was applied to the raw waste to intentionally cause agglomerations to occur. The agglomerated form is used to facilitate easier material handling and reduce dust during use. The eight silica fumes were obtained from three separate suppliers. SF5 and SF8 were sold as the same product from the same industrial plant. The two fumes were simply produced at different times. These two fumes were studied to help understand the variability within a single industrial line. SF6 and SF7 were sold as the same product; however, they were produced at different industrial plants and at different times. These two fumes were studied to help understand the variability in a commercial product line. This is summarized in Table 2.1.

Table 2.1. Silica fumes studied

Silica Fume	Supplier	Product Type
SF1	1	Undensified
SF2	1	Undensified
SF3	1	Densified
SF4	1	Undensified
SF5 ^a	2	Densified
SF6 ^b	3	Densified
SF7 ^b	3	Densified
SF8 ^a	2	Densified
^a Same product, different lots		
^b Same product, different industrial plants		

2.1.4 High-Range Water Reducing Admixtures

Three commercially available polycarboxylate ether (PCE) based high-range water-reducing admixtures (HRWRA) were used in this study. HRWRAs are used in low w/c concretes to improve workability without having to add additional water. HRWRA A was the most common HRWRA used throughout this study and consisted of 30% solids. HRWRA B, used in initial

rheological testing, was specifically designed to be used in very low w/c concretes and consisted of approximately 30% solids. HRWRA C was used in a handful of mixture proportions in this study and consisted of 36% solids.

2.1.5 Mix Water

For rheological characterization and calorimetry experiments, distilled water was used exclusively for mixing. For larger volume concrete mixtures, traditional tap water (City of Vicksburg, Mississippi) was used for mixing.

2.2 Characterization Methods

2.2.1 Physical Characterization

Physical characterization of materials included measurements of specific gravity, bulk density, particle size distribution, specific surface area, and absorption capacity. The method used for determining these properties depended on the material being analyzed.

2.2.1.1 Specific Gravity

Specific gravity was determined for each of the eight silica fumes tested in accordance with ASTM C1240 [61]. For six of the eight silica fumes, distilled water was used in analysis. Two silica fumes (SF5 and SF8) contained higher quantities of calcium oxide (CaO) as determined by XRF spectroscopy, which suggested that they both could be hydraulically reactive. As such, water was an unsuitable media for analysis. The specific gravity for these two materials was determined with kerosene substituted for water to prevent any hydraulic reaction. For these analyses, approximately 30 g of silica fume were added to a 500 mL volumetric flask. The flask

was filled approximately one-half full with liquid and shaken to thoroughly wet the silica fume. The remaining volume of the flask was then filled with liquid. The flask was deaired under vacuum pressure and placed into a 23°C water bath until thermal equilibrium was reached. Additional liquid was added as necessary to fill the flask to the exactly 500 mL. The process was repeated without silica fume. The difference in liquid volume was equal to the volume of the silica fume. The density of the silica fume was then determined by dividing the mass of silica fume (~30 g) by the measured volume. Dividing the density of the silica fume by the density of water at 25°C (997 kg/m³) resulted in the specific gravity of silica fume. The specific gravities for cement, silica sand, and silica powder were taken from suppliers' data sheets.

2.2.1.2 Bulk Density

Bulk density was used to quantify the level of densification of each silica fume. Bulk density was determined for seven of the eight silica fumes tested by modifying ASTM D4254 [62] to use a mold with smaller volume (0.005 ft³) to minimize material usage. A cylindrical mold with a diameter of 1.399 in. and a height of 5.417 in. was used for testing. Oven-dried silica fume was poured into the mold until material was approximately 1/2" above the top of the mold. The excess material was then struck off with a straightedge. The mass of silica fume needed to completely fill the mold was determined, and the bulk density was determined by dividing the mass of silica fume by the volume of the mold. This measurement corresponded to the minimum dry density, as no additional effort was made to increase the particle packing. Due to material limitations, this analysis was not performed using SF8.

2.2.1.3 Particle Size Analysis

Particle size distributions were determined for each material studied using laser diffraction analysis, utilizing a Malvern Mastersizer 3000 with the Hydro EV fixture. Water was used as the dispersant fluid for silica sand, silica powder, and silica fume. Isopropyl alcohol was used as the dispersant fluid for cement to prevent any hydraulic reactivity. A 500 mL beaker of clean dispersant fluid was initially analyzed to establish the background for measurement. This background measurement was then subtracted by analysis software from the final measurements. For all testing, the beaker was constantly stirred at 2000 RPM. Material was added to the dispersant fluid until the obscuration level measured between 5% and 10%. Obscuration refers to how “cloudy” the dispersant fluid becomes due to the presence of particles. For all materials except silica sand, the beaker was removed from the testing apparatus, and external ultrasonication was performed for 10 minutes on each sample using a 700 W ultrasonication probe to break up agglomerations prior to testing. After external ultrasonication was performed, the beaker was placed back into the testing apparatus, and additional ultrasonication was performed for three minutes using the low wattage sonication feature of the testing apparatus. After three minutes, six measurements were taken for each material with a 15-second delay between measurements. The instrumentation used for particle size analysis was capable of measuring particles between 0.01 and 3500 μm .

2.2.1.4 Specific Surface Area

Specific surface area is a measurement of the surface area of particles per unit mass. For silica fumes, specific surface area, notated as SSA_{BET} , was determined using the Brunauer-Emmett-Teller (BET) method in accordance with ASTM C1069 [63]. Measurements were performed

using a Quantachrome NovaTouch LX⁴ analyzer. Approximately 150 mg of silica fume were used for analysis. The specimens were degassed under vacuum pressure using the following temperature profile:

- Heat to 60°C at 2°C/min, and hold for 30 minutes
- Heat to 120°C at 2°C/min, and hold for 30 minutes
- Heat to 300°C at 2°C/min, and hold for 180 minutes

Specimens were then analyzed at 77 K at relative pressures of N₂ from 0.05 to 0.30. Multipoint BET analysis was then performed using the instrumentation software to determine the specific surface area. For comparison, specific surface areas, notated as SSA_{PSD} , was also estimated from particle size distributions. To estimate the specific surface area from the particle size distribution, the volume, surface area, and mass of a representative particle in each size bin was calculated assuming each particle was a solid sphere. By dividing the bin volume by the respective particle volume, an estimate of the total number of particles in each size bin could be determined. The expected mass and surface area of particles contained in each size bin was then calculated. The total surface area and mass contained in the distribution was determined by summing each of the individual size bins. The specific surface area was estimated by dividing the total surface area by the total mass.

Specific surface area, also known as Blaine fineness, was determined for cement and silica powder in accordance with ASTM C204 [64]. To determine Blaine fineness, a test bed of material having an approximate porosity of 0.500 was prepared. Air permeability tests were then performed on the prepared test beds by measuring the time required for the manometer fluid to

travel from the second mark to the third mark on the testing apparatus. All testing was performed at room temperature. The specific surface area for silica sand was estimated from the particle size distribution, assuming that the particles were spherical.

2.2.1.5 Absorption Capacity

The models developed in this research require careful accounting of free and bound water, so determining the water physically absorbed by each constituent was critical. Due to the very small average particle size (~100 nm) of silica fume, traditional absorption techniques for aggregates in concrete were not suitable for these materials. ASTM C127 [65] is only applicable to coarse aggregates rather than fine aggregates and requires the physical drying of surfaces for testing. The surfaces of silica fume particles can be finer than can be seen with the human eye, so physical drying was not feasible. ASTM C128 [66] is applicable for fine aggregates but was deemed unsuitable for silica fume. This approach requires saturation for 24 hours before drying. During the drying process, silica fume particles tend to agglomerate even further, making it impossible to determine when the material reaches saturated-surface-dry (SSD) condition. Due to these difficulties, four different approaches were used to estimate the absorption capacity of silica fume: statistical approximation, atmospheric absorption, vacuum filtration, and dynamic vapor sorption. Each of these approaches is described in detail below.

2.2.1.5.1 Statistical Approximation

Statistical approximations of absorption capacity based on particle size distribution, density, and specific surface area were estimated for each of the silica fumes. The estimation process is as follows, and an example calculation is shown in Table 2.2:

1. The volume ($V_{particle}$) and surface area ($A_{s,particle}$) of a representative spherical particle in each size bin is calculated.
2. Assuming a total unit volume ($V_{assumed}$), the number of particles ($n_{particles}$) in each bin is determined by dividing the bin volume ($f_{vol}V_{assumed}$) by the volume of the representative particle ($V_{particle}$).
3. The total surface area within each bin ($A_{s,bin}$) is determined by multiplying the number of particles ($n_{particles}$) in each bin by the surface area of the representative particle ($A_{s,particle}$).
4. The total surface area for the entire distribution ($A_{s,total}$) is determined by summing the bin surface areas ($A_{s,bin}$).
5. The required mass of the distribution ($m_{required}$) is determined by dividing the total surface area ($A_{s,total}$) by the specific surface area as determined by the BET method (SSA_{BET}).
6. The required solid density ($\rho_{solid,required}$) is determined by dividing the required mass ($A_{s,total}$) by the assumed unit volume ($V_{assumed}$).
7. The percentage of solids in the distribution (p_{solids}) is determined by dividing the measured density ($\rho_{measured}$) by the required density ($\rho_{solid,required}$).

8. The absorption capacity/porosity ($\Phi_{volumetric}$) is determined by subtracting the percentage of solids (p_{solids}) from 1.

Table 2.2. Example calculation for statistical approximation of absorption capacity

$d_{particle}$ (nm)	$V_{particle}$ (nm ³)	$A_{s,particle}$ (nm ²)	f_{vol}	$n_{particles}$	$A_{s,bin}$ (μm ²)
52.6	76100	8680	2.73%	359	3.12
59.7	112000	11200	2.81%	252	2.82
67.9	164000	14500	2.86%	175	2.53
77.1	240000	18700	2.89%	120	2.25
87.6	352000	24100	2.89%	82	1.98
99.5	516000	31100	2.87%	56	1.73
113.1	757000	40200	2.83%	37	1.50
128.5	1110000	51900	2.77%	25	1.29
All Other Diameters			77.35%	44000	57.8
$A_{s,total}$ (μm ²)					75.0
SSA_{BET} (m ² /g)					18.1
$m_{required}$ (pg)					4.14
$V_{assumed}$ (μm ³)					1
$\rho_{solid,required}$ (g/cm ³)					4.14
$\rho_{measured}$ (g/cm ³)					2.36
p_{solids}					0.571
$\Phi_{volumetric}$					0.429

2.2.1.5.2 Atmospheric Absorption

Atmospheric absorption involved suspending specimens of silica fume above a reservoir of distilled water in a sealed container. The reservoir of water below caused the humidity within the chamber and the moisture content of silica fume specimens to change so that the sealed system could reach equilibrium. Minor fluctuations in laboratory temperature also caused changes in chamber humidity. Mass change of specimens was recorded over a 13-month period to measure the amount of moisture absorbed by the silica fumes. Measurements were taken daily for the first 20 days, weekly for the next 34 weeks, biweekly for the next eight weeks, and

monthly through the end of the experiment. As with bulk density, this approach was not used for SF8 due to limited material availability. This test setup is shown in Figure 2.1.



Figure 2.1. Atmospheric absorption test setup

2.2.1.5.3 Vacuum Filtration

The vacuum filtration technique involved filtering solutions of silica fume and distilled water mixed in prescribed ways through a fine filter ($0.22\ \mu\text{m}$) under vacuum until no additional water was readily removed by the vacuum. While some very fine particles of silica fume were able to pass through the filter, the vast majority of particles remained agglomerated on the filter. The moisture content of the material remaining on the filter was then determined after drying overnight in a 105°C oven. Suspensions of silica fume and distilled water were combined using three approaches: as-received, after shear mixing, and after sonication. The as-received specimens were prepared by simply pouring distilled water into a beaker containing silica fume and allowing the turbulence created to blend the materials. Other specimens were blended using a paddle mixer for five minutes at different rates (100, 200, and 500 RPM) to see what effect shear rate had on the measurements. Lastly, additional specimens were prepared by sonicating

silica fume in distilled water for 10 minutes using a 700 W ultrasonication probe. The filtration setup can be seen in Figure 2.2.

Regardless of mixing procedure, the testing process was as follows:

1. The mass of the dry filter paper was determined.
2. The filter paper was saturated with distilled water, and the mass of the wet filter paper was determined.
3. Approximately 1 g of silica fume was combined with approximately 50 mL of distilled water in a separate beaker according to the designated procedure.
4. The combined suspensions were added to the vacuum filtration setup, and the beaker was rinsed with additional distilled water to ensure all of the silica fume was added to the filtration setup.
5. The vacuum pump was activated, and testing continued until at least 60 seconds elapsed between drops of water passing through the filter.
6. The vacuum pump was deactivated, and the combined wet mass of filter paper, silica fume, and residual water was determined.
7. The wet filter paper and silica fume was placed in an oven at 105°C overnight to remove all residual moisture.
8. The mass of dry filter paper and silica fume was determined.
9. The mass of dry silica fume was determined by subtracting the mass of the dry filter paper from Step #1 from the combined mass of dry filter paper and silica fume from Step #8.

10. The mass of residual water was determined by subtracting both the mass of dry silica fume from Step #9 and the mass of wet filter paper from Step #2 from the combined wet mass determined in Step #6.
11. The residual moisture content was determined by dividing the residual water from Step #10 by the mass of dry silica fume determined in Step #9.



Figure 2.2. Vacuum filtration setup

2.2.1.5.4 Dynamic Vapor Sorption

Dynamic vapor sorption (DVS) is an approach that measures the change in mass of materials over time when exposed to sweeps of relative humidity (RH) at a constant temperature. For this study, silica fume specimens were exposed to an adsorption sweep from 5% to 95% RH in 5% RH increments at 23°C and a desorption sweep from 95% to 5% RH in 5% RH increments at 23°C. Measurements were recorded in approximately five-minute intervals. Mass stability was defined as a minimum of two successive measurements with less than a 0.01% change in mass. The raw data were then fit to the Double Log Polynomial (DLP) model, as shown in Equation 1.

$$m = \beta_3 [\ln(-\ln(RH))]^3 + \beta_2 [\ln(-\ln(RH))]^2 + \beta_1 [\ln(-\ln(RH))] + \beta_0 \quad (1)$$

After fitting the raw data with the DLP model, a difference curve was generated by subtracting the adsorption isotherm from the desorption isotherm. The integral of the difference curve from 10% to 90% RH was taken as the absorption capacity of the specimen. These bounds were chosen to eliminate any unusual artifacts caused by the DLP fits at both low and high RH. Representative examples of both the DLP fits and difference curve are shown in Figure 2.3.

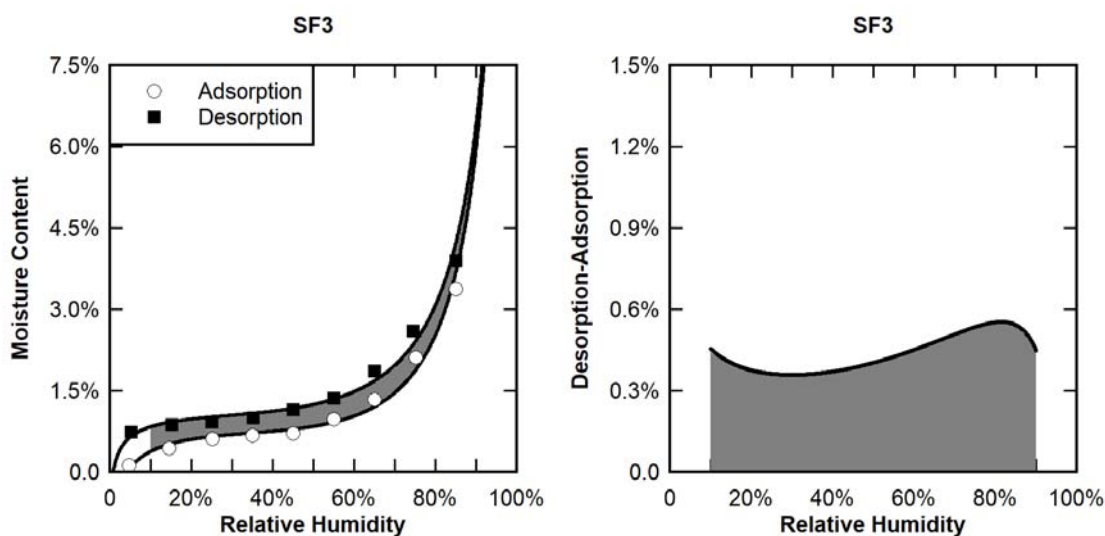


Figure 2.3. Representative data with DLP fits (left) and difference curve (right)

2.2.2 Chemical Characterization

2.2.2.1 X-Ray Diffraction

X-ray diffraction (XRD) analysis was used to determine the presence of crystalline phases and estimate the amorphous fraction present in the silica fumes examined in this study. Random orientation powder mounts were used to test specimens. XRD patterns were collected using an X-Pert Pro Multipurpose Powder Diffractometer system (Malvern Panalytical, Inc.). Scans were performed from 2 to 70 $^{\circ}2\theta$ in 0.02 $^{\circ}2\theta$ increments using Co-K α radiation. Analysis of

diffraction patterns was performed using the Jade2010 program (Materials Data, Inc.). Sharp peaks indicated highly crystalline phases whereas very broad “peaks” indicated the presence of amorphous or glassy material. XRD analysis followed Bragg’s Law, shown in Equation 2. In order to satisfy conditions of constructive interference, n_{Bragg} is required to be a positive integer value.

$$2d \sin \theta = n_{Bragg} \lambda \quad (2)$$

This characterization was critical because traditional theory suggests that only amorphous silica present in the silica fumes should be reactive. Quantitative Rietveld analysis was performed on XRD patterns to estimate the mineralogical composition of each silica fume. Quantitative whole pattern fits for each silica fume tested are included in Appendix B.

2.2.2.2 X-Ray Fluorescence

Wavelength dispersive XRF spectroscopy was performed on silica fume specimens using an Axios Cement spectrometer (Malvern Panalytical, Inc.) to determine the bulk chemistry of the materials. In performing XRF spectroscopy, materials are excited by x-rays at various wavelengths that cause electrons to be ejected from bands at characteristic energies. These energies are detected and converted to chemical oxides for reporting. For testing, specimens were prepared as glass disks using the procedure below. The resulting specimen was a transparent glass disk suitable for analysis. Table 2.3 shows parameters for each element scanned using XRF and the corresponding oxide for reporting. Quantitative analysis was performed using SuperQ software (Malvern Panalytical, Inc.).

1. 1.25 g of silica fume was blended with 7.50 g of lithium borate – lithium iodide flux (49.75% $\text{Li}_2\text{B}_4\text{O}_7$ – 49.75% LiBO_2 – 0.50% LiI).

2. Silica fume – flux mixture was heated to 1000°C and held for five minutes.
3. The mixture was then heated to 1040°C and held for 15 minutes.
4. The molten glass was poured into a disk mold.
5. The disks were cooled to room temperature over the next eight minutes before being removed from the molds.

Table 2.3. XRF scan parameters

Element	Voltage (kV)	Current (mA)	Angle (°2θ)	Chemical Oxide
Aluminum	24	100	144.9712	Al ₂ O ₃
Calcium	30	80	113.1820	CaO
Chromium	60	40	69.3288	Cr ₂ O ₃
Iron	60	40	57.5668	Fe ₂ O ₃
Magnesium	24	100	23.1648	MgO
Manganese	60	40	63.0308	Mn ₂ O ₃
Phosphorus	24	100	141.0388	P ₂ O ₅
Potassium	25	96	136.7518	K ₂ O
Silicon	24	100	109.1582	SiO ₂
Sodium	24	100	27.9746	Na ₂ O
Strontium	60	40	25.1550	SrO
Sulfur	25	96	110.7202	SO ₃
Titanium	40	60	86.2206	TiO ₂
Zinc	60	40	41.8352	ZnO
Zirconium	60	40	22.4990	ZrO ₂

2.2.2.3 Loss on Ignition

Loss on ignition (LOI) testing was performed on silica fume specimens to determine any organic content. Testing was performed in accordance with ASTM C1240 [61]. Approximately 1 g of material was fired in a crucible at 750°C for 45 minutes and allowed to cool. The masses before and after firing were determined. The change in masses calculated is called the loss on ignition. Organic impurities in silica fumes traditionally are associated with the materials used to heat the

furnaces at silicon and ferrosilicon metal plants. LOI testing is also traditionally associated with the color of silica fumes, with darker fumes having greater LOI.

2.3 Characterization Results

2.3.1 Class H Cement

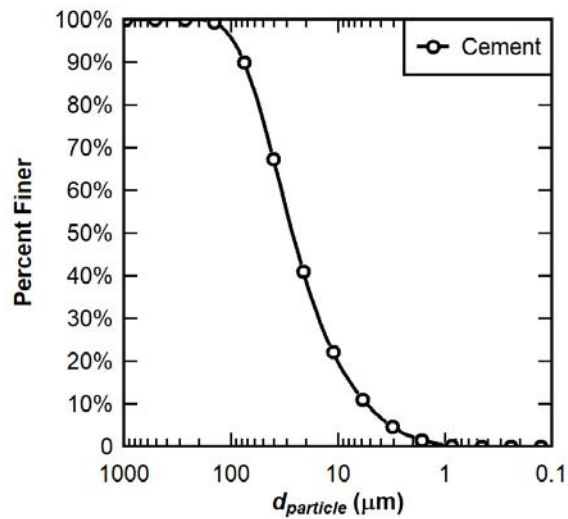


Figure 2.4. Class H cement particle size distribution

Class H cement was characterized for particle size and Blaine fineness. The particle size distribution is shown in Figure 2.4. As shown, the average particle size was 26.7 μm . Blaine fineness and chemical composition are shown in Table 2.4. Chemical composition was taken from suppliers' data sheets. A specific gravity of 3.15 was assumed for cement.

Table 2.4. Class H cement characterization results

Chemical Composition	
SiO ₂ , %	22.1
Al ₂ O ₃ , %	2.7
Fe ₂ O ₃ , %	4.5
CaO, %	64.7
MgO, %	2.2
SO ₃ , %	2.8
LOI, %	1.0
Blaine fineness, m ² /kg	
310	

2.3.2 Silica Sand

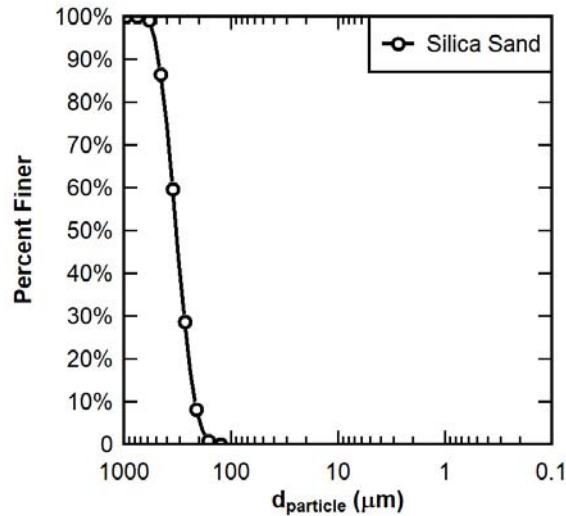


Figure 2.5. Silica sand particle size distribution

Silica sand was characterized for particle size. From the particle size distribution, a specific surface area was estimated, assuming spherical particles. The particle size distribution is shown in Figure 2.5. As shown, the average particle size was 326 μm. Specific surface area, specific gravity, and chemical composition are reported in Table 2.5. The specific gravity and chemical composition were taken from suppliers' safety data sheets.

Table 2.5. Silica sand characterization results

Material Property	Value
Specific Surface Area, m ² /kg	13
Specific Gravity	2.65
SiO ₂ , %	>95

2.3.3 Silica Powder

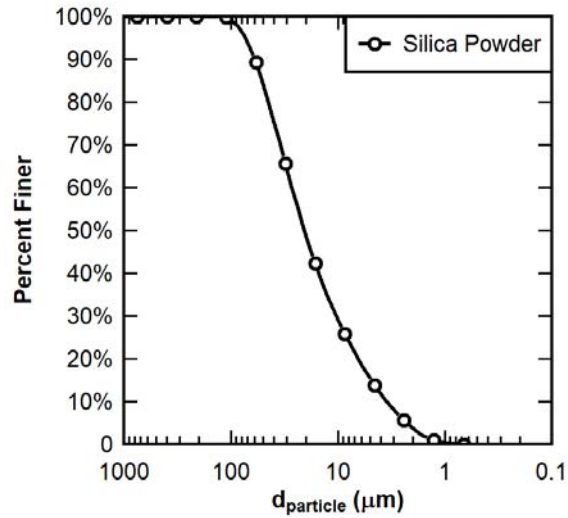


Figure 2.6. Silica powder particle size distribution

Silica powder was characterized for particle size and Blaine fineness. The particle size distribution is shown in Figure 2.6. As shown, the average particle size was 20.7 μm. Specific surface area, specific gravity, and chemical composition are reported in Table 2.6. The specific gravity and chemical composition were taken from suppliers’ safety data sheets.

Table 2.6. Silica powder characterization results

Material Property	Value
Specific Surface Area, m ² /kg	565
Specific Gravity	2.65
SiO ₂ , %	>95

2.3.4 Silica Fumes

Each silica fume was completely characterized by the methods described in Section 2.2.

Comparative data between silica fumes are included in this section. Additional details and micrographs are included for each silica fume in the subsequent sections. Particle size

distributions for each silica fume are shown in Figure 2.7. As is shown, SF1 was the coarsest

silica fume tested and was the most unique silica fume in terms of particle size. SF2, SF3, SF5,

and SF8 had similar particle size distributions and were of medium fineness. SF4, SF6, and SF7

were the finest silica fumes and had similar particle size distributions. Comparing those fumes

that were identical products, SF5 and SF8 had similar particle size distributions, with SF5 being

slightly coarser. SF6 and SF7 had almost identical particle size distributions.

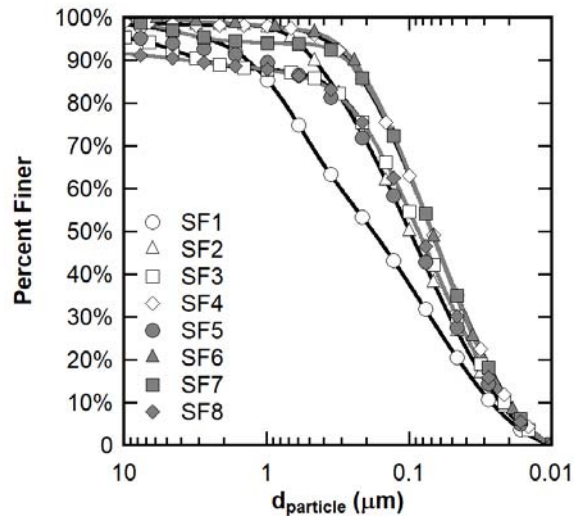


Figure 2.7. Silica fume particle size distributions

Specific gravities, bulk densities, and specific surface areas are shown in Table 2.7. Measured

specific gravities (G_s) ranged from 2.21 to 2.37. Comparing similar silica fume products, SF8

was appreciably denser than SF5, and SF6 was slightly denser than SF7. Bulk density

measurements (ρ_{bulk}) supported supplier classifications concerning undensified and densified

silica fumes. SF1, SF2, and SF4 all had bulk densities below 420 kg/m³, whereas the four densified silica fumes tested had bulk densities greater than 650 kg/m³. SF7 had a slightly greater bulk density than SF6, even though the specific gravity was lower, suggesting significantly more densification effort was used for this product.

Specific surface areas as measured by the BET method ranged from 18 to 30 m²/g. SF1 and SF8 had the lowest surface areas, SF3, SF5, SF6, and SF7 were of medium surface area, and SF2 and SF4 had the highest surface areas. Specific surface areas as estimated from particle size distributions are also shown for comparison. The SSA_{PSD} measurements ranged from 31 to 55 m²/g, which is appreciably higher than the SSA_{BET} measurements. Once again, SF1 had the lowest surface area, and SF4 had the highest surface area.

Table 2.7. Physical characterization data for silica fumes

Silica Fume	G_s	ρ_{bulk} (kg/m ³)	SSA_{BET} (m ² /g)	SSA_{PSD} (m ² /g)
SF1	2.37	412	18.1	31.7
SF2	2.23	319	29.3	43.7
SF3	2.30	706	22.0	45.5
SF4	2.23	386	29.4	54.3
SF5	2.23	698	25.7	43.9
SF6	2.26	670	24.0	52.6
SF7	2.21	726	22.8	54.2
SF8	2.34	--- ^a	19.8	44.8

^aDue to limited material supply, ρ_{bulk} was not determined for SF8.

Absorption capacity estimates by mass of silica fume using each of the four methods described above are shown in Table 2.8. Individual analyses from dynamic vapor sorption data are included in the subsequent sections. Figure 2.8 shows mass change from atmospheric absorption over time for each of the tested silica fumes. As shown in Table 2.8, dynamic vapor sorption

gave the lowest absorption capacities for silica fumes, whereas vacuum filtration tended to give the highest estimates.

Table 2.8. Absorption capacity estimates by mass for silica fumes

Silica Fume	α_{SA} (%)	α_{AA} (%)	$\alpha_{VF,NM}$ (%)	$\alpha_{VF,100}$ (%)	$\alpha_{VF,200}$ (%)	$\alpha_{VF,500}$ (%)	$\alpha_{VF,S}$ (%)	α_{DVS} (%)
SF1	18.1	6.4	121.9	115.9	95.2	94.5	38.6	0.121
SF2	14.8	20.6	198.2	159.5	149.2	147.3	64.6	0.107
SF3	22.4	52.2	63.5	58.7	57.5	59.7	38.7	0.348
SF4	20.5	23.0	192.4	168.9	145.6	152.3	64.1	0.075
SF5	18.6	29.2	67.3	68.1	57.7	57.6	68.9	0.761
SF6	24.0	29.9	73.0	53.4	51.3	67.7	47.0	0.368
SF7	26.2	36.9	60.3	47.3	46.6	56.7	32.0	0.132
SF8	23.8	--- ^a	72.5	63.7	61.5	65.7	75.4	0.625

^aDue to limited material supply, this test was not performed for SF8.

Table 2.9 shows relative ranks for absorption capacity estimates for each test method with 1 representing the lowest estimate and 8 representing the greatest estimate. Vacuum filtration seemed to give opposite results than the other test methods. For statistical approximation, atmospheric absorption, and dynamic vapor sorption, the undensified fumes were always in the lowest half of estimates; however, this changes when analyzing the vacuum filtration results. While the magnitudes of the estimates vary rather dramatically among test methods, the relative rankings of absorption capacity suggested that undensified silica fumes have the capacity to absorb less water than densified silica fumes. This is because the densified silica fumes have a greater potential to absorb water into agglomerations in addition to absorbing water into and onto the surface of the individual particles themselves.

Table 2.9. Relative ranks of absorption capacity estimates

Silica Fume	a_{SA} (%)	a_{AA} (%)	$a_{VF,NM}$ (%)	$a_{VF,100}$ (%)	$a_{VF,200}$ (%)	$a_{VF,500}$ (%)	$a_{VF,S}$ (%)	a_{DVS} (%)
SF1	2	1	6	6	6	6	2	3
SF2	1	2	8	7	8	7	6	2
SF3	5	7	2	3	3	3	3	5
SF4	4	3	7	8	7	8	5	1
SF5	3	4	3	5	4	2	7	8
SF6	7	5	5	2	2	5	4	6
SF7	8	6	1	1	1	1	1	4
SF8	6	---	4	4	5	4	8	7

Comparing the different test methods, the high estimates of absorption capacity from vacuum filtration suggested that this method might have overestimated absorption capacity. Because it was difficult to determine when all of the surface water has been removed without emptying any potential internal pores, it was challenging to determine when to stop the vacuum filtration testing. Atmospheric absorption was seen as a good test method for comparing the relative absorption potentials of silica fumes; however, some of the silica fumes tested were still absorbing moisture after one year of testing. This length of testing makes this approach less practical. Statistical approximation was the quickest method to perform as it simply estimated the capacity based on other characterization results. As such, this approach is a quick way to get a relative idea of the absorption capacity. Dynamic vapor sorption was determined to be the most reliable test method for determination of absorption capacity. Testing could be performed in less than two weeks, and the data were actual measurements rather than estimations from other tests.

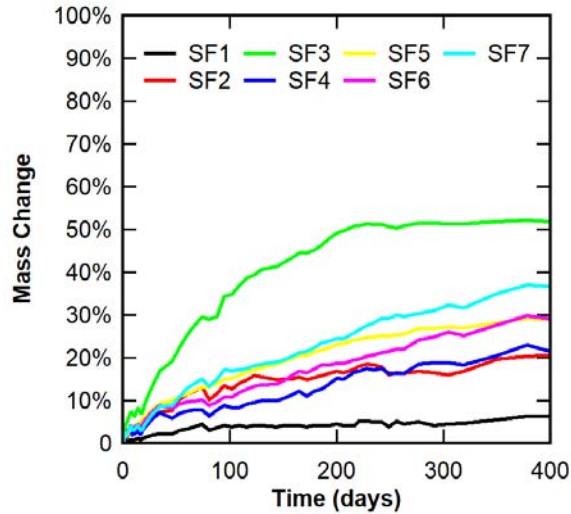


Figure 2.8. Atmospheric absorption results

Quantitative XRD was used to determine the amorphous content of each of the silica fumes tested. Results are shown in Table 2.10. As shown, each of the silica fumes was at least 88% amorphous. High amorphous content was expected in these pozzolanic materials, as the amorphous phases are potentially reactive.

Table 2.10. Amorphous content of silica fumes from quantitative XRD

Silica Fume	Amorphous Content (%)
SF1	96.9
SF2	98.6
SF3	99.2
SF4	99.3
SF5	88.1
SF6	98.3
SF7	97.4
SF8	90.2

The chemical composition of each silica fume is shown in Table 2.11. As is shown, a wide range of chemistries was seen in the eight silica fumes tested. Three silica fumes (SF3, SF5, and SF8) failed to meet ASTM C1240 specifications for minimum SiO₂ content (85%).

Additionally, SF8 exceeded the maximum LOI specification from ASTM C1240 (6%).

Comparing similar commercial products, SF5 and SF8 did show similar chemistries (low SiO₂, high CaO and LOI), and neither met ASTM C1240 specifications. Comparing SF6 and SF7, SF7 was a higher purity fume with the SiO₂ difference mainly accounted for by differences in MgO, Mn₂O₃, and LOI. Additionally, all densified silica fumes (SF3, SF5-SF8) had LOIs exceeding 1%, whereas none of the undensified silica fumes (SF1, SF2, and SF4) had LOIs exceeding 1%. This suggests that the densification process may be contributing to the organic content of the silica fumes. While reported industrial practice uses only the application of pneumatic pressure in densification, these results suggest that some type of organic chemical treatment may also be used in the densification process.

Table 2.11. Chemical composition of silica fumes

Silica Fume	SiO ₂ (%)	CaO (%)	MgO (%)	Mn ₂ O ₃ (%)	LOI (%)	Balance (%) ^a	Other ^b
SF1	92.2	1.5	0.2	2.2	0.9	3.0	ZrO ₂
SF2	95.9	0.3	0.3	1.4	0.9	1.2	None
SF3	83.4	0.9	1.3	5.4	2.0	7.0	K ₂ O, ZnO
SF4	97.8	0.3	0.2	0.0	0.9	0.8	None
SF5	70.0	19.5	2.6	0.0	5.1	2.9	None
SF6	90.4	0.6	1.9	3.3	2.5	1.3	None
SF7	94.3	0.6	0.3	1.7	2.0	1.2	None
SF8	68.4	18.0	2.0	0.1	8.9	2.6	None

^aTotal content of other XRF phases
^bOther XRF phases greater than 1%

2.3.4.1 SF1

SF1, shown in Figure 2.9, was a commercially available undensified silica fume that was light gray in color. Results from dynamic vapor sorption analysis are shown in Figure 2.10. XRD patterns are shown in Figure 2.11. Identified crystalline phases included silicon metal and two zirconium oxide phases (zirconium oxide and baddeleyite). These zirconium phases are unique when compared to most silica fumes and are byproducts of zirconium being included in the silicon metal production process.

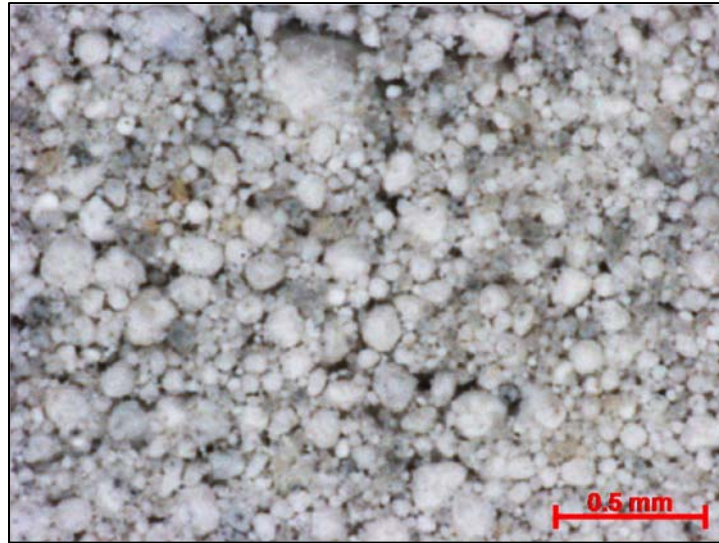


Figure 2.9. SF1

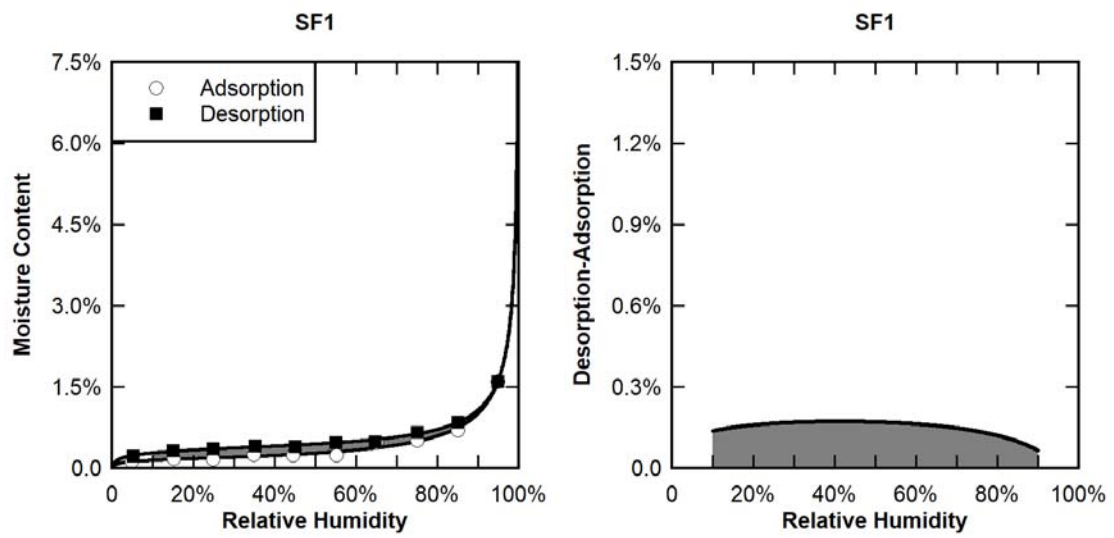


Figure 2.10. Dynamic vapor sorption data (left) and hysteresis area analysis (right) for SF1

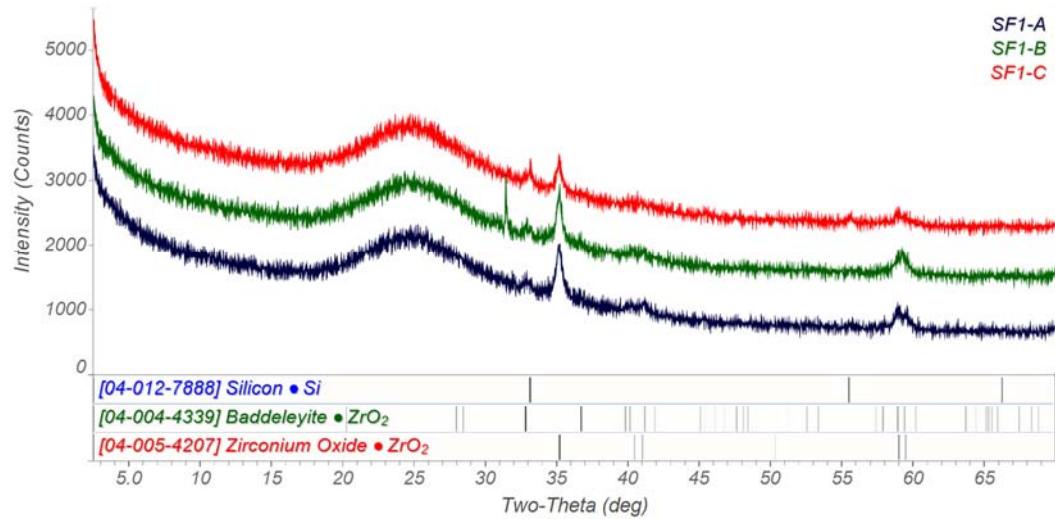


Figure 2.11. XRD patterns for SF1

2.3.4.2 SF2

SF2, shown in Figure 2.12, was a commercially available undensified silica fume that was light gray in color. Results from dynamic vapor sorption analysis are shown in Figure 2.13. XRD patterns are shown in Figure 2.14. Identified crystalline phases included elemental silicon, quartz, and silicon carbide. SF2, SF4, SF6, and SF7 were found to have very similar mineralogical compositions.

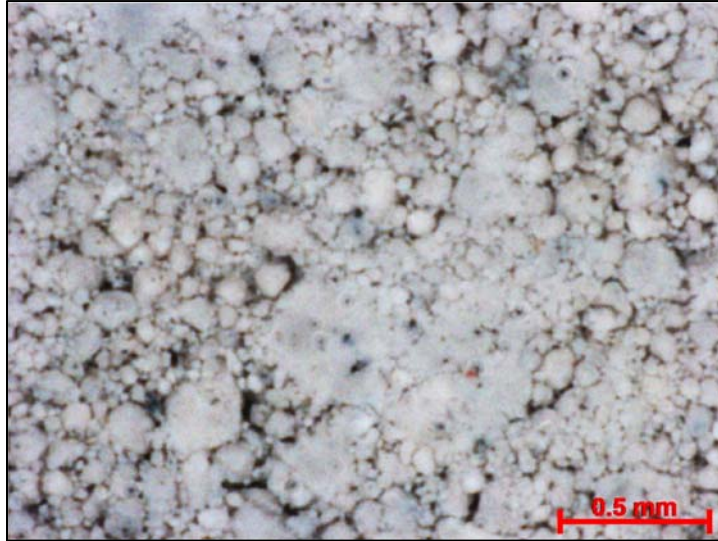


Figure 2.12. SF2

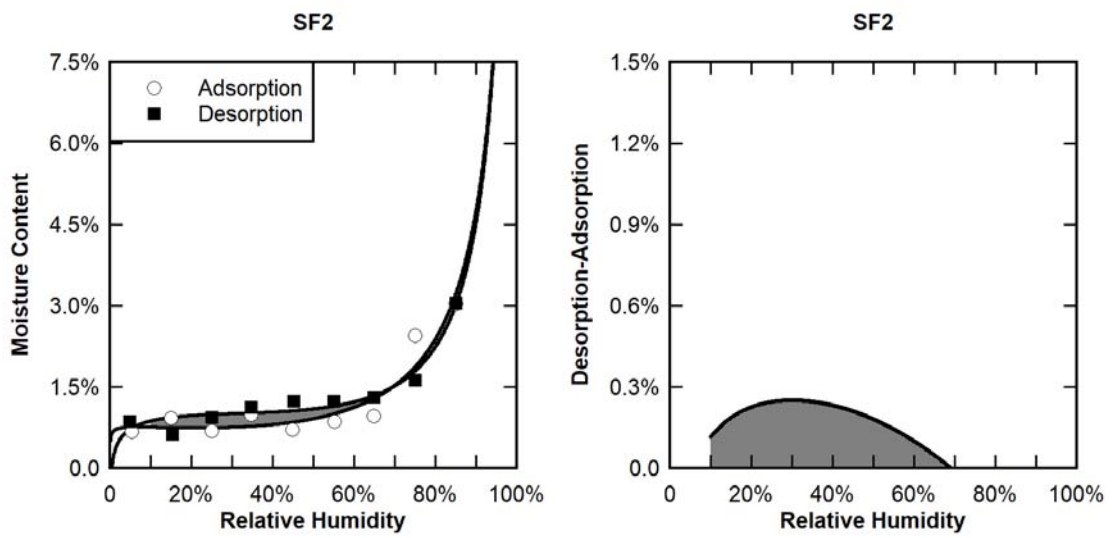


Figure 2.13. Dynamic vapor sorption data (left) and hysteresis area analysis (right) for SF2

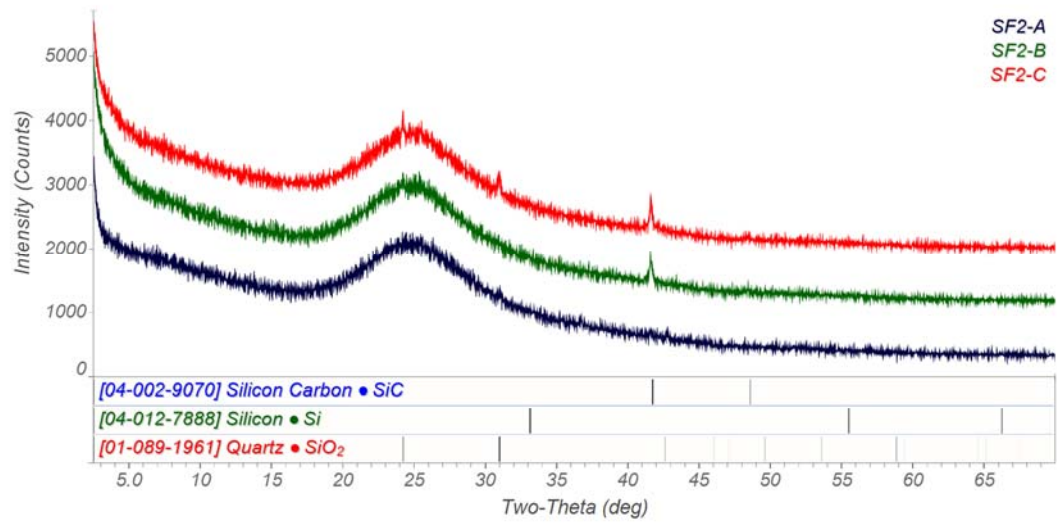


Figure 2.14. XRD patterns for SF2

2.3.4.3 SF3

SF3, shown in Figure 2.15, was a commercially available densified silica fume that was light gray in color. Results from dynamic vapor sorption analysis are shown in Figure 2.16. XRD patterns are shown in Figure 2.17. Identified crystalline phases included baddeleyite, elemental silicon, halite, quartz, and zirconium oxide. The presence of halite was unique to SF3.

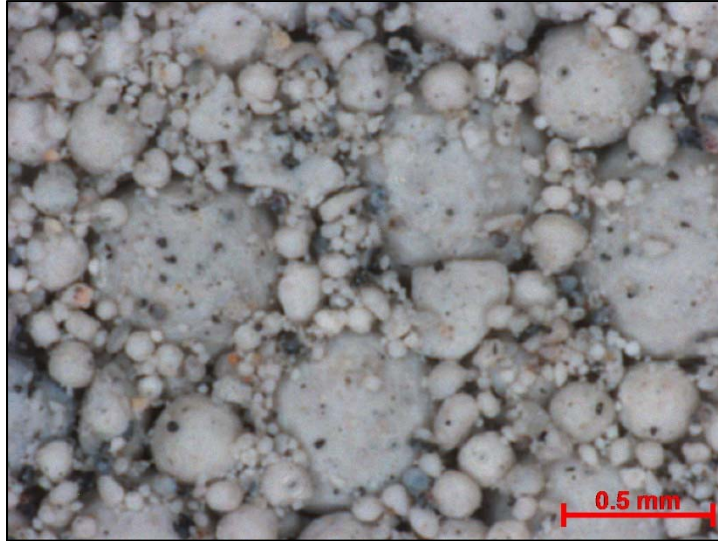


Figure 2.15. SF3

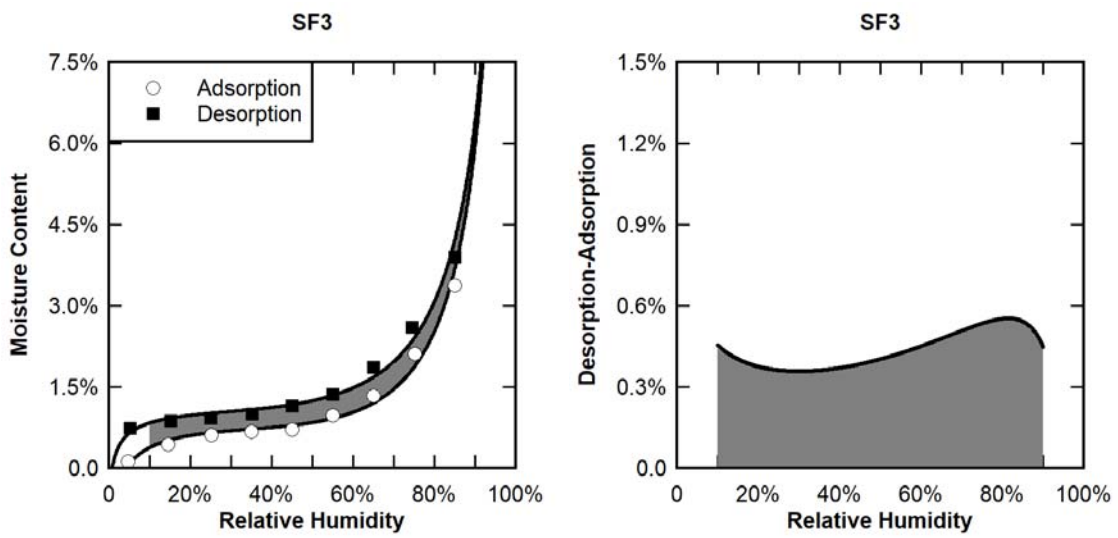


Figure 2.16. Dynamic vapor sorption data (left) and hysteresis area analysis (right) for SF3

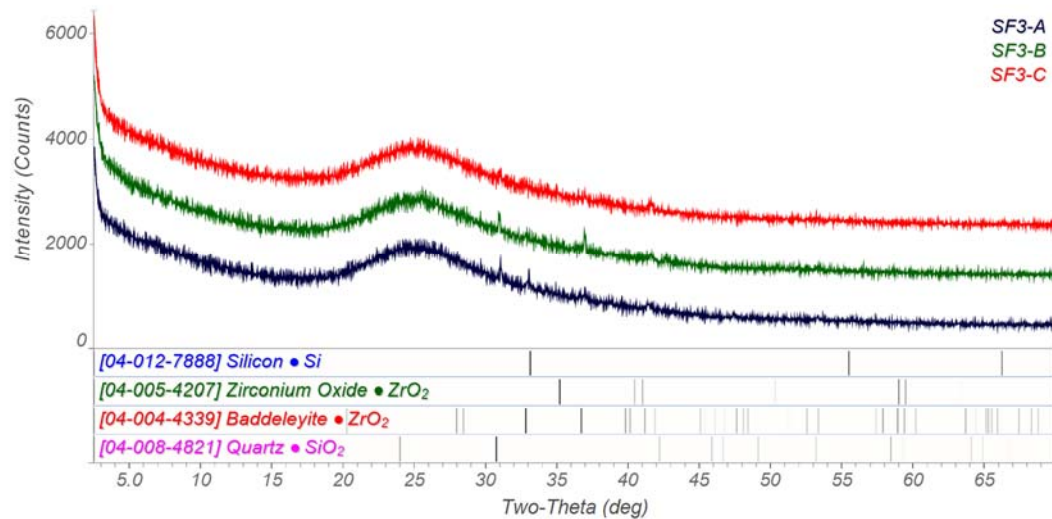


Figure 2.17. XRD patterns for SF3

2.3.4.4 SF4

SF4, shown in Figure 2.18, was a commercially available undensified silica fume that was light gray in color. Results from dynamic vapor sorption analysis are shown in Figure 2.19. An XRD pattern is shown in Figure 2.20. Identified crystalline phases included elemental silicon, quartz, and silicon carbide. SF2, SF4, SF6, and SF7 were found to have very similar mineralogical compositions.

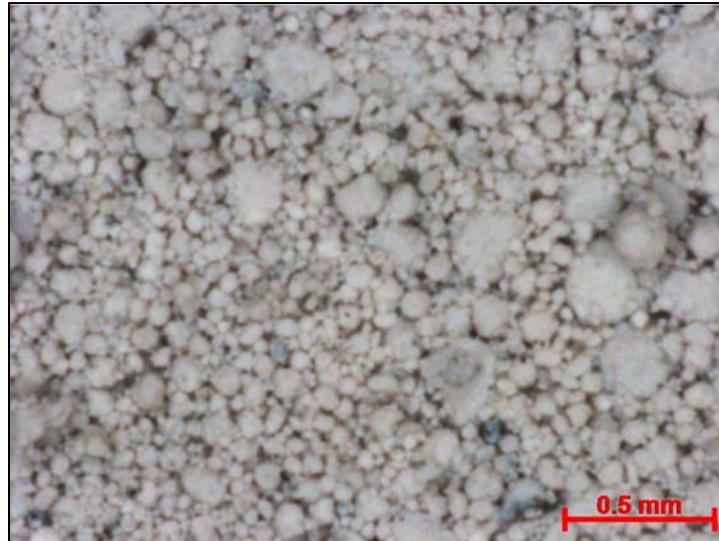


Figure 2.18. SF4

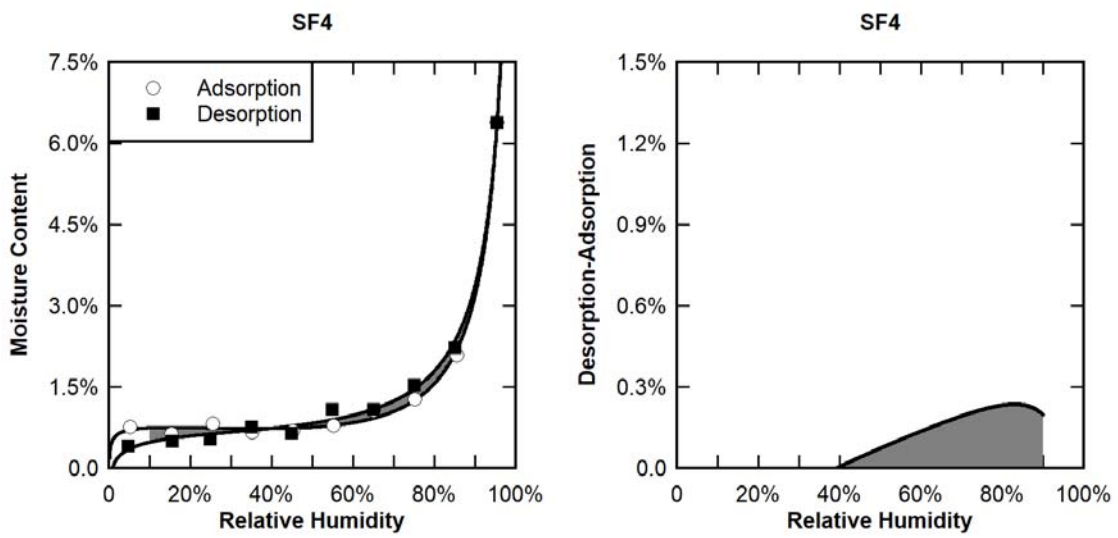


Figure 2.19. Dynamic vapor sorption data (left) and hysteresis area analysis (right) for SF4

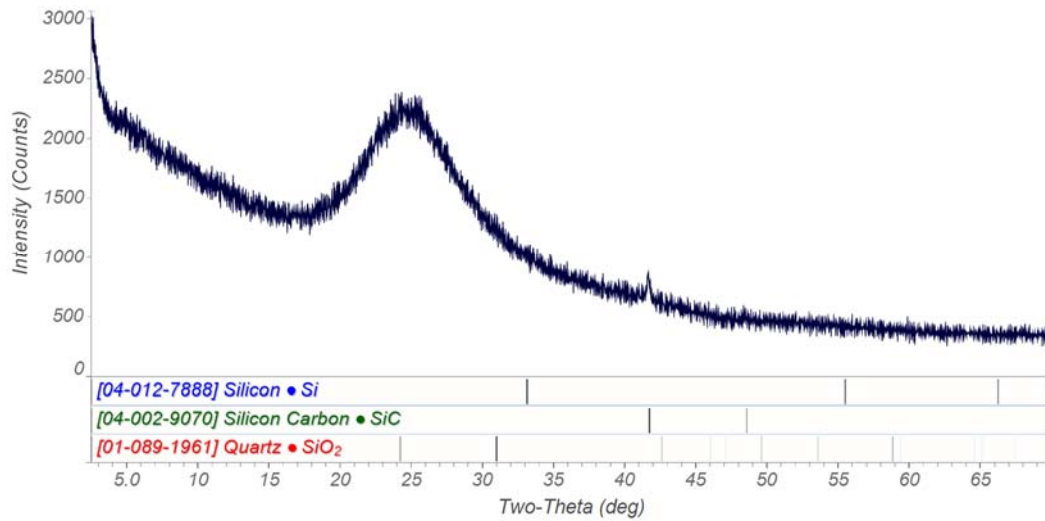


Figure 2.20. XRD pattern for SF4

2.3.4.5 SF5

SF5, shown in Figure 2.21, was a commercially available densified silica fume that was gray in color. It was produced at the same industrial plant and was marketed as the same product as SF8. Results from dynamic vapor sorption analysis are shown in Figure 2.22. XRD patterns are shown in Figure 2.23. Identified crystalline phases included calcite, hatrurite, periclase, perovskite, quartz, and silicon carbide. As expected from XRF spectroscopy, multiple calcium-containing phases were present in SF5, including calcite, perovskite, and hatrurite, which is a cementitious phases similar to tricalcium silicate (C_3S). The presence of such phases further suggested hydraulic reactivity. Periclase and perovskite were only identified in SF5.



Figure 2.21. SF5

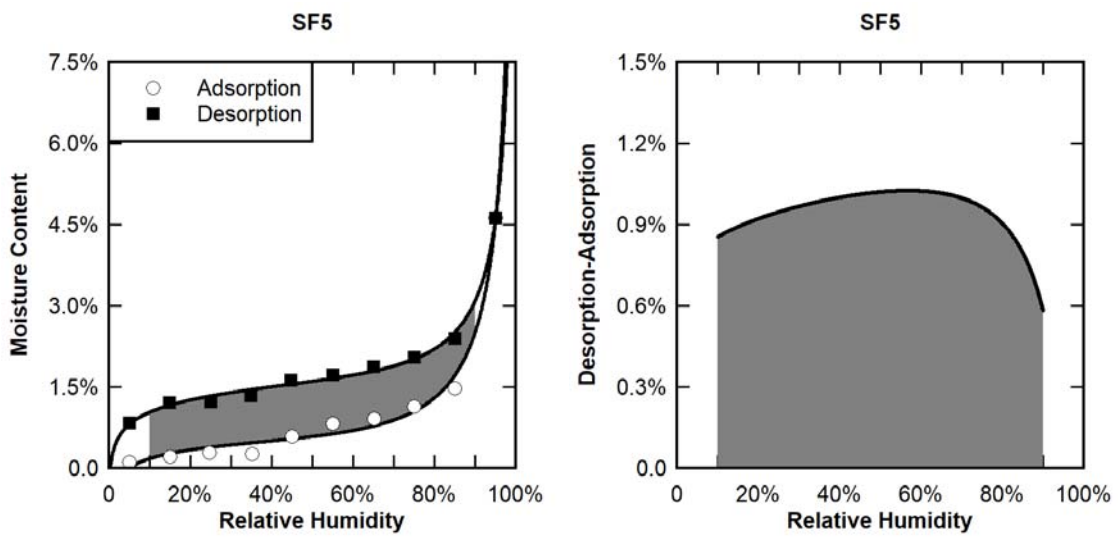


Figure 2.22. Dynamic vapor sorption data (left) and hysteresis area analysis (right) for SF5

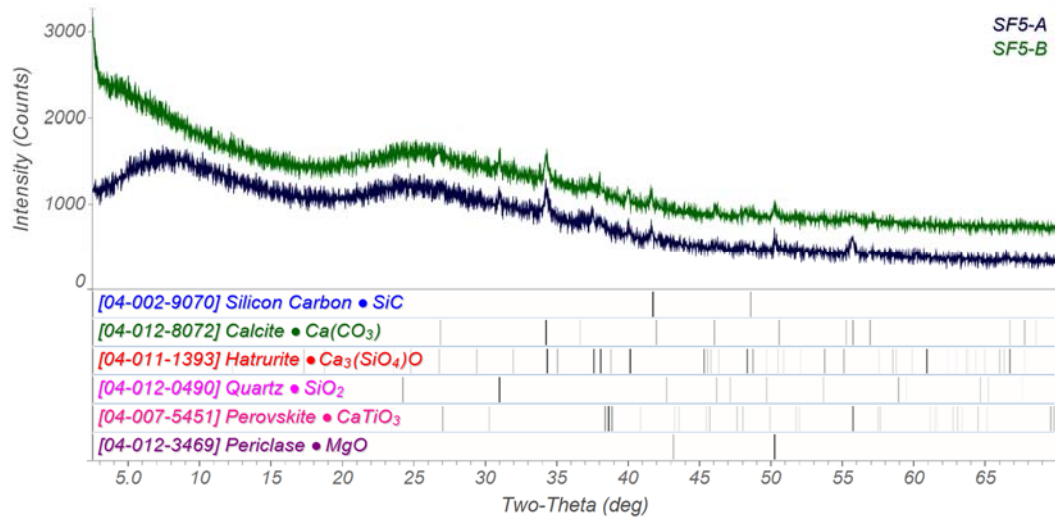


Figure 2.23. XRD patterns for SF5

2.3.4.6 SF6

SF6, shown in Figure 2.24, was a commercially available densified silica fume that was dark gray to black in color. It was commercially marketed as the same product as SF7. Results from dynamic vapor sorption analysis are shown in Figure 2.25. XRD patterns are shown in Figure 2.26. Identified crystalline phases included elemental silicon, quartz, and silicon carbide. SF2, SF4, SF6, and SF7 were found to have very similar mineralogical compositions.



Figure 2.24. SF6

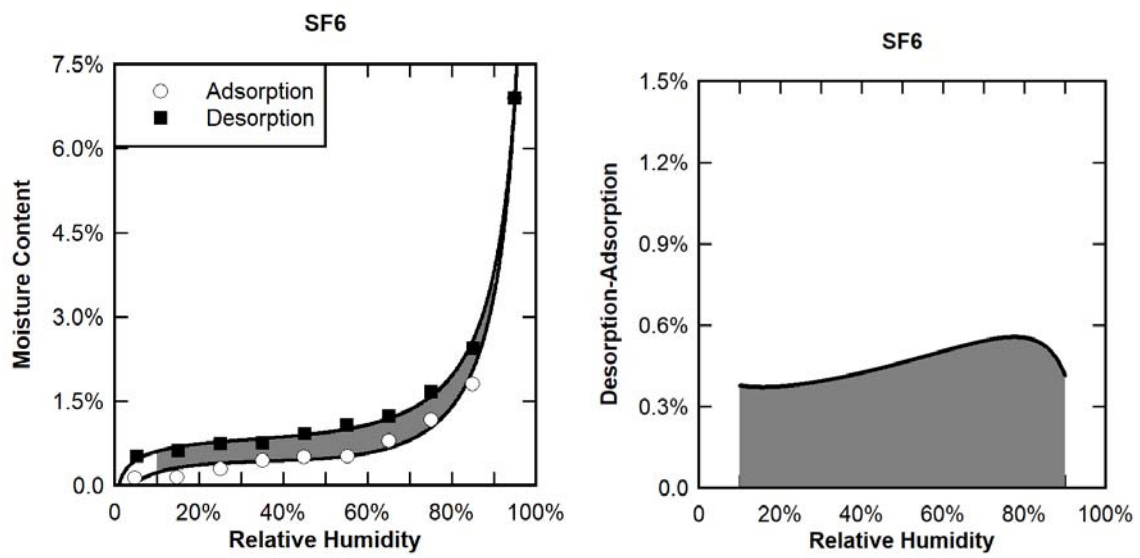


Figure 2.25. Dynamic vapor sorption data (left) and hysteresis area analysis (right) for SF6

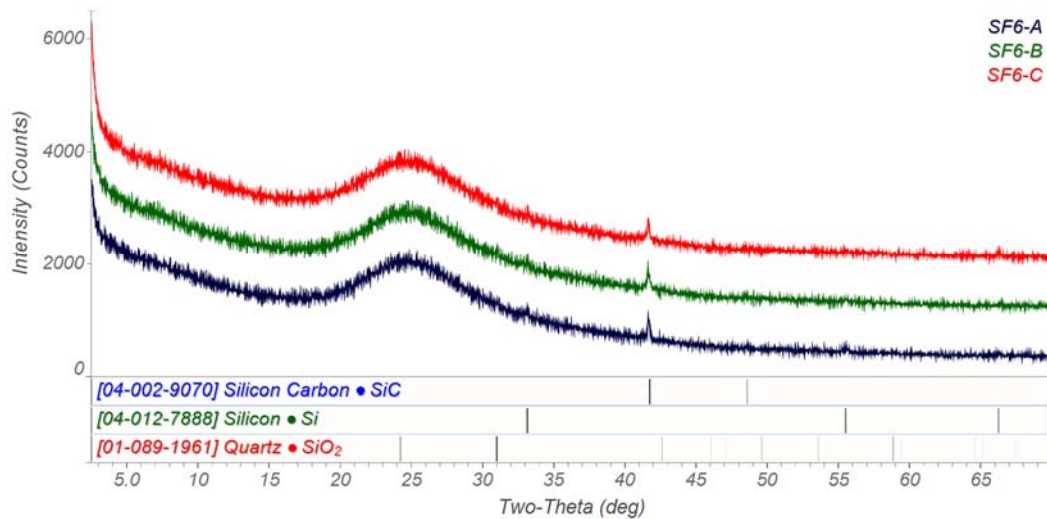


Figure 2.26. XRD patterns for SF6

2.3.4.7 SF7

SF7, shown in Figure 2.27, is a commercially available densified silica fume that is dark gray to black in color. It was commercially marketed as the same product as SF6. Results for dynamic vapor sorption analysis are shown in Figure 2.28. XRD patterns are shown in Figure 2.29.

Identified crystalline phases included elemental silicon, quartz, and silicon carbide. SF2, SF4, SF6, and SF7 were found to have very similar mineralogical compositions.

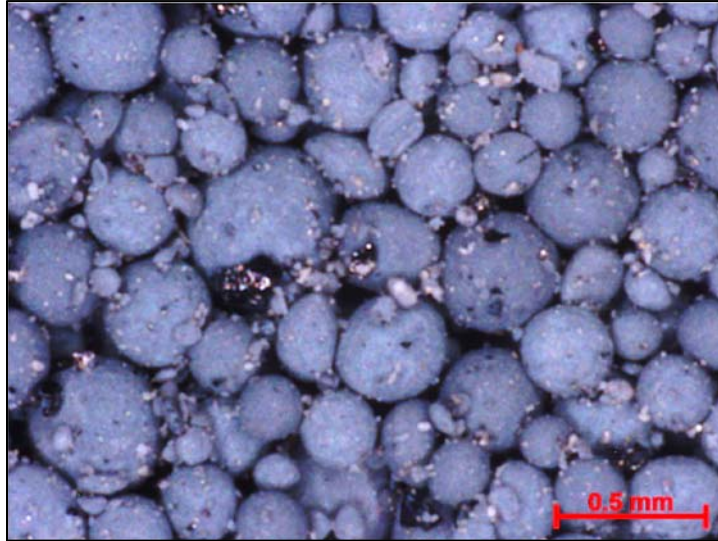


Figure 2.27. SF7

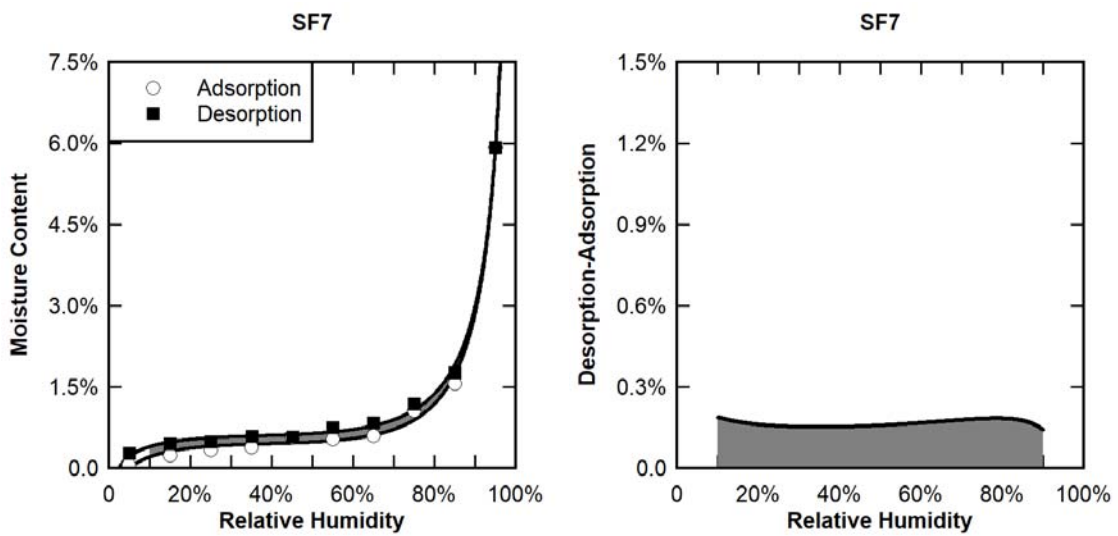


Figure 2.28. Dynamic vapor sorption data (left) and hysteresis area analysis (right) for SF7

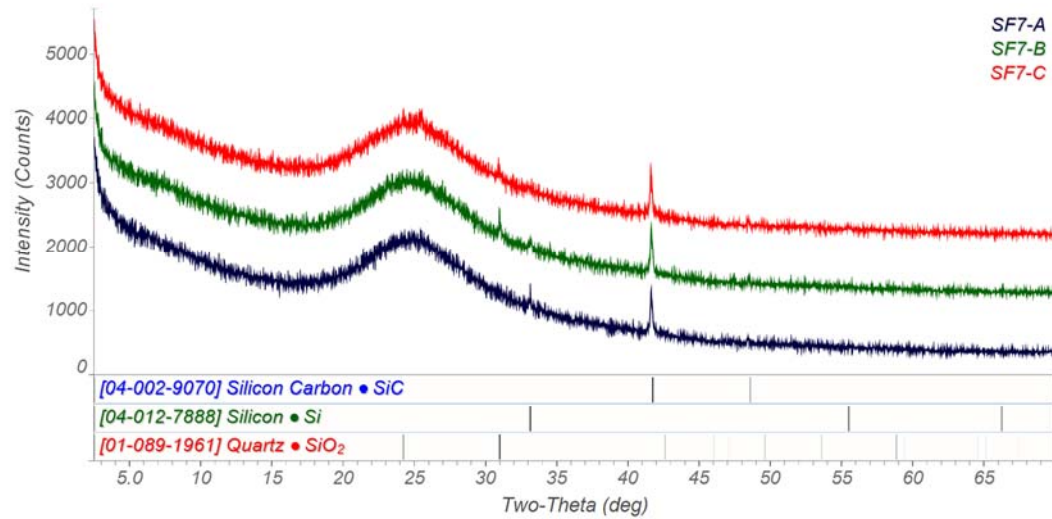


Figure 2.29. XRD pattern for SF7

2.3.4.8 SF8

SF8, shown in Figure 2.30, was a commercially available densified silica fume that was dark gray in color. It was produced at the same industrial plant and commercially marketed as the same product as SF5. Representative results for dynamic vapor sorption analysis are shown in Figure 2.31. Additional dynamic vapor sorption analyses for multiple replicates of SF8 are included in Appendix C. An XRD pattern is shown in Figure 2.32. Identified crystalline phases included calcite, hatrurite, lime, moganite, and silicon carbide. As expected from XRF spectroscopy, multiple calcium-containing phases were present in SF8, including calcite, lime, and hatrurite, which is a cementitious phases similar to C₃S. The presence of such phases further suggested hydraulic reactivity. The identification of moganite and lime were unique to SF8.

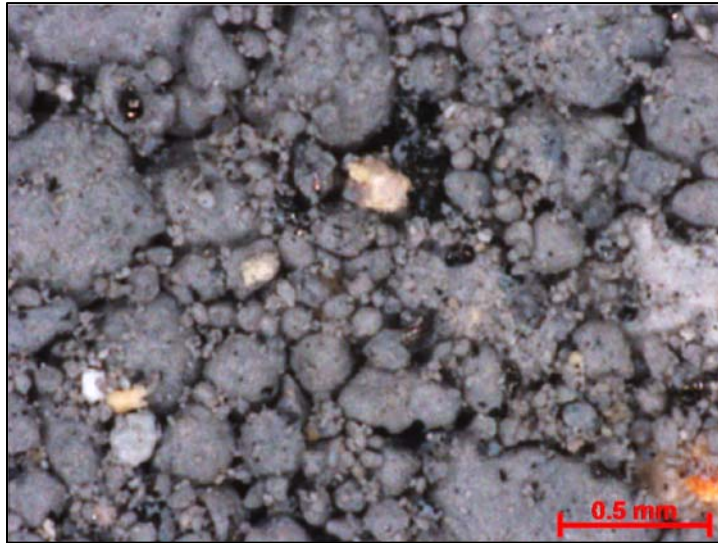


Figure 2.30. SF8

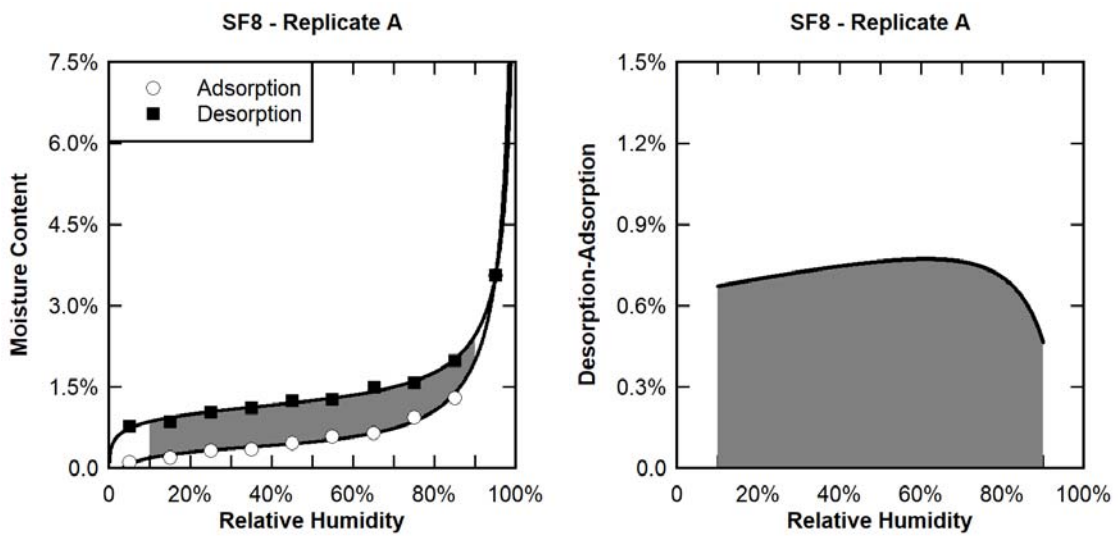


Figure 2.31. Representative dynamic vapor sorption data (left) and hysteresis area analysis (right) for SF8

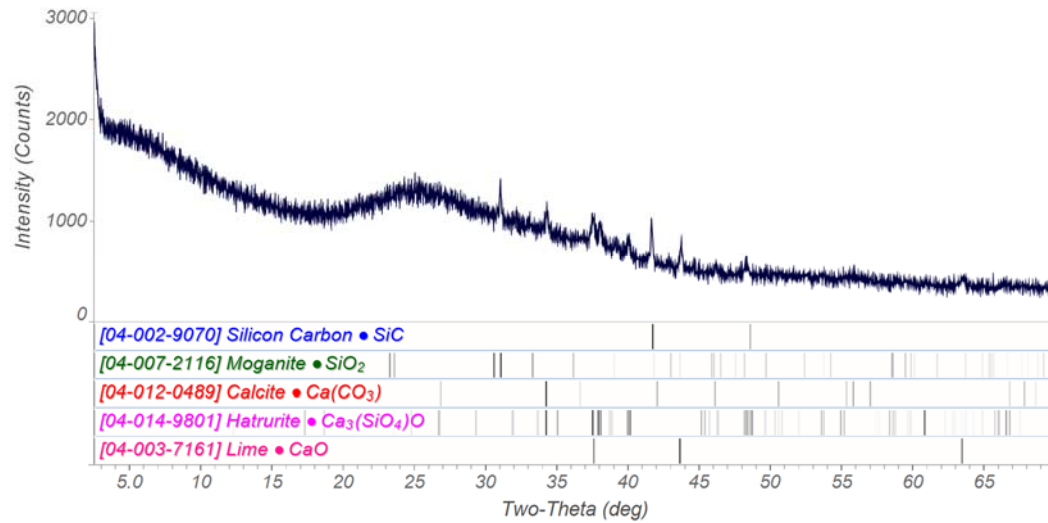


Figure 2.32. XRD pattern for SF8

2.4 Conclusions

Eight different commercially available silica fumes were characterized for their chemical and physical properties. Included in these eight silica fumes were three undensified silica fumes and five densified products. Furthermore, two of the silica fumes, SF6 and SF7, were commercially marketed as the same product; however, they were produced at different industrial facilities. Additionally, two of the silica fumes, SF5 and SF8, were commercially marketed as the same silica fume and were produced at the same industrial facility; however, they represented different lots of the same material as they were produced at different times.

Physically, minor differences were seen in the density of the particles, with specific gravities ranging from 2.21 to 2.37. Particle size analysis and the BET method were used to analyze the fineness of materials. Stark differences in surface area were seen between silica fumes, with SSA_{BET} ranging from 18 to 30 m²/g. The potential absorptive nature of silica fume particles

were analyzed by four approaches, as there is no existing standard for testing this material property with silica fumes. Each of the methods showed that silica fume particles would absorb various amounts of water. Statistical analysis and dynamic vapor sorption were seen as the most promising techniques, as vacuum filtration most likely overestimated the absorption capacity and atmospheric absorption was a very lengthy test method. As statistical approximation was simply an estimation method, dynamic vapor sorption is recommended for characterization in future studies.

Chemically, silica (SiO_2) was the predominant phase in each of the fumes tested, as expected. SF5 and SF8 also showed high levels of CaO, making these materials potentially hydraulic. Quantitative XRD analysis showed that at least 88% of each material was amorphous, which is assumed necessary for reactivity. Densified silica fumes had higher levels of carbon impurities than undensified silica fumes as seen through LOI testing.

3. HYDRATION EFFECTS

Portions of the following section contain text and/or figures and tables to be submitted in **J.F. Burroughs**, C.A Weiss, Jr., J.D. Shannon, J.E. Haddock, and W.J. Weiss, “Modeling the influence of changes in silica fume on concrete performance,” *Journal of Materials in Civil Engineering*, in preparation.

3.1 Calorimetry Experiments

Isothermal calorimetry measures the energy, in the form of heat, released over time by a reaction at constant temperature. Because cement hydration is a highly exothermic reaction, these methods are widely used in cement research. To study the reactivity of each silica fume, idealized pozzolanic reactivity experiments, developed by Oregon State University [21], were performed using isothermal calorimetry methods. In this test method, each silica fume was blended with calcium hydroxide [Ca(OH)₂] at 1:3 by mass. The combined solid mass was then blended with a potassium hydroxide (KOH) solution at 10:9 by mass. A mass ratio mixture proportion for this test method is shown in Table 3.1. Isothermal calorimetry was then performed at 50°C for 10 days.

Table 3.1. Idealized pozzolanic reactivity mixture proportion

Component	Mass Ratio
Silica Fume	1
Ca(OH) ₂	3
KOH Solution	3.6

Figure 3.1 shows representative plots of the normalized heat flow for each of the silica fumes tested over the first 24 hours. Each figure is plotted on identical axes to facilitate comparison.

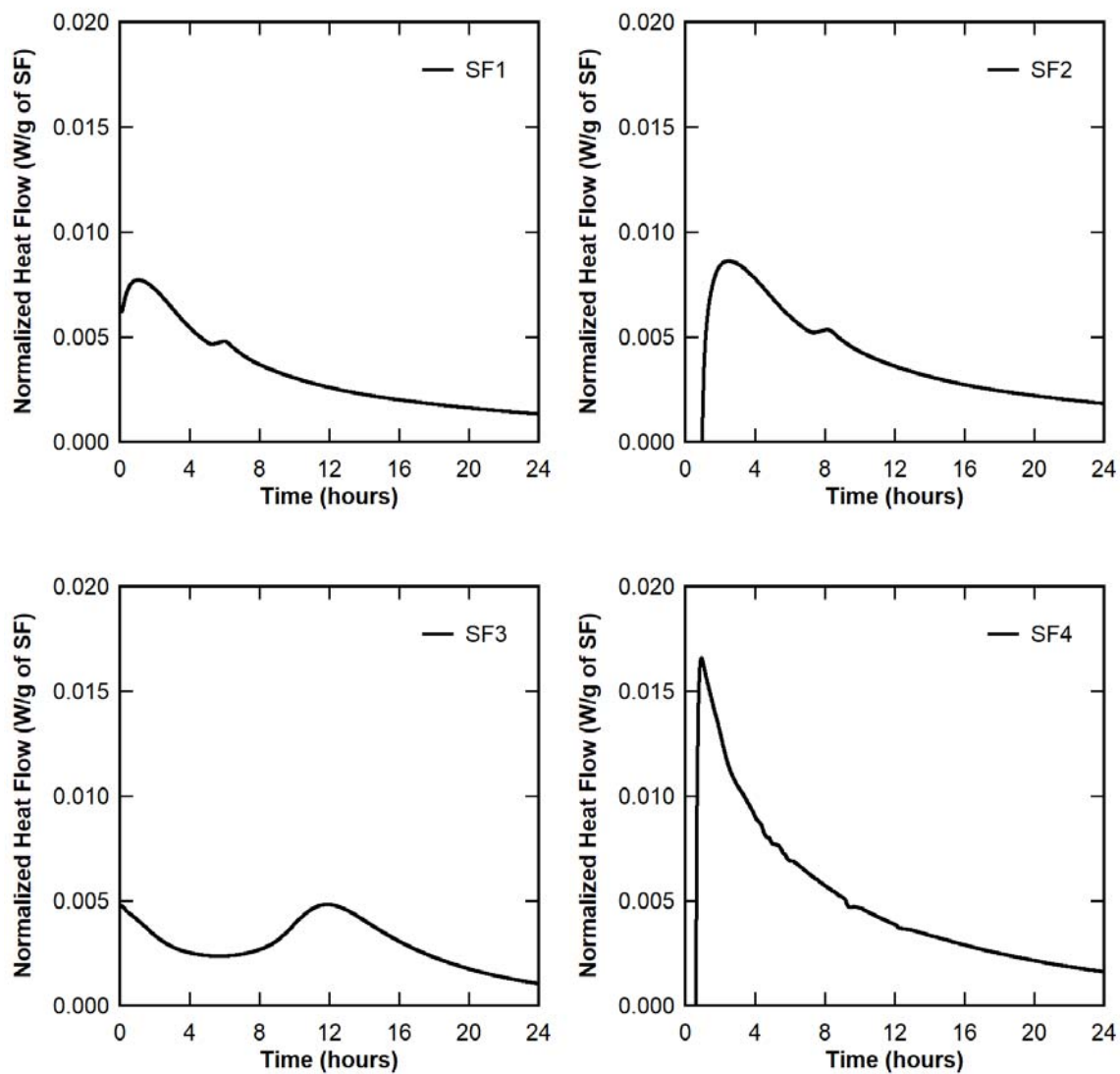
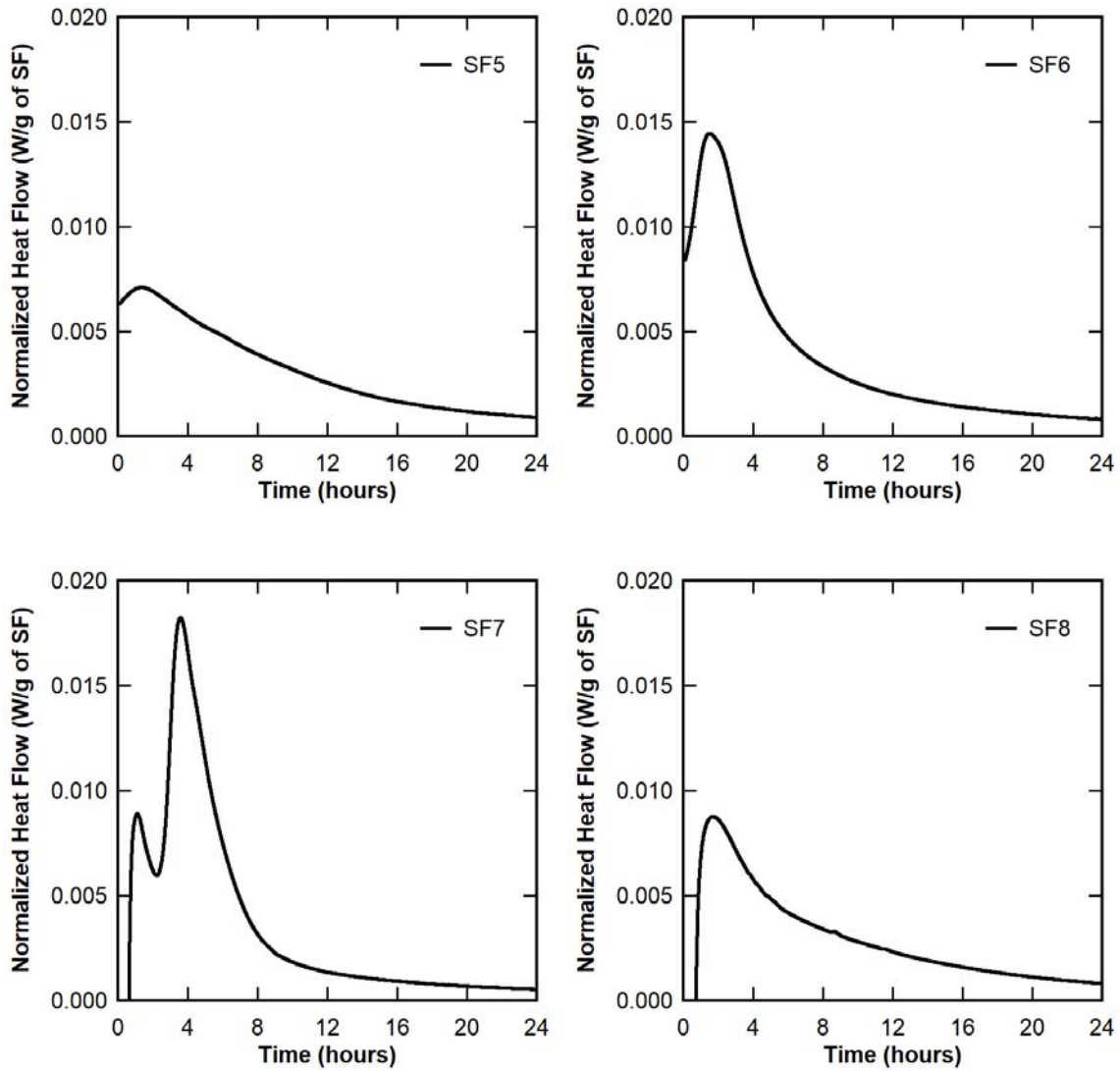


Figure 3.1. Normalized heat flow plots from isothermal calorimetry experiments

Figure 3.1 continued



SF1, SF2, SF5, and SF8 show the most similar behavior over the first 24 hours. A comparative plot of these four silica fumes is included in Figure 3.2. The initial hydration peaks for SF1 and SF5 occurred at very similar times (61.6 and 82.3 minutes respectively), suggesting similar rates of reaction. The initial hydration peaks for SF2 and SF8 occurred slightly later at 147 and 102 minutes, respectively. Additionally, SF1 and SF5 had similar magnitudes of their initial hydration peaks, while SF2 and SF8 had slightly greater magnitudes. SF5 and SF8 exhibited faster decay rates from their initial peaks than SF1 and SF2.

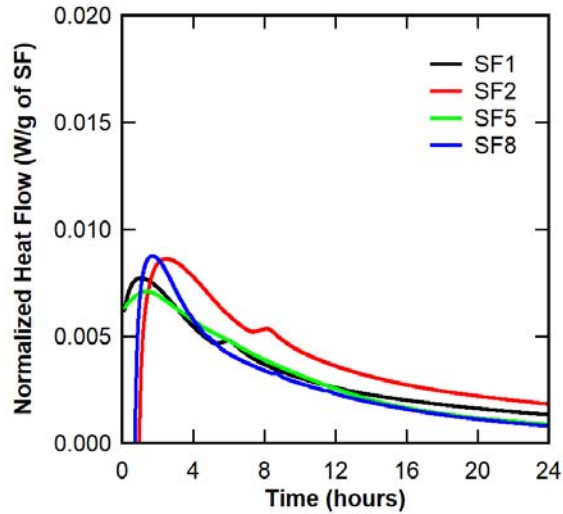


Figure 3.2. Heat flow comparison – SF1, SF2, SF5, and SF8

SF1 and SF2 both exhibited a second minor hydration peak that was not seen in SF5 and SF8. The second hydration peak for SF1 occurred approximately two hours before the second hydration peak in SF2. The cause for this second hydration peak is unknown. One possible explanation for this second hydration peak is incomplete initial dissolution of agglomerations. If aggregated particles were still present during the initial hydration stage, the initial peak magnitude could be reduced because the reactive silica was not exposed to Ca(OH)_2 . As the unreacted silica became exposed to Ca(OH)_2 after initial hydration, a secondary peak could be expected. Another possible explanation is the depletion of sulfate from the system as gypsum was not included in these tests.

Analysis of the remaining silica fumes shows that, with the exception of SF3, the initial hydration peaks for the other seven silica fumes occurred between 50 and 150 minutes. SF3 displayed starkly different behavior with the initial hydration peak not occurring until after 700 minutes after an extended dormant period. A very prominent second hydration peak was seen in

SF7 than was not seen in any of the other silica fumes, which could suggest very poor initial dissolution. As previously discussed, characterization data suggested that SF7 was a highly densified silica fume. The level of densification could have influenced the ability of this silica fume to disagglomerate. SF4, SF6, and SF7 had the greatest magnitudes of hydration peaks, thereby indicating more rapid reaction. These peaks were also sharper than observed in other silica fumes, meaning the majority of the reactive phases were reacting at similar times. Broader peaks like those seen in SF3 and SF5 suggest the reactive phases were reacting over longer periods of time.

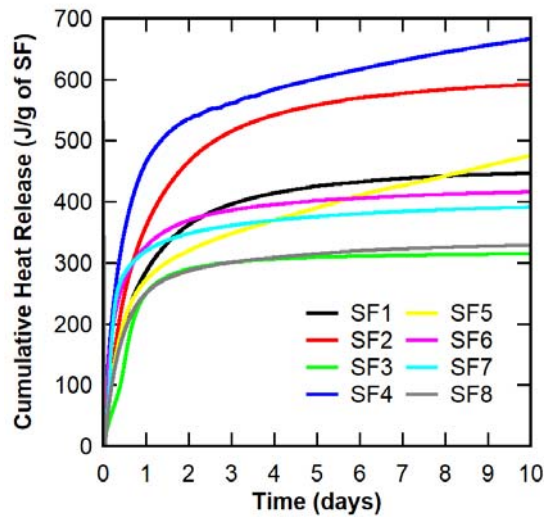


Figure 3.3. Normalized heat release from idealized pozzolanic reactivity tests

Through the integration of the heat flow data (Figure 3.1) as a function of time, cumulative heat release curves (shown in Figure 3.3) can be generated to examine the total energy released from the exothermic reactions. As is shown, undensified silica fumes tended to have a greater cumulative heat release than densified silica fumes, as the three undensified silica fumes have three of the four greatest cumulative heat release values. The exception is SF5, shown in yellow, which never reached an approximately constant value over the 10-day period like the other silica

fumes did. This suggests that SF5 was reactive over a longer time than used in these tests, unlike than the other silica fumes. Considerable differences were observed in the performance of different silica fumes, even for those fumes that were measured to be chemically or physically similar. As emphasis of this point, a 40% increase in the cumulative heat released was observed between SF5 and SF8, even though they were chemically very similar. Additionally, variability was also observed for materials of similar average size. For example, SF4 generated approximately 70% more cumulative heat than SF7, even though their average particle sizes were less one nanometer different.

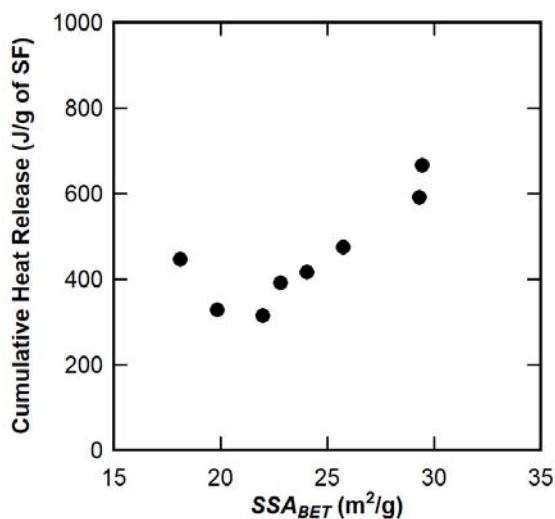


Figure 3.4. Comparison of specific surface area and cumulative heat release

In general, cumulative heat release was associated with BET specific surface area, as shown in Figure 3.4. As specific surface area increased, the cumulative heat released increased as well. This relationship follows the classic chemical understanding that increased surface area leads to increased reactivity. The exception was SF1, which had the lowest surface area but average heat release.

3.2 Hydration Modeling

Hydration modeling was used to predict the volume of hydration products and final degree of hydration for cement pastes containing silica fume. Many published hydration models were considered, but this study focused on expanding the Powers-Brownyard Model to include the effects of silica fume. Once volumes of hydration products were estimated from the Powers-Brownyard Model, a descriptive parameter for each mixture proportion (t_{paste}) was defined as the thickness of hydration products surrounding all unhydrated, unreacted, and inert particles in the cementitious system. The following sections describe the theoretical development and calculation of t_{paste} for a cementitious system containing silica fume.

3.2.1 Powers-Brownyard Model Expansion

The Powers-Brownyard Model for cement hydration, used to algebraically estimate hydration products from degree of hydration (α), was originally published in the 1940s [32]. This model, shown in Equations 3 through 9, was developed specifically for modeling the hydration of neat cement paste. Many times in the literature, f_{water} has been represented by p as the initial porosity of the mixture, and f_{cement} is represented as $1 - p$. While this approach is certainly accurate, it may be easier to understand the inputs for the model if the volume fractions of cement and water (f_{cement} and f_{water}) from the mixture proportion are used instead. These inputs can be directly calculated from the mixture proportion.

$$V_c = f_{cement}(1 - \alpha) \quad (3)$$

$$V_{gs} = (1 - \Delta V_c \rho_c + w_{n,c} \rho_c / \rho_w) f_{cement} \alpha \quad (4)$$

$$V_{gw} = w_{gw,c} \rho_c / \rho_w f_{cement} \alpha \quad (5)$$

$$V_{cw} = f_{water} - (w_{gw,c} + w_{n,c}) \rho_c / \rho_w f_{cement} \alpha \quad (6)$$

$$V_{cs} = \Delta V_c \rho_c f_{cement} \alpha \quad (7)$$

$$f_{cement} = \frac{V_{cement}}{V_{cement} + V_{water}} \quad (8)$$

$$f_{water} = \frac{V_{water}}{V_{cement} + V_{water}} \quad (9)$$

Other model inputs include the volumetric change due to chemical shrinkage (ΔV_c), the amount of nonevaporable water formed through hydration ($w_{n,c}$), and the amount of water trapped in gel pores in CSH ($w_{gw,c}$). Brouwers [67] demonstrated how to estimate these model parameters from the Bogue phase composition of the cement used. ASTM C150 [68] defines how to convert the chemical composition as determined by ASTM C114 [69] or by XRF to the Bogue phases composition, as shown in Equations 10 through 17. In order to determine the model input following the Brouwers method, it is also necessary to estimate the amount of anhydrite ($C\bar{S}$) in the cement. Equation 18, as reported by Stutzman et al. [70], was used to calculate the anhydrite content.

$$\text{If } \frac{Al_2O_3}{Fe_2O_3} \geq 0.64$$

$$C_3S = 4.071CaO - 7.600SiO_2 - 6.718Al_2O_3 - 1.430Fe_2O_3 - 2.852SO_3 \quad (10)$$

$$C_2S = 2.867SiO_2 - 0.7544C_3S \quad (11)$$

$$C_3A = 2.650Al_2O_3 - 1.692Fe_2O_3 \quad (12)$$

$$C_4AF = 3.043Fe_2O_3 \quad (13)$$

$$\text{If } \frac{Al_2O_3}{Fe_2O_3} < 0.64$$

$$C_3S = 4.071CaO - 7.600SiO_2 - 4.479Al_2O_3 - 2.859Fe_2O_3 - 2.852SO_3 \quad (14)$$

$$C_2S = 2.867SiO_2 - 0.7544C_3S \quad (15)$$

$$C_3A = 0 \quad (16)$$

$$ss(C_4AF + C_2F) = 2.100Al_2O_3 + 1.702Fe_2O_3 \quad (17)$$

$$C\bar{S} = 1.7004SO_3 \quad (18)$$

Using Equations 14 through 18, the Bogue phase composition for the Class H cement used in this study is shown in Table 3.2. Following the procedure outlined by Brouwers, the model input parameters used for cement in this study are as follows:

- $\Delta V_c = 6.6 \text{ mL}/100 \text{ g}$ of cement reacted
- $w_{n,c} = 0.17 \text{ g/g}$ of cement reacted
- $w_{gw,c} = 0.17 \text{ g/g}$ of cement reacted

Table 3.2. Bogue composition of Class H cement

Phase	Content (%)
C_3S	62.5
C_2S	16.2
C_3A	0
$ss(C_4AF + C_2F)$	13.2
$C\bar{S}$	4.8
Balance	3.3

The Powers-Brownyard Model can also be used to estimate final degree of hydration (α_∞). This occurs when either the amount of water available for reaction (V_{cw}) or the volume of unhydrated cement (V_c) equals zero. If V_c reaches zero before V_{cw} , there is excess water in the system than is necessary for hydration. If V_{cw} reaches zero before V_c , the mixture is described as water-starved. This means that insufficient water is available to fully hydrate all of the cement in the mixture. Calculations from the Powers-Brownyard Model can be used to create phase diagrams for each stage of hydration as shown in Figure 3.5 for three different w/c. These phase diagrams can be used to evaluate the evolution of phases as the cement hydrates.

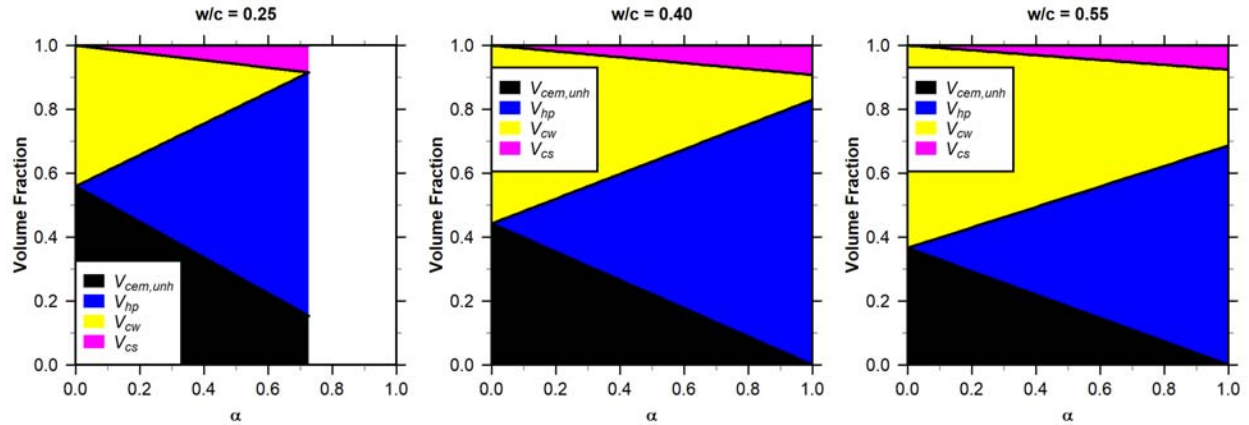


Figure 3.5. Example phase diagrams from Powers-Brownyard Model for neat cement paste

In order to use the Powers-Brownyard Model for cement pastes containing silica fume, the Powers-Brownyard Model has to be expanded. This model expansion, shown in Equations 19 through 27, has previously been published in the literature [34], but it is presented here in the same format as was used with the Powers-Brownyard Model for neat cement paste. Here, f_{fume} is the volumetric proportion of silica fume in the mixture proportion, which can be calculated directly from the mixture proportion. Model terms with a subscript s refer to the equivalent term in the neat cement paste model for silica fume. Additional input parameters for silica fume were taken from the published literature [34]:

- $\Delta V_s = 20 \text{ mL}/100 \text{ g}$ of silica fume reacted
- $w_{n,s} = 0 \text{ g/g}$ of silica fume reacted
- $w_{gw,s} = 0.50 \text{ g/g}$ of silica fume reacted

These input parameters were assumed constant for all silica fumes studied, even though idealized pozzolanic reactivity testing showed that not all silica fumes react identically. As such, refinement of the input parameters for each specific silica fume would further improve this model in future studies. As before, hydration continues until either V_{cw} or V_c reaches zero. This approach assumes that cement and silica fume are equally likely to react. Put another way, the

degree of hydration of cement is always equal to the degree of reaction for silica fume. This is expressed mathematically in Equation 28.

$$V_c = f_{cement}(1 - \alpha) \quad (19)$$

$$V_s = f_{fume}(1 - \alpha) \quad (20)$$

$$V_{gs} = [(1 - \Delta V_c \rho_c + w_{n,c} \rho_c / \rho_w) f_{cement} + (1 - \Delta V_s \rho_s + w_{n,s} \rho_s / \rho_w) f_{fume}] \alpha \quad (21)$$

$$V_{gw} = (w_{gw,c} \rho_c / \rho_w f_{cement} + w_{gw,s} \rho_s / \rho_w f_{fume}) \alpha \quad (22)$$

$$V_{cw} = f_{water} - [(w_{gw,c} + w_{n,c}) \rho_c / \rho_w f_{cement} + (w_{gw,s} + w_{n,s}) \rho_s / \rho_w f_{fume}] \alpha \quad (23)$$

$$V_{cs} = (\Delta V_c \rho_c f_{cement} + \Delta V_s \rho_s f_{fume}) \alpha \quad (24)$$

$$f_{cement} = \frac{V_{cement}}{V_{cement} + V_{fume} + V_{water}} \quad (25)$$

$$f_{fume} = \frac{V_{fume}}{V_{cement} + V_{fume} + V_{water}} \quad (26)$$

$$f_{water} = \frac{V_{water}}{V_{cement} + V_{fume} + V_{water}} \quad (27)$$

$$\alpha_c = \alpha_s = \alpha \quad (28)$$

Phase diagrams similar to those for neat cement paste can be generated for the expanded model as well. Example phase diagrams at the same w/c with 10% silica fume are shown in Figure 3.6.

Phase diagrams including inert phases for each mixture tested in this study are included in Appendix D.

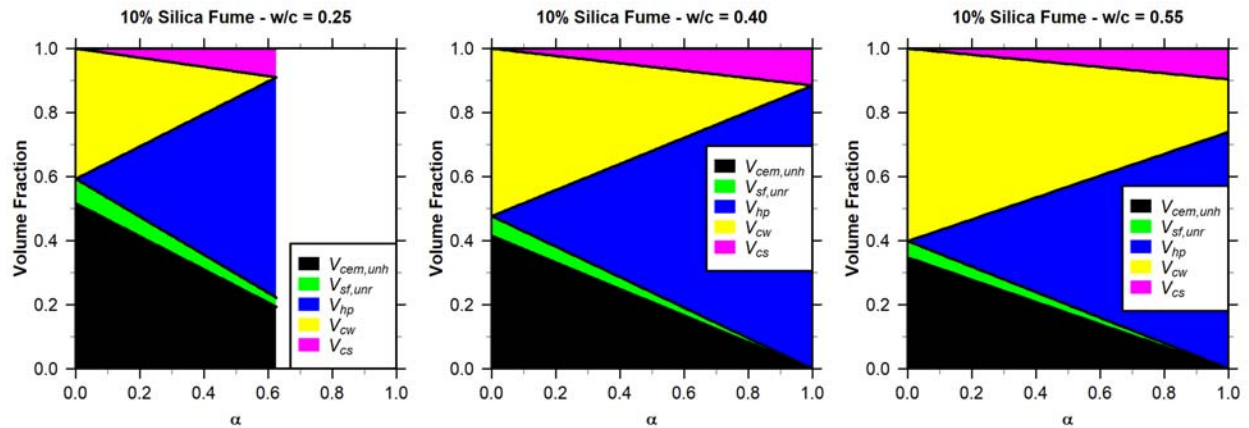


Figure 3.6. Example phase diagrams from Powers-Brownyard Model for cement paste with 10% silica fume

Comparing Figure 3.5 with Figure 3.6, less hydration occurs when silica fume is present at equivalent w/c. This is further supported by Figure 3.7, which shows a reduction in α_∞ for a constant w/c as the silica fume content is increased. Put another way, significantly more water is necessary to fully hydrate the cement when high volumes of silica fume are included in the mixture proportion. Additionally, Figure 3.6 shows an increase in the volume of hydration products (V_{hp}) and chemical shrinkage (V_{cs}) when silica fume is included.

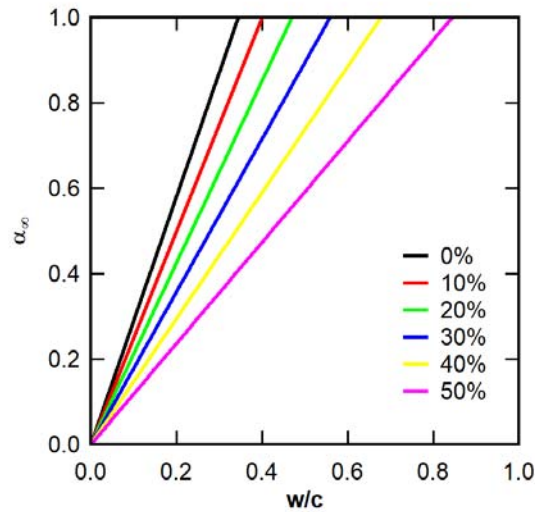


Figure 3.7. Effect of silica fume content on α_∞ for different w/c

3.2.2 Reduction of Surface Area

As previously discussed, many concrete mixture proportions, especially those designed for high strength or high performance, are water-starved and do not have enough water to fully hydrate all of the cement or fully react all of the silica fume in the system. As shown in the previous section, the expanded Powers-Brownyard Model allows for the calculation of how much unhydrated cement and unreacted silica fume remain in the system at α_∞ . These unhydrated and unreacted particles simply fill volume and provide no chemical benefit to the system. In other

words, unhydrated cement and unreacted silica fume serve the function of inert fillers and aggregates in water-starved systems. In order to determine the surface area of unhydrated and unreacted particles in the system that will be necessary inputs in an analytical model mentioned above and described in detail in later sections, the following method was used to calculate the reduced surface area. This method assumes that all particles are spherical, that the volume of each particle reduces diametrically with hydration, and that the volume of each particle reduces by same percentage. Figure 3.8 shows a schematic of the reduction in surface area. The areas shaded in dark gray indicate hydrated area, whereas areas in light gray are unhydrated. The mathematical calculation of the reduced surface area is described in Equations 29 through 35.



Figure 3.8. Reduction of particle surface area with hydration

$$V_1 = \frac{4}{3}\pi r_1^3 \quad (29)$$

$$V_2 = \frac{4}{3}\pi r_2^3 \quad (30)$$

$$V_2 = (1 - \alpha)V_1 \quad (31)$$

$$\frac{4}{3}\pi r_2^3 = (1 - \alpha)\frac{4}{3}\pi r_1^3 \quad (32)$$

$$r_2^3 = (1 - \alpha)r_1^3 \quad (33)$$

$$r_2 = \sqrt[3]{(1 - \alpha)r_1^3} \quad (34)$$

$$A_{s,2} = 4\pi r_2^2 \quad (35)$$

Figure 3.9 shows what effects hydration and reaction have on the specific surface area of cement and each silica fume tested. Note that the scales on the y-axes of each graph are very different as the specific surface area of silica fume is much greater than that of cement. With both materials,

the specific surface area approaches infinity as the degree of hydration approaches one. At $\alpha = 1$, all of the cement and silica fume has reacted; therefore, no unreacted mass remains for the specific surface area calculation. The denominator goes to zero, and the specific surface area goes to infinity. With adjusted surface areas for reactive components, a more realistic calculation of the total unhydrated surface area can be performed.

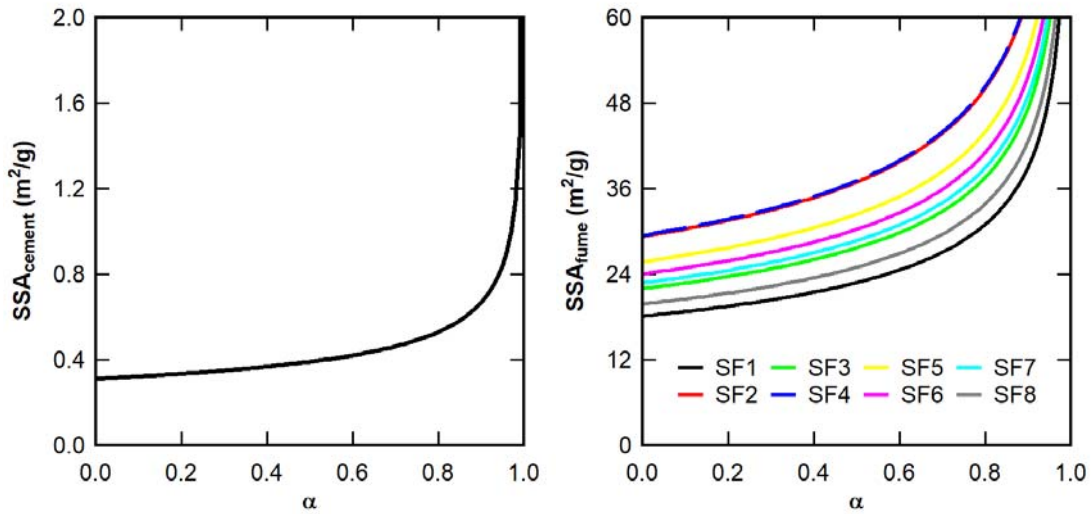


Figure 3.9. Evolution of specific surface area of cement and silica fume with hydration

3.2.3 Paste Thickness Model

Once volume fractions of hydration products are estimated from the expanded Powers-Brownyard Model and the reduced surface area of cement and silica fume are calculated, t_{paste} can be determined for a concrete or cementitious mixture. The volume fraction of gel water (V_{gw}) and gel solids (V_{gs}) calculated from the Powers-Brownyard Model are converted to actual volumes of gel water ($V_{gw,total}$) and gel solids ($V_{gs,total}$) by multiplying the volume fraction by the initial volume of paste that can be calculated from the mixture proportion, as shown in Equations 36 through 38. These phases represent the entirety of hydration products in water-starved materials. In cementitious materials with excess water, the volume of capillary water

($V_{cw,total}$) must be included as well. The calculation of this term is described by Equation 39.

Combining these phases using Equation 40, the total volume of hydration products

($V_{hydration\ products}$) can be calculated.

$$V_{paste,total} = V_{cement} + V_{fume} + V_{water} = \frac{m_c}{\rho_c} + \frac{m_s}{\rho_s} + \frac{m_w}{\rho_w} \quad (36)$$

$$V_{gw,total} = V_{gw}V_{paste,total} \quad (37)$$

$$V_{gs,total} = V_{gs}V_{paste,total} \quad (38)$$

$$V_{cw,total} = V_{cw}V_{paste,total} \quad (39)$$

$$V_{hydration\ products} = V_{gw,total} + V_{gs,total} + V_{cw,total} \quad (40)$$

To calculate t_{paste} , the volume of hydration products is distributed over the total remaining surface area after corrections have been made for reactive components. This is mathematically described in Equation 41. This calculation assumes that all unreacted and inert particles are perfectly distributed in the system and surrounded by an equal thickness of paste. Because this assumption is difficult to satisfy in practice, t_{paste} serves as a bulk descriptor for the entire material rather a parameter that can be directly measured optically. In other words, it is unlikely that a measurement of actual paste thickness with a microscope would always be equal to t_{paste} . As a bulk descriptor, the average thickness measured around an infinite number of particles should approach t_{paste} .

$$t_{paste} \equiv \frac{V_{hydration\ products}}{A_{s,total,after\ hydration}} = \frac{V_{hydration\ products}}{A_{s,cem,unh} + A_{s,sf,unr} + A_{s,ss} + A_{s,sp}} \quad (41)$$

3.2.3.1 Comparison to Similar Models

The Paste Thickness Model developed in this study is somewhat similar to the paste film thickness described by Li and Kwan [55]; however, the Li and Kwan model only focused on traditional concretes containing only cement and aggregates. Additionally, the calculated paste

content was not based on the hydration of the cement, and no correction was made in that model for the unhydrated cement particles that exist in water-starved mixture proportions. Furthermore, the Li and Kwan model only considered paste in excess of the porosity between aggregates, whereas the Paste Thickness Model presented here includes all paste that is generated by hydration.

3.3 Application of Paste Thickness Model

To study the applicability of t_{paste} in describing behavior in concrete, 82 batches of concrete were analyzed. Each of the batches analyzed contained cement, silica sand, silica powder, silica fume, HRWRA, and water. The mixing procedure was follows:

1. All of the silica fume, silica sand, and water were blended on low for 10 minutes to try and break up silica fume agglomerations.
2. Cement and silica powder were added to the mixer and blended on low for 30 seconds.
3. HRWRA was added over the next 30 seconds with the mixer running. Mixing continued for four additional minutes.
4. The mixture was allowed to rest for 60 seconds.
5. The mixture was blended on low for an additional five minutes.
6. The mixture was allowed to rest for 60 seconds.
7. The mixture was blended on medium for two minutes.
8. The mixture was blended on low for three minutes.

The minimum and maximum loading of constituents used in mixture proportions is shown in Table 3.3. The compressive strength of 50-mm cubes was tested in accordance with ASTM

C109 [71] after curing for seven days at 25°C and 100% RH using a universal testing machine with a maximum load capacity of 1950 kN.

Table 3.3. Range of mixture proportions

Constituent	Minimum	Maximum
Cement	557 kg/m ³	1030 kg/m ³
Silica Sand	676 kg/m ³	1088 kg/m ³
Silica Powder	37 kg/m ³	311 kg/m ³
Silica Fume	224 kg/m ³	432 kg/m ³
w/c	0.19	0.32
w/b	0.14	0.23

3.3.1 Comparing Paste Thickness Model with Experimental Results

Figure 3.10 shows the relationship between the calculated paste thicknesses for each of the 82 batches with the maximum measured compressive strength at seven days. The maximum compressive strength was used because it better describes the upper limit of the compressive strength potential of the mixture proportion. Cubes with lower compressive strength results could be influenced by improper specimen preparation, nonparallel faces for testing, entrapped air, etc. Paste thicknesses are presented as a ratio between the calculated paste thickness of each mixture to the calculated paste thickness of a reference mixture (Mix #41 in Appendix D), denoted as r_{paste} . As t_{paste} increases, r_{paste} also increases. Ratios greater than one indicate that the mixture has a greater paste thickness than the reference mixture. Similarly, the compressive strength results are presented as a ratio, denoted as $r_{strength}$, of the measured compressive strength of each mixture to the measured compressive strength of the reference mixture. The raw data points were binned in 0.075 increments to develop the trendline shown. For example, all data with r_{paste} between 0.9625 and 1.0375 were averaged together in a

$r_{paste} = 1$ bin. The binned averages, plotted as filled black circles in Figure 3.10, are averaged for both compressive strength and t_{paste} .

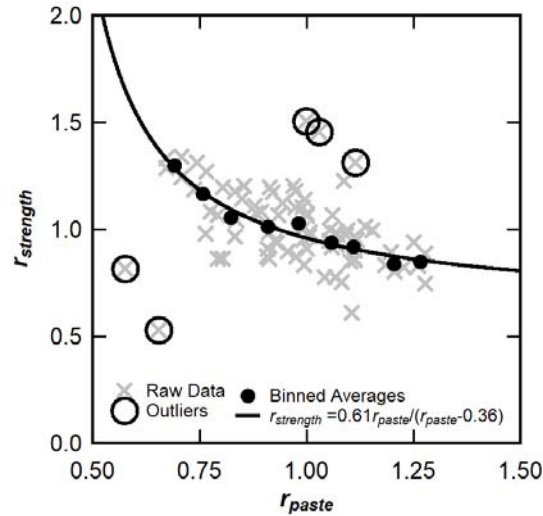


Figure 3.10. Paste thickness model

3.3.2 Discussion of Results

As is shown, a strong asymptotic relationship exists between t_{paste} and the measured compressive strength. Increasing t_{paste} led to a decrease in measured compressive strength. As can be seen, a strong correlation ($R^2 = 0.962$) exists between compressive strength and paste thickness. Another way to consider these results is to visualize t_{paste} as the spacing between aggregates and unreacted components in concrete. Most concrete specimens tend to fail in compression either through the paste phase or along aggregate-paste interfaces. As such, one way to increase compressive strength is to limit the amount of paste phase available for failure. The caveat in this analysis is that a certain amount of paste is required to adequately mix and cement the proportion together. Taken to the extreme, aggregates surrounded by no paste would not have any unconfined compressive strength, as they would not be structurally bonded in any

way. In addition, frictional effects between aggregates would be expected to increase considerably as t_{paste} decreases, making mixing more difficult. Put another way, at some $r_{paste} < 0.6$, a decrease in compressive strength should be expected due to inadequate mixing with $r_{paste} = 0$ having no unconfined compressive strength. The lower limits of this relationship need further study to elucidate the lower part of this curve. Additionally, this relationship is only applicable to concretes that have either reached complete hydration or are at equivalent states of hydration. As shown in Figure 3.11, t_{paste} increases with time because of hydration. At a defined time or at final hydration, concretes with increased t_{paste} would be expected to have reduced compressive strength.

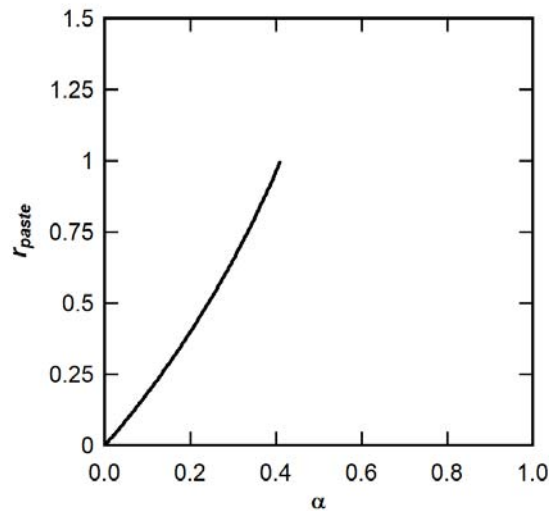


Figure 3.11. Example of paste thickness evolution with hydration

The relationship shown in Figure 3.10 opposes that proposed by Li and Kwan [55], as compressive strength decreased with increasing t_{paste} in this study. As discussed, t_{paste} can be understood as a measure of the spacing between particles in the system. As such, decreased spacing between particles would be analogous to increased particle packing, which has long been known as a method of increasing concrete compressive strength. Furthermore, by reducing the

volume of cementitious phases in a mixture, the volume of unhydrated cement and unreacted silica fume are reduced as well. Reducing the volume of unreacted particles also reduces the likelihood of agglomerations of unreacted particles. Agglomerations of such particles would be expected to have much lower strength than a similar volume of aggregate.

This explanation, however, is only applicable to well-graded distributions of particles. Very poorly graded distributions of inert particles, like those used for pervious concrete, would not be expected to follow this behavior because increasing the paste content could begin to fill some of the porosity formed by the poorly graded aggregates. If the paste content did not fill the aggregate void space, increased paste content could lead to decreased strength in these types of concrete as well.

3.4 Conclusions

Isothermal calorimetry experiments show that silica fumes all react differently. The early age reactivity can vary substantially from one silica fume to another, as shown in Figure 3.1.

Cumulative heat release measurements showed a mild correlation with specific surface area in Figure 3.4, with finer and higher surface area silica fumes generating more heat over time on average than coarser and lower surface area silica fumes. Additionally, undensified silica fumes tended to generate more heat over time than densified silica fumes. Furthermore, an analytical model combining existing hydration models and surface area reduction was used to define a single parameter called t_{paste} that describes the thickness of hydrated paste that surrounds all of the inert and unreacted surface area in a cementitious system. This parameter was shown to correlate strongly with the unconfined compressive strength. As t_{paste} increased, the measured

compressive strength decreased. This occurs because decreased t_{paste} allows for better particle packing between aggregates, thus reducing the critical flaw size and increasing strength.

4. MULTILINEAR RHEOLOGICAL MODEL

Portions of the following section contain text and/or figures and tables previously published in **J.F. Burroughs**, J. Weiss, and J.E. Haddock, “Influence of high volumes of silica fume on the rheological behavior of oil well cement pastes,” *Construction and Building Materials*, vol. 203, pp. 401-407, 2019.

4.1 Rheological Experiments

The initial rheological study was conducted as an $8 \times 3 \times 3$ factorial considering three different treatment factors: silica fume (SF1-SF8), water-to-binder (w/b) (0.20, 0.30, 0.45), and the percentage of total materials dry mass represented by silica fume (10%, 20%, 30%). These treatment factors are shown in Table 4.1 as factors A, B, and C, respectively. For example, for a 30% mixture, 300 g of silica fume would be added to 700 g of cement to create 1000 g of dry materials. This factorial experimental design resulted in 72 distinct combinations to be tested. In all cases, HRWRA B was used at a constant dosage of 3% by total mass of binder.

4.1.1 Methodology

All composites were mixed using a commercial laboratory blender with an attached variable speed controller. Initially, all water, HRWRA, and silica fume were blended on the lowest setting until an approximately homogenous paste was achieved. After the silica fume had been incorporated, all mixing followed the protocol illustrated in Figure 4.1 described as follows:

- I. All cement was added slowly with the blender on the lowest setting over two minutes.
- II. The rotational speed of the blender was increased to 4,000 RPM over 30 seconds.

- III. The paste was blended at 4,000 RPM for 60 seconds.
- IV. The paste was allowed to rest for 30 seconds.
- V. The rotational speed of the blender was increased to 10,000 RPM over 30 seconds.
- VI. The paste was blended at 10,000 RPM for 30 seconds.

Because the rheostat used to control the blender was analog rather than digital, exact rotational speeds could not be achieved; thus, all blending was performed at the approximate rotational speeds listed in the high-shear mixing protocol.

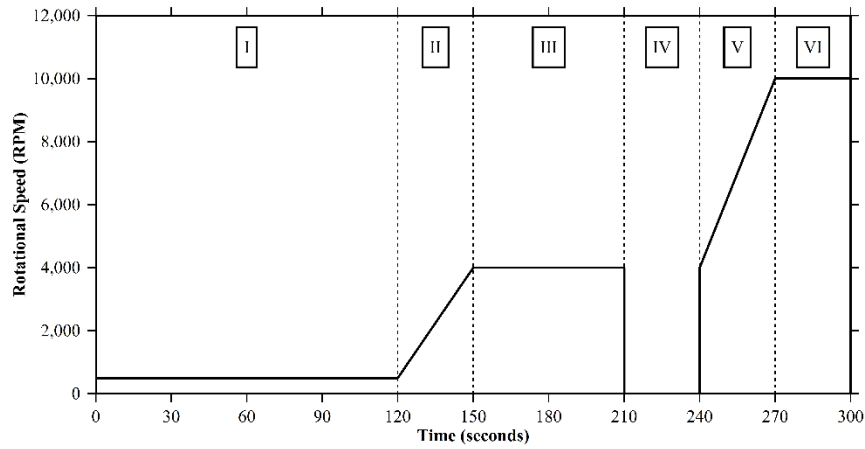


Figure 4.1. High-shear mixing protocol

After the completion of the mixing protocol, paste specimens were added to a rheometer equipped with a cup and paddle analogous to traditional concentric cylinders. According to ASTM C1749 [72], the shear stress and shear rate of a cement paste can be calculated from data collected using a rotational rheometer with concentric cylinders using Equations 42 and 43, respectively.

$$\dot{\gamma} = \frac{R_2 \Omega_1}{R_2 - R_1} \quad (42)$$

$$\tau = \frac{\Gamma}{2\pi R_1^2 L} \quad (43)$$

A Newtonian fluid of known viscosity was used to calculate a virtual inner radius represented by the paddle attachment. The cup was fitted with a cage insert to minimize wall effects. Material was added until the vanes of the cage insert were completely submerged. The material was allowed to rest in the cup for 30 seconds to allow it to fully fill all voids and then pre-sheared at 10 s^{-1} for 30 s to ensure specimen homogeneity. After pre-shearing, the specimen underwent a loading and unloading cycle, loading from 0 to 60 s^{-1} at a rate of $1 \text{ s}^{-1}/\text{s}$ and then unloading from 60 to 0 s^{-1} similarly. In total, each test lasted three minutes, meaning all testing was completed before the pastes reached 10 minutes of age. The unloading curve was used for all rheological characterization, as has been described elsewhere [48]. Example specimen loading and unloading curves are shown in Figure 4.2.

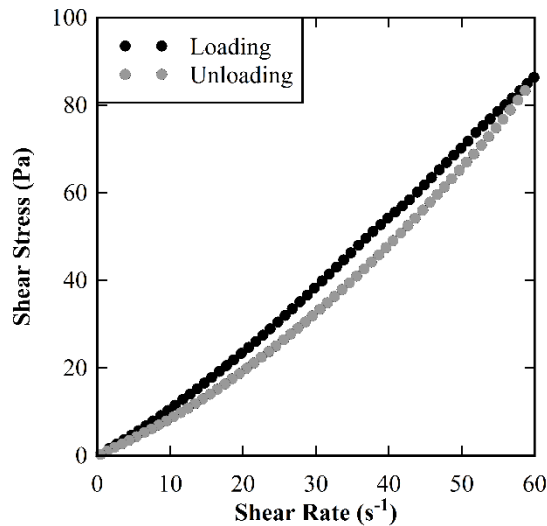


Figure 4.2. Example specimen loading and unloading curves

4.1.2 Herschel-Bulkley Model

Raw data from rheological experiments were fit by the Herschel-Bulkley model to characterize the rheological behavior. The Herschel-Bulkley model, shown in Equation 44, is a three-parameter model that relates shear stress (τ) and shear rate ($\dot{\gamma}$).

$$\tau = \tau_0 + k\dot{\gamma}^n \quad (44)$$

Consistency (k) is analogous to viscosity in most commonly known rheological models for Newtonian and Bingham plastic fluids. In other words, a higher consistency paste can be described as being more viscous. Rate indices (n) greater than one indicate that the material is shear thickening, whereas rate indices less than one indicate shear-thinning behavior. In the case where $n = 1$, the Herschel-Bulkley model reduces to the Bingham plastic model. Practically, pastes with rate indices approaching two are easier to mix than those with rate indices closer to one. As the rate index falls below one, mixing the paste becomes much more difficult.

While the raw data collected during rheological testing were able to be fit well with the three-parameter Herschel-Bulkley model, there are certain drawbacks when using the model. First, the fitting process can result in a slightly negative yield stress (τ_0) being given as a rheological parameter, which has no physical interpretation. To account for this, the yield stress was given a lower bound of 0 Pa. Second, the consistency index has units of Pa-sⁿ, with the rate index varying from specimen to specimen. As a result, each consistency index is given in slightly different units, making direct comparison between results impossible. Due to these drawbacks, only rate index is discussed in this study.

4.1.3 Rheological Testing Results

Rate index results for each silica fume tested are shown in Figure 4.3. In all cases, increasing the amount of silica fume decreased the rate index; similarly, an increase in w/b also resulted in increased rate indices. For the case of 30% SF2 with a w/b of 0.20, the paste exhibited shear thinning behavior with a rate index of 0.96, with all other tested combinations exhibiting shear thickening behavior. Previous research has shown that shear thickening behavior can be readily observed in cement pastes containing higher dosages of HRWRA, with increased dosages of silica fume leading to a reduction in the shear thickening effect [73].

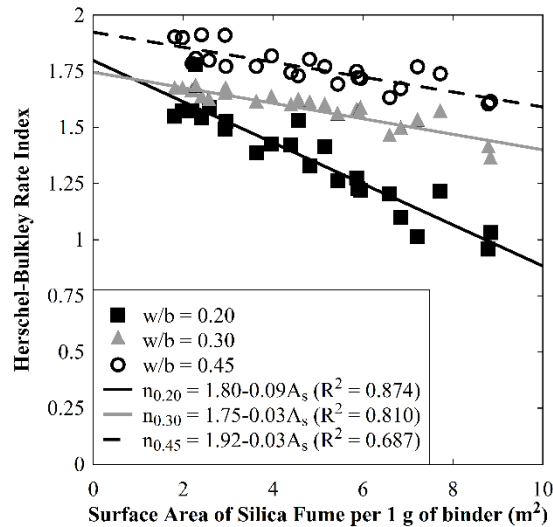


Figure 4.3. Rate index results

The ANOVA table for rate index is shown in Table 4.1. Using a confidence level of 95%, all three treatment factors, the interaction between fume type and w/b, and the interaction between fume amount and w/b were statistically significant as the calculated P-value is less than 0.05.

Table 4.1. ANOVA for rheological testing

Source	DF	SS	MS	F	P-value
A = Fume type	7	0.11	0.02	7.62	0.00
B = w/b	2	1.97	0.98	460.97	0.00
C = Fume amount	2	0.82	0.41	191.83	0.00
AB	14	0.09	0.01	3.09	0.01
AC	14	0.06	0.00	1.91	0.07
BC	4	0.22	0.06	26.09	0.00
Error	28	0.06	0.00	—	—
Total	71	3.33	—	—	—

These measurements were obtained with the cement pastes at very early ages (less than 10 minutes from combination of cement and water), and it is unlikely that chemical reactions were responsible for the observed behavior variations. Instead, it is likely the silica fumes' different physical characteristics that best explain the behavior. Average particle size, whether measured from laser diffraction or calculated from specific surface area and specific gravity, only represents a single silica fume characteristic and does not fully describe the distribution of particles as a whole. Additionally, data observations indicate there is not any strong dependency between the densification state and the measured rate indices.

Specific surface area measurements can be used to explain the observed rheological differences. As specific surface area increases, the measured rate index generally decreases, especially at low w/b. It is hypothesized that this response is caused by a decrease in the thickness of the lubricating layer of water between particles. For equivalent amounts of water, the lubricating layer of water around each particle becomes thinner as surface area increases. Due to the decrease in lubrication, the composite becomes much more difficult to mix. In mixtures with high w/b, these effects are minimized due to excess water, suggesting a critical lubrication layer thickness exists beyond which surface area no longer controls the rheological behavior. This is

further suggested by the coefficients of determination (R^2) shown in Figure 4.3, as the variance explained by surface area variations increases as the w/b decreases.

The hypothesis is supported by findings from Chen et al [46] who showed that this lubrication layer thickness could be used to describe increased flow behavior in high w/b (greater than 0.60) composites containing condensed silica particles.

4.2 Model Development

Multiple linear regression was used to develop an empirical model relating specific surface area, w/b, and silica fume percentage (P_{SF}) to rheological behavior (Equation 45). Initially, all three treatment factors and both significant first-order interactions determined from ANOVA were included in the regression model (Equation 46). Upon development of the multiple linear regression equation model, statistically insignificant components were removed from the equation (Table 4.2), leaving three significant factors in the regression model (Equation 47). The resulting regression equation was then plotted through the 72 raw data points (Figure 4.4), showing a very strong correlation ($R^2 = 0.88$). By using a regression equation relating measured and predicted indices, it can be shown that Equation 47 will tend to under-predict $n > 1.568$ and overpredict $n < 1.568$. The standard error between the predicted and measured rate indices was 0.072.

$$n = \beta_1 + \beta_2 SSA + \beta_3 \left(\frac{w}{b}\right) + \beta_4 P_{SF} + \beta_5 SSA \left(\frac{w}{b}\right) + \beta_6 SSA(P_{SF}) + \beta_7 \left(\frac{w}{b}\right) (P_{SF}) \quad (45)$$

$$n = \beta_1 + \beta_2 SSA + \beta_3 \left(\frac{w}{b}\right) + \beta_4 P_{SF} + \beta_5 SSA \left(\frac{w}{b}\right) + \beta_7 \left(\frac{w}{b}\right) (P_{SF}) \quad (46)$$

$$n = \beta_1 + \beta_2 SSA + \beta_4 P_{SF} + \beta_7 \left(\frac{w}{b}\right) (P_{SF}) \quad (47)$$

Table 4.2. Significance and regression coefficients for multilinear model

Coefficient	Equation 45	Equation 46	Equation 47
β_1	1.90	2.14	2.04
β_2	-0.010 (P = 0.00)	-0.020 (P = 0.01)	-0.0089 (P = 0.00)
β_3	-0.33 (P = .0.00)	-0.33 (P = 0.57)	---
β_4	-0.018 (P = 0.00)	-0.030 (P = 0.00)	-0.0369 (P = 0.00)
β_5	0.036 (P = 0.01)	0.036 (P = 0.11)	---
β_6	-0.00050 (P = 0.07)	---	---
β_7	0.052 (P = 0.00)	0.052 (P = 0.00)	0.0755 (P = 0.00)

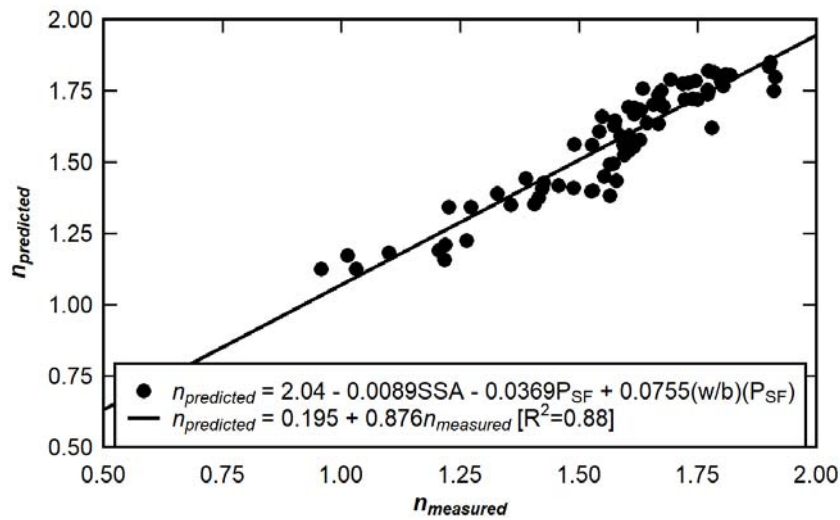


Figure 4.4. Multilinear rheological model fit

4.3 Model Validation

In order to validate the proposed empirical model, 10 trial cement-silica fume paste combinations were determined by random number generation, specimens were prepared, and requisite measurements were made to compare the measured response with model predictions. These trial combinations are shown in Table 4.3.

Table 4.3. Model validation mixtures with predicted rate indices

Trial	Silica Fume	w/b	P _{SF}	$n_{predicted}$
T1	SF5	0.24	10	1.62
T2	SF7	0.20	24	1.31
T3	SF2	0.34	11	1.66
T4	SF4	0.29	17	1.52
T5	SF2	0.25	17	1.47
T6	SF8	0.40	26	1.69
T7	SF1	0.44	14	1.83
T8	SF3	0.33	10	1.73
T9	SF7	0.29	27	1.43
T10	SF4	0.29	29	1.34

The measured rate indices of the 10 validation mixtures compared with the predicted values from Table 4.3 are shown in Figure 4.5. There appears to be a strong correlation ($R^2 > 0.9$) between the predicted and the measured indices using the Equation 47 model. The measured rate indices for nine of the 10 validation mixtures fell within 5% of the predicted value with the 10th predicted rate index only 5.2% less than measured.

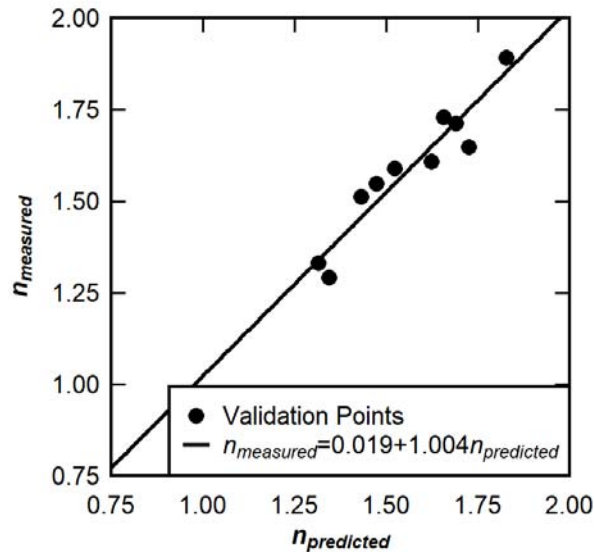


Figure 4.5. Multilinear model validation mixture results

4.4 Conclusions

Many conclusions can be drawn from this study. Firstly, changing silica fume source has a statistically significant effect ($P < 0.01$) on the rheological properties of oil well cement pastes. Secondly, the effect of changing silica fume sources becomes more pronounced at higher silica fume dosages. Silica fume dosage has a statistically significant effect ($P < 0.01$) on the rheological properties of oil well cement pastes. Thirdly, silica fume densification does not significantly affect the rheological properties of oil well cement pastes. Lastly, specific surface area can be used, along with mixture proportions such as w/b and silica fume dosage, to predict the rheological characteristics of oil well cement pastes through the use of a multilinear model.

5. WATER THICKNESS MODEL

Portions of the following section contain text and/or figures and tables previously submitted in **J.F. Burroughs**, C.A Weiss, Jr., J.E. Haddock, and W.J. Weiss, “Modeling early-age rheology of cement-silica fume pastes,” *ACI Materials Journal*, in review.

5.1 Introduction

A critical element in describing the rheological behavior of any collection of particles in a fluid is the amount of fluid in which particles can disperse. As the volume of fluid increases relative to the volume of solid particles, the system becomes increasingly more workable because the theoretical spacing between particles increases. As the volume of fluid decreases, the system has the tendency to become very stiff due to particle contact and frictional effects between the particles themselves. This is further illustrated by Figure 5.1.

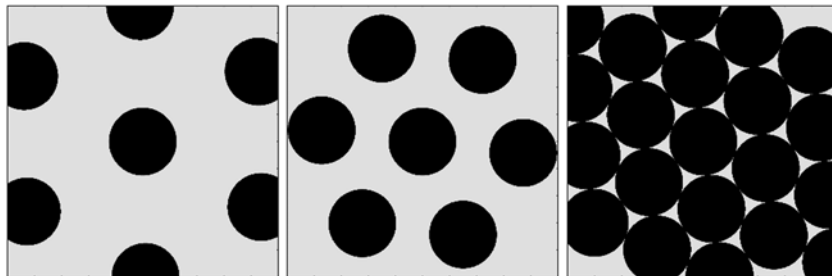


Figure 5.1. Particles (shown in black) surrounded by volumes of fluid (shown in gray) decreasing from left to right

In cementitious materials, the predominant fluid phase is, of course, water. In most cases, water is the only fluid phase added to the system, whether that water is from added mix water or another source. Some admixtures are used to increase the fluidity and workability of cementitious materials, but those chemicals are essentially a solid polymer phase dispersed in additional water. It is therefore paramount to consider all the avenues in which water can

interact with particles in a cementitious system if rheological behavior is to be adequately described.

5.2 Model Development

In the proposed analytical framework, water can be used in three different ways: 1) reaction, 2) absorption, and 3) coating. The classification of reaction considers any water that is consumed in a chemical reaction and the water becomes structurally bound in the products. In traditional cementitious materials, two main constituents can have reaction water, cement and slag.

Reaction water can be determined through non-evaporable water measurements, once hydration has been halted or completed. Reactions in which water simply serves as the medium for reaction rather than a reactant are not considered in reaction water. One such example is the pozzolanic reaction between silica fume and calcium hydroxide. These materials will not react in their dry state, but they become reactive once ions are dissolved in water.

Any water that is taken internally by any hydraulically inert particle is considered absorbed water. The classical example of this behavior is the amount of water required to bring aggregates to a SSD stage. Beyond the classic aggregate absorption, the potential absorptive nature of all other hydraulically inert particles must be considered as well. Absorbed water can be determined for aggregates using traditional ASTM techniques. For other hydraulically inert particles, approaches like those described in Chapter 2 must be used to accurately determine the absorptive behavior.

The third category includes all water that is not taken internally by a particle and can be determined algebraically. This interparticle water is used to lubricate the system by surrounding

each particle and reducing the frictional effects between particles. Considering these classifications from a volumetric standpoint, the total water in a cementitious material system can be described as shown in Equation 48.

$$V_{water,total} = V_{water,reaction} + V_{water,absorbed} + V_{water,coating} \quad (48)$$

Equation 48 can be expanded into Equation 49 by considering the water consumption of each particle in the system.

$$V_{water,total} = \sum_{i=1}^n V_{water,reaction,particle\ i} + \sum_{j=1}^m V_{water,absorbed,particle\ j} + V_{water,coating} \quad (49)$$

As previously noted, the model system used in this study included two solid constituents and two liquid constituents. As a hydraulically reactive particle, cement consumption is classified as reaction water, whereas any potential silica fume consumption is classified as absorbed water.

With these substitutions, Equation 49 can be resolved to Equation 50.

$$V_{water,mix} + V_{water,HRWRA} = V_{water,reaction,cem} + V_{water,absorbed,sf} + V_{water,coating} \quad (50)$$

Cement hydration is very much a diffusion-controlled process; as such, the water consumed by hydration reactions evolves over time. In the initial stages of hydration, very little water is actually consumed by these reactions because only the particle surfaces have been exposed to water. As such, the calculation of $V_{water,coating}$ to describe the early-age rheological behavior can be approximated by Equation 51, if $V_{water,reaction,cem}$ is assumed to be negligible.

$$V_{water,coating} \approx (V_{water,total} + V_{water,HRWRA}) - V_{water,absorbed,sf} \quad (51)$$

The parameter $V_{water,coating}$ allows for a descriptive measure of the workability of a cementitious material as materials with identical collections of particles will see increased workability as $V_{water,coating}$ increases; however, this parameter is influenced by the total volume of the material being mixed. Larger mixture volumes of equivalent mixture proportions

necessitates greater $V_{water,coating}$. In order to use a single parameter to describe the rheological behavior of any cementitious mixture, the parameter must be independent of batch size. To overcome this issue, a final parameter, t_{flow} , is proposed that idealizes $V_{water,coating}$ as the thickness of water that surrounds each individual particle in the system. This new parameter can be calculated using Equation 52 simply by dividing $V_{water,coating}$ by the total surface area of all the particles included. The resulting t_{flow} is highly idealized and assumes that each particle is perfectly dispersed and is coated by the same thickness of water. This coating thickness can be converted to the number of water molecules surrounding each particle by dividing t_{flow} by the diameter of a single water molecule (~0.28 nm).

$$t_{flow} \equiv \frac{V_{water,coating}}{A_{s,total}} \quad (52)$$

5.2.1 Comparison to Existing Models

The Water Thickness Model presented does share some similarities with the water film thickness described by Kwan et al. [54]; however, the Kwan model did not consider the contribution of silica fume and did not consider the potential for absorption by particles other than aggregates. Furthermore, Kwan et al. only considered water in excess of the volume of void space between particles in their calculations. Here, all water that is not absorbed is available for coating particles.

5.3 Comparison of Experimental and Analytical Results

The estimated coating thickness as determined by Equation 52 was compared with measured rate indices to determine the effectiveness of the proposed analytical model in describing the rheological behavior of cement pastes containing high volumes of silica fume. The relationships

between rate index and t_{flow} with and without the statistically approximated absorption capacities from Table 2.8 are shown in Figure 5.2. Table 5.1 shows goodness-of-fit results for the application of the analytical model for both cases.

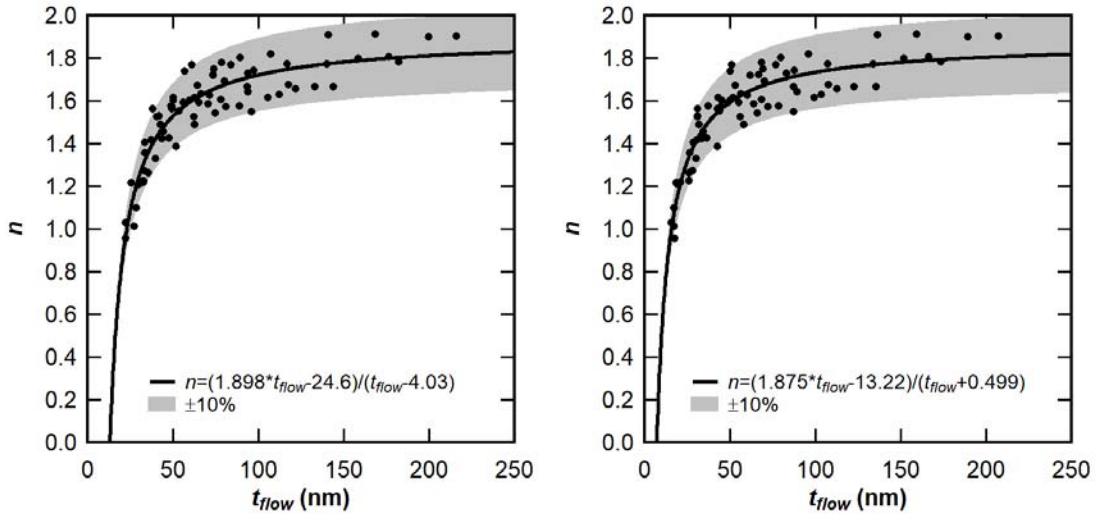


Figure 5.2. Relationship between rate index and coating thickness with (right) and without (left) absorption

Table 5.1. Goodness-of-fit with and without absorption

Absorption	$R^2_{y=x}$	RMSE	MAE
No	0.815	0.085	0.072
Yes	0.826	0.083	0.069

As is shown by the goodness-of-fit results in Table 5.1, only a slight improvement is seen when absorption is included regardless of the goodness-of-fit measurement. This is because the coating thickness calculation is dominated by the surface area of silica fume in the system rather than the absorptive nature of the silica fume particles in these combinations. In the 72 combinations considered, silica fume accounts for a minimum of 86.6% of the total particle surface area of each combination. With lower surface area additives, the effects of absorption may be more pronounced. The relative contributions of absorption and coating water are further

illustrated in Figure 5.3 for different mixture proportions involving SF1. These relative contributions should sum to 100% at early age, as reaction water is assumed negligible. More refined measurement, rather than estimation, of absorption capacity could also improve the full model results.

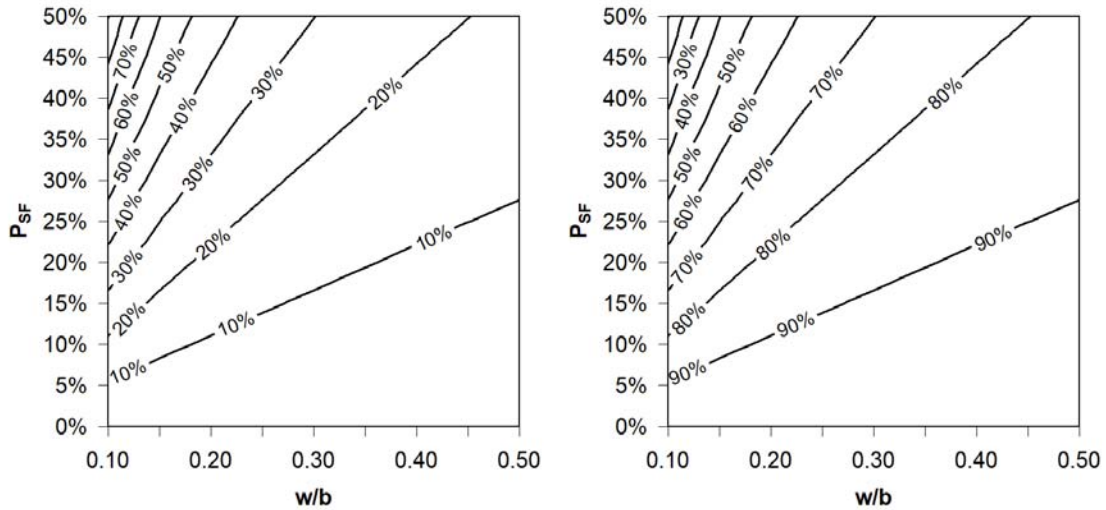


Figure 5.3. Volume fractions of water categorized at early age as absorption (left) and coating (right) for SF1

The main takeaway from the relationships shown in Figure 5.2 is that minor fluctuations in water content have a dramatic effect on the rheology of low water content mixtures, evidenced by the nearly vertical stem when $t_{flow} < 40$ nm. The effect of water fluctuations for higher water content mixtures is considerably reduced because the system already contains excess water that is more than necessary for mixing. This is shown by the asymptotic relationship in both cases, which begins to control the rheological behavior at t_{flow} between 50 and 100 nm. At these levels of t_{flow} , the water thickness is becoming equal to the radii of the silica fume particles, and particle interactions could reasonably be expected to be negligible. It can therefore be logically deduced that the effects of t_{flow} are much more critical for cementitious materials with very low

w/b like UHPC than for traditional concretes. This is further illustrated in Figure 5.4, which shows the critical dependence of the rheological behavior of combinations with a w/b of 0.20 and 30% silica fume replacement (shown as black squares in Figure 5.4) on t_{flow} . This dependence is less pronounced for combinations with a w/b of 0.45 and only 10% silica fume replacement (shown as white circles in Figure 5.4). In all cases for Figure 5.4, combinations with w/b of 0.20 are shown in black, w/b of 0.30 are shown in gray, and w/b of 0.45 are shown in white. Circles represent 10% silica fume, triangles represent 20% silica fume, and squares represent 30% silica fume.

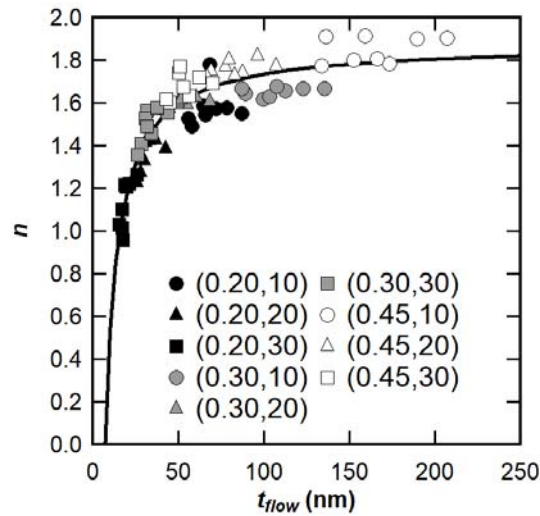


Figure 5.4. Rheological results segmented by w/b and silica fume content

The critical difference between the relationships developed that consider or do not consider absorption capacity, shown in Figure 5.2, is the tighter clustering of points along the regression line at low t_{flow} when absorption capacity is included in the analysis. Table 5.2 shows a comparison of goodness-of-fit measurements for t_{flow} both greater than and less than 40 nm for both absorption cases. As shown, there is very little difference in the goodness of fit measurements when the coating thickness exceeds 40 nm; however, there is more error in the

prediction at low t_{flow} when absorption capacity is not included in the analysis. This suggests that the absorption capacity of silica fume is more important when mixtures become more water starved. When available water is intentionally limited, any reduction of this available water due to absorption can have a significant effect on the rheological behavior.

Table 5.2. Comparison of goodness-of-fit at low and high coating thickness

Absorption	Range	RMSE	MAE
No	< 40 nm	0.090	0.079
Yes	< 40 nm	0.076	0.064
No	\geq 40 nm	0.084	0.070
Yes	\geq 40 nm	0.086	0.071

5.4 Conclusions

The rheological behavior of cementitious pastes containing silica fume at levels of up to 30% by total binder mass can be modeled analytically using a single parameter, t_{flow} . This parameter is idealized as the amount of water that surrounds each individual particle in the system; however, this parameter is reduced by any water consumed in chemical reactions and any water absorbed by the particles. A strong relationship is observed between t_{flow} and the Herschel-Bulkley rate index, which describes the fundamental rheological behavior of a material. By estimating the absorption capacity of silica fumes, the relationship between t_{flow} and rate index can be slightly improved, especially at low w/b and high replacements of silica fume.

6. CONCLUSIONS

6.1 Project Summary

This study analyzed the raw material properties of eight different silica fumes. Silica fumes were characterized for both chemical and physical properties to determine where differences existed among the sources. Included in the analysis were two silica fumes marketed as the same product yet produced in separate industrial facilities, as well as two silica fumes marketed as the same product produced from the same industrial facility at different times. From characterization testing, the most critical differences observed related to specific surface area and particle fineness.

It was hypothesized that silica fume particles could be potentially absorptive, which could influence the rheological performance of these materials. Because no standard test methods exist for analyzing the absorption capacity of silica fume, four approaches were proposed, all of which demonstrated that silica fume particles were in fact absorptive. Dynamic vapor sorption and statistical approximation were seen as the most promising of the test methods proposed. As statistical approximation is an estimation technique, dynamic vapor sorption is the recommended technique for any future testing.

Isothermal calorimetry testing was used to show that each silica fume reacted differently when exposed to a high pH environment saturated with $\text{Ca}(\text{OH})_2$. Undensified silica fumes were shown to release more heat over the life of the reaction than densified silica fumes on average. The extended Powers-Brownyard model to include silica fume was used to estimate the final degree of hydration and volume of hydration products produced for different mixture

proportions. Degree of hydration calculations were then used to calculate the reduction of surface area of reactive components in water-starved environments. By combining the volume of paste produced with the adjusted surface areas of inert and unreacted particles, a model was presented relating the thickness of paste surrounding each particle with compressive strength. A strong correlation was seen between these two parameters, as shown in Figure 3.10.

The influence of silica fume on the rheological behavior of cement pastes was analyzed by testing 72 combinations of silica fume, cement, and water. Two different models were presented, a multilinear model fit to the data and an analytical model theoretically derived to estimate the thickness of water surrounding each particle at early age. The Water Thickness Model was used to show that minor changes in water content could have a significant effect on the workability of pastes with low water contents or high silica fume contents. Less significant effects were seen as the initial water content increased.

6.2 Recommended Future Work

Future work in this area needs to focus on refining the inputs of the Paste Thickness Model for each of the different silica fumes. As currently presented, all silica fumes are considered the same in the model, even though testing showed that each silica fume reacted differently. While assuming equivalent reactivity in the model showed strong agreement with compressive testing results, refinement of the inputs should improve the predictions of this model. Determining the applicability of these analytical models for the analysis of more traditional concretes also seems like the next logical step. Expanding the use of these approaches for other additives to concrete such as fly ash or ground granulated blast furnace slag seems like a natural progression in research as well.

APPENDIX A. PRELIMINARY STUDY

First International Interactive Symposium on UHPC – 2016
Analyzing Effects of Varied Silica Fume Sources within Baseline UHPC

Analyzing Effects of Varied Silica Fume Sources within Baseline UHPC

Author(s) & Affiliation:

Jedediah F. Burroughs, U.S. Army Engineer Research and Development Center, Vicksburg, MS
Todd S. Rushing, U.S. Army Engineer Research and Development Center, Vicksburg, MS
Dylan A. Scott, U.S. Army Engineer Research and Development Center, Vicksburg, MS
Brett A. Williams, U.S. Army Engineer Research and Development Center, Vicksburg, MS

Abstract:

Silica fume has been used for many years as a fine-grained supplementary cementitious material in ultra-high performance concrete (UHPC) to aid in improving strength and durability. Since silica fume is a waste product, much variability is present among different silica fume sources. This study compared the functionality of eight silica fume products in an otherwise identical cementitious matrix using a standard reference UHPC known as Cor-Tuf Baseline (CTB). The studied silica fumes were obtained from multiple suppliers and geographical locations. Both densified and undensified silica fumes were evaluated. Silica fumes were substituted one for another on a 1:1 basis (by mass) for initial batching. Fresh properties of interest in this study included mixing time and flow percentage. Hardened properties of interest included compressive strength and density. The effects of different mixing actions were studied as well as different high temperature curing conditions. Results of this study indicated that some silica fumes, while similar in composition to others tested, presented many difficulties in producing a UHPC. The state of silica fume densification did not exclusively determine its usefulness in the production of a UHPC. Increased shearing action during mixing was seen as advantageous for increased fluidity and ease of production. The use of a steam generator for high temperature curing was more beneficial in strength development than placing the samples in a high temperature water bath at the same temperature. Two of the eight silica fumes tested were found to be acceptable for CTB production.

Keywords: compressive strength, densification, fresh properties, silica fume, UHPC

Burroughs, Rushing, Scott, and Williams 1

1. Introduction

Silica fume is a highly reactive pozzolan due to a high amorphous silicon dioxide (SiO_2) content and an extremely small particle size. Portland cement mixtures when mixed with water form two primary chemical compounds, calcium silicate hydrate (CSH) and calcium hydroxide (CH). Silica fume adds strength to a portland cement mixture by reacting with CH to form additional CSH, which is the primary strength giving phase in portland cement concrete. The very fine particle size of silica fume also improves particle packing in cementitious mixtures leading to decreased interfacial transition zone porosity and increased overall strength gain, durability, and decreased permeability. Due to these properties, silica fume is a common addition to most ultra-high performance concrete (UHPC) mixtures.

Ultra-high performance concrete is a family of materials that typically exhibits high compressive strengths in excess of 150 MPa and high durability due to negligible interconnected porosity. UHPC formulations generally consist of a high cementitious content incorporating oil-well or low-heat portland cement, siliceous fine aggregates, crushed quartz or other micron-sized powder, silica fume, water, high-range water-reducing admixtures (HRWRA) to control rheology, and other components that vary by manufacturer. The high compressive strengths of UHPC lead to brittle behavior similar to ceramics. To overcome this brittle behavior, steel fiber reinforcement is commonly used. The addition of steel fiber reinforcement aids in delocalizing micro- and macro-scale cracking, and leads to improvements in tensile properties and minimized spallation during failure (Scott et al. 2015).

Many UHPC formulations exist, including those commercially available from vendors as well as in-house mixtures. Cor-Tuf Baseline (CTB) is one such UHPC formulation developed by the U.S. Army Engineer Research and Development Center (ERDC) as an in-house laboratory standard reference material with minimal batch-to-batch variation. The general mixture proportion for CTB is described in United States Patent 7,744,690 B2 (Durst et al. 2010), and the development process is described in a 2008 Northwestern University PhD dissertation (O'Neil 2008). CTB has a compressive strength that can range from 193 to 220 MPa on average (Scott et al 2015). The present study analyzed the effects of substituting one silica fume source for another by mass in a standard reference mixture proportion.

2. Materials

American Petroleum Institute (API) class H oil well cement was used as the primary cementitious component in this study. Class H oil well cement was used instead of a more traditional Type I/II Portland cement due to its coarser grinding, typically higher dicalcium silicate (C_2S) content, and lack of tricalcium aluminate (C_3A), which allowed for slower hydration. Two inert constituents were used as fine aggregates in this study. Unground silica was used as the primary fine aggregate in all mixture proportions, and angular ground quartz silica was also used as a fine aggregate for this study. The only admixture used in this study was a high-range water-reducing admixture (HRWRA) to improve the workability of the low water-to-cement ratio mixture. The product used was a polycarboxylate HRWRA. This HRWRA provides a lubricating effect that allows for stiffer mixtures to be more readily placed into molds and forms without dramatically altering the water-to-cement ratio of the mixture. One negative side effect of using a high dosage rate of HR WRA is a retarding effect on the setting time of the

material. Steel fibers were used as tensile reinforcement in the composite matrix. 1.2-inch (30-mm) fibers with hooked ends and an aspect ratio (L/d) of 55 were used.

Silica fume is used as the primary supplementary cementitious material (SCM) in Cor-Tuf Baseline (CTB). Eight distinct silica fume products were considered in this study. The traditional silica fume used in CTB, SF-1, was used as a reference material in this study. SF-1 was not a traditional silica fume according to ASTM C1240 (ASTM 2015a) as it was produced as a by-product in a zirconium furnace rather than as a by-product of a ferro-silicon alloys furnace. This gave SF-1 a high silica purity and unique properties that were advantageous to UHPC mixtures. Seven additional silica fume materials were also considered. They were labeled SF-2 through SF-8. Both densified and undensified silica fumes were considered. SF-1 was an undensified silica fume, but both types of fume were studied for completeness. SF-3 and SF-7 were the densified fumes studied. All other fumes were undensified.

3. Silica Fume Characterization

Each silica fume source was characterized in its powder state in two ways: (1) particle size distribution was determined through the use of laser diffraction analysis, and (2) bulk chemical analysis was determined through the use of x-ray fluorescence (XRF) spectroscopy.

3.1. Methods and Procedures

Laser diffraction was used to determine particle size distributions by measuring the angular variation in intensity of light scattered as a laser beam passed through a dispersed particulate sample. A narrow beam of monochromatic light from a He-Ne laser, $\lambda = 633$ nm, is passed through the dispersed sample, and the angular distribution of the diffracted light is measured. The angle of the diffracted light increases as particle size decreases. This technique is used to determine particle sizes in nanometer to micrometer range (McCave et al. 1986).

Laser diffraction was performed using a Beckman Coulter LS laser diffraction particle size analysis system. Sample preparation was performed by sonication using a 600W ultrasonic probe for 15 minutes in deionized water. The sonication time was selected after a small study of the effect of sonication time on dispersion that indicated 15 minutes was sufficient to fully disperse the silica fume in deionized water. Following sonication, the dispersed silica fume and deionized water solution were passed into the laser diffraction system using a peristaltic pump. Two consecutive laser diffraction measurements with a length of 60 seconds each were performed. Following the laser diffraction measurements, integrated analysis algorithms were used to generate particle size distributions and associated statistics.

X-ray fluorescence (XRF) spectroscopy is a non-destructive chemical analysis technique utilized to measure the bulk chemical composition of samples. During the analysis, an x-ray beam (source) hits a sample and its atoms interact with the received radiation. The energy causes an electron that is positioned in an inner shell in the atom to be dislodged, making the atom unstable and creating a vacancy. At this point, an electron that is positioned in another orbit inside an outer shell moves to the vacancy in order to make the atom stable, and in the process emits an x-ray at a unique energy value (in keV). This energy is known as the binding energy, which is characteristic of that specific element. The process of emissions of characteristic x-rays is called x-ray fluorescence (XRF). When the source energy changes, the same process described above occurs. During this process the different characteristic x-rays with their corresponding energy values are

emitted producing a spectra.

3.2. Characterization Data

Figure 1 shows the particle size distributions for the all silica fume products tested. The solid blue line represents the reference silica fume, SF-1. These test results show that SF-2, SF-4, SF-6, and SF-7 are finer than the reference material, whereas SF-3, SF-5, and SF-8 are coarser. SF-6 and SF-7 are produced at the same location, so their similar particle size distributions were expected.

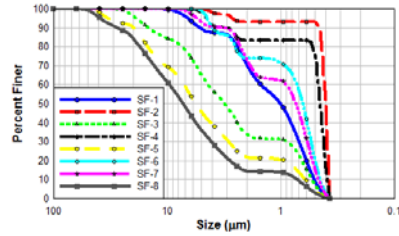


Figure 1. Particle Size Distributions for Silica Fumes.

Table 1 summarizes the chemical testing results for the nine different silica fumes considered. The four oxide contents represent the components that make up the majority of the silica fume. The “Balance” column is the remaining percentage of the chemical composition that does not fall into one of the main four oxide categories. Loss on ignition, or LOI, is the percentage of mass loss when the silica fume is heated to high temperature. LOI gives an indication of the amount of carbon present in a silica fume.

Table 1. Chemical composition of silica fumes.

Silica Fume	SiO ₂	CaO	MgO	Na ₂ O	Balance	LOI
SF-1	97.30	0.00	0.06	0.00	2.64	1.35
SF-2	95.04	0.01	0.38	1.78	2.79	1.39
SF-3	93.26	0.00	0.21	1.24	5.29	3.93
SF-4	74.95	17.90	2.89	0.52	3.74	0.89
SF-5	97.21	0.00	0.15	0.16	2.48	1.61
SF-6	96.06	0.00	0.14	0.12	2.68	2.73
SF-7	93.65	0.10	0.37	0.23	5.65	4.47
SF-8	97.42	1.27	0.09	0.01	1.21	0.93

With the exception of the SF-4 fume, Table 1 shows that silicon dioxide makes up at least 93% of all silica fumes tested. The SF-4 fume was only 75% silicon dioxide and had a much higher percentage of calcium oxide than the other fumes.

4. UHPC Evaluation

4.1. Methods and Procedures

4.1.1. Mixture Proportioning

The standard baseline reference mass mixture proportion for CTB (MP-1) used in this study is given in Table 2 below. Each of the eight studied silica fumes was incorporated into the CTB mixture proportion using the mixing methods and curing processes described in Section 4.1.2 and Section 4.1.4.

Table 2. Mixture proportions.

Material	MP-1 – pcy (kg/m ³)	MP-2 – pcy (kg/m ³)	MP-3 – pcy (kg/m ³)
Cement	1350 (804)	1400 (829)	1360 (805)
Unground Silica	1310 (778)	1350 (802)	1310 (779)
Ground Silica	375 (223)	387 (230)	376 (223)
Silica Fume	527 (313)	408 (242)	528 (313)
HRWRA	23.2 (13.7)	23.9 (14.2)	23.2 (13.8)
Water	282 (167)	291 (173)	274 (163)
Steel Fibers	420 (249)	433 (257)	421 (250)

4.1.2. Mixing Procedures

Three different mixers that had different mixing actions were used in this study. Bench-scale planetary style mixing was completed using a 12-qt (11.3-L) Hobart Legacy® Countertop mixer fitted with a flat beater and bowl-scraper attachment. This mixer was used for all preliminary batching and down selection of potential silica fume sources. Steel fibers were not included in bench-scale mixtures. The standard batch volume for bench-scale mixing was 0.075 ft³ (0.002 m³). This volume represented the final wet out volume of concrete. The dry powders used took up considerably more volume prior the addition of water, so batch size was limited by the amount of dry powder that could be successfully mixed in the mixer.

All bench-scale mixing was performed with an attachment speed of 33 RPM. For control, all bench-scale mixing was performed in a constant temperature room set at 65°F (18°C). All dry materials were added at one time and dry blended for five minutes. All liquids were then added and mixed until the mixture “broke over”. “Break over” is defined in Section 4.1.3. After each mixture broke over, five additional minutes of mixing was conducted to ensure thorough mixing. ASTM standard 2-in (50-mm) cubes were cast for compressive strength testing using the materials mixed with the bench-scale mixer.

High shear mixing was used as a robust mixing technique for larger scale batching. High shear mixing was performed using an Eirich high shear mixer. The standard batch size used was 2.0 ft³ (0.056 m³). Steel fibers were included in each batch, and 4 in. x 8 in. (100 mm x 200 mm) cylinders and 4 in. x 4 in. x 15 in. (100 mm x 100 mm x 375 mm) beams were cast for compressive strength and flexural strength testing, respectively. Traditional rotating drum mixing was performed as a worst-case-scenario mixing technique. Batches that are successfully mixed using this technique are assumed to be mixable in any concrete mixer. A Gilson rotating drum mixer was used in this

study. Steel fibers were included in these batches, and 4 in. x 8 in. (100 mm x 200 mm) cylinders were cast for compressive strength testing. The standard batch size was 1.5 ft³ (0.042 m³).

4.1.3. Fresh Properties

Mixing time was measured as the elapsed time from the addition of water until the batch “broke over”. Breaking over was defined as the time at which the material wet out enough to become a fluid. The time was measured using a stopwatch and recorded to the nearest quarter minute due to the subjective nature of determining break over. Mixing time was recorded for bench-scale batches only.

Workability was measured in accordance with ASTM C1437 (ASTM 2013b). This test method determined the flow of a material as a percentage of spread from an initial cone diameter. The flow cone is filled halfway with mortar and tamped 20 times prior to adding the remaining volume. The tamping process is repeated on the second layer, and the excess mortar is struck off the top of the mold with a straight edge. The flow cone is removed, and the flow table is dropped 25 times in 15 seconds. The resulting diameter of the mortar is measured with special calipers at four defined points. The sum of these four diameters represents the percentage increase in the diameter of the flow cone. Workability was only measured for bench-scale batches.

4.1.4. Curing Regimes

The standard curing method for cast samples was seven days at a room temperature (23°C), 100% humidity environment, followed by six days in a high temperature 195°F (90°C), 100% humidity environment. The room temperature curing was performed in the ERDC’s Moist Curing Room. High temperature curing was performed either by submerging the samples in a hot water bath or by using a steam generator to saturate the samples with steam underneath an insulated cover. All samples cast using the bench-scale planetary mixer were cured using the hot water bath. Samples from the high shear mixer were cured using the steam generator. Samples made using the traditional rotating drum mixer were cured using both high temperature apparatuses, and the technique used is noted in the results.

4.1.5. Hardened Properties

The density of each mixture was determined using hydrostatic weighing, which compares the mass of the sample “in air” to the mass of the sample submerged in water. This procedure was performed in accordance with ASTM C39 (ASTM 2015b).

The compressive strength, designated by f'_c , of each mixture proportion was measured in accordance with ASTM C39 (ASTM 2015b) for cylindrical samples and ASTM C109 (ASTM 2013a) for cubic samples. A Tinius Olsen Universal Testing Machine (UTM) capable of applying 440-kips (1,950 kN) of force was used to test cubic samples, and a 1,000-kip (4,450 kN) SATEC load frame was used to test cylindrical samples. Each load frame was connected to a data collection system that recorded load and displacement data. Data of interest for each sample was the peak load obtained. Compressive strength was calculated as the peak load divided by the cross-sectional area of the sample. All compressive strength tests were performed at 14 days, which was one day after the end of standard curing.

Flexural strength, designated by f_b , of fiber reinforced samples was measured in accordance with ASTM C78 (ASTM 2015c). The standard sample geometry was a 4 in. x 4 in. x 15 in. (100 mm x 100 mm x 375 mm) flex beam. The simply supported span length was 12 in. (300 mm), and the flexural load was applied at third points [4 in. and 8 in. (100 mm and 200 mm)]. Load versus position data were recorded with the peak load being the data of interest.

4.2.1. Bench-scale Planetary Mixing

The results for mixtures using bench-scale planetary mixing are shown in Table 3. Only three of the eight tested silica fumes successfully mixed and produced a UHPC similar to CTB, one of those being the reference silica fume. SF-2 was an undensified silica fume, and SF-7 was a densified product. All other tested silica fumes were allowed to mix for at least one hour without breaking over. Even after four times the allowed mixing time, these materials were unsuitable for the production of CTB. Both other silica fumes mixed much quicker than the reference and exhibited higher fluidity. The increased fluidity of SF-7 suggests that the densified silica fume was not breaking apart as expected, so the silica fume had less surface area for reaction. The density results were similar for all three silica fume sources, and SF-7 samples tested at a higher compressive strength than the other two materials.

Property/Batch	SF-1	SF-2	SF-7
Time – min	14:45	6:15	9:15
Flow – %	57.6	60.6	82.1
ρ – lb/ft ³ (kg/m ³)	148.1 (2372)	145.9 (2337)	149.2 (2390)
f'_c – ksi (MPa)	27.0 (186)	26.8 (185)	29.7 (205)

4.2.2. High-shear Mixing

The results for mixtures using high-shear mixing are shown in Table 4. Here, only the two non-reference silica fumes that were successful in producing CTB using bench-scale planetary mixing were tested. One key difference in these samples was the presence of steel fiber reinforcement. Once again, the two mixtures had similar densities, and SF-7 samples tested with a slightly higher compressive strength. For both materials, the measured flexural strength was approximately 14% of the measured compressive strength. The results here are very similar for both silica fume sources, which suggests that both densified and undensified silica fumes perform similarly with appropriate mixing techniques and adequate batch sizes.

Property/Batch	SF-2	SF-7
ρ – lb/ft ³ (kg/m ³)	158.1 (2533)	159.9 (2561)
f'_c – ksi (MPa)	28.0 (193)	28.9 (199)
f_b – ksi (MPa)	3.98 (27.4)	4.18 (28.8)

4.2.3. Traditional Rotating Drum Mixing

The results for mixtures made using traditional rotating drum mixing are shown in Table 5. Traditional rotating drum mixing is a much less energy intensive mixing process, so the mixtures had more difficulties in mixing. In order to ease some of these difficulties, the mixture proportions for these batches were changed slightly. Preliminary workability testing of drum-mixed SF-2 CTB showed decreased fluidity when compared with traditional CTB. To counter this, 25% of the original silica fume content was removed, which allowed for easier mixing and similar fresh properties. This mixture proportion is shown in Table 2 as MP-2. Drum-mixed SF-7 CTB actually exhibited excess fluidity when compared to reference materials. To balance this, 3% of the mix water was withheld from the batch. This mixture proportion is shown in Table 2 as MP-3. The labels A and B in Table 5 for SF-7 indicate different methods of high temperature curing. SF-7A samples were cured by submerging samples in a hot water bath set to 195°F (90°C). SF-7B samples were cured under a steam blanket using a steam generator set to the sample temperature. The samples for SF-7A and SF-7B were cast out of the same batch of fresh CTB, with only the different high temperature curing applied. As with high-shear mixing, the samples tested were fiber reinforced. Similar densities were observed for both silica fume sources, but the removal of 25% of silica fume for SF-2 caused a significant reduction in compressive strength. The decrease in silica fume also caused a small reduction in density when compared to SF-7 samples. The reduction in strength was to be expected because less silica fume was available to fill small voids in the matrix and for secondary pozzolanic reaction. For the SF-7 samples, the steam generator samples were marginally stronger than the hot water bath samples. While only a small increase, these results suggest that the use of a steam generator is more effective than the use of a hot water bath. Certainly, the use of a steam generator is more practical as sample size increases.

Property/Batch	SF-2	SF-7A	SF-7B
ρ – lb/ft ³ (kg/m ³)	160.6 (2573)	162.4 (2601)	162.4 (2601)
f'_c – ksi (MPa)	23.6 (163)	26.4 (182)	27.3 (188)

The present study used three different mixing techniques to study eight distinct silica fume sources. The findings of this study suggest the following conclusions:

- When used in small batches, the agglomerations in densified silica fumes may not adequately break apart. This can lead to higher than expected fluidity and segregation of fibers.
- When using larger batches and high intensity mixing, there was no significant differences in hardened properties observed between UHPC made with densified or undensified silica fumes. However, with low intensity mixing such as a traditional rotating drum, the agglomerations in densified silica fumes may still not adequately disperse. The resulting increased fluidity led to different adjustments to the baseline mixture proportion than with undensified silica fume.
- The use of a steam generator and steam blanket for high temperature curing of UHPC was more effective than the use of a hot water bath set at the same temperature.
- Results suggest that silica fumes with an apparent $d_{50} \leq 1 \mu\text{m}$ are best suited for the production of suitable UHPC. Selection of silica fume should be based on performance in matrix.

6. References

Durst, B. P., et al. Blast-resistant concrete also suitable for limiting penetration of ballistic fragments. United States of America: Patent 7,744,690. 29 June 2010.

McCave, I. N., et al. "Evaluation of a laser-diffraction-size analyzer for use with natural sediments." *Journal of Sedimentary Petrology* (1986): 561-564.

O'Neil, E.F. *On engineering the microstructure of high-performance concretes to improve strength, rheology, toughness, and frangibility*. PhD dissertation. Evanston, IL: Northwestern University, 2008.

Scott, D. A., et al. *Impact of steel fiber size and shape on the mechanical properties of ultra-high performance concrete*. ERDC/GSL-TR-15-22. Vicksburg, MS: U.S. Army Engineer Research and Development Center, 2015.

Standard specification for silica fume used in cementitious mixtures, ASTM C1240, ASTM International, West Conshohocken, PA, 2015a.

Standard test method for compressive strength of cylindrical concrete specimens, ASTM C39/C39M, ASTM International, West Conshohocken, PA, 2015b.

Standard test method for compressive strength of hydraulic cement mortars (using 2-in or [50-mm] cube specimens), ASTM C109/C109M, ASTM International, West Conshohocken, PA, 2013a.

Standard test method for flexural strength of concrete (using simple beam with third-point loading), ASTM C78/C78M, ASTM International, West Conshohocken, PA, 2015c.

Standard test method for flow of hydraulic cement mortar, ASTM C1437, ASTM International, West Conshohocken, PA, 2013b.

7. Acknowledgements (optional)

The authors would like to acknowledge Mr. Brian Green (U.S. Army ERDC) for additional technical oversight of this study, as well Ms. Wendy Long and Mr. Kirk Walker (both U.S. Army ERDC) for their assistance in the mixing of batches and casting of samples. Permission to publish is granted by the Director, Geotechnical and Structures Laboratory.

APPENDIX B. QUANTITATIVE XRD WHOLE PATTERN FITS

This appendix includes quantitative whole pattern fits for each of the silica fumes tested. The material tested is listed in the top left corner of each figure under the heading Scan Name. File names including -A, -B, etc. indicate multiple replicates of the same material.

Scan ID: SF1-A.xrdml

Scan Parameters: 2.511°/69.99°/0.01671°/219.71(s), $\phi=0.0^\circ$, $I(p)=3459.0/592.0$, Co(45kV,40mA), Thursday, November 10, 2016, 5

- Zero Offset = -0.0531 (0.0158) Displacement = 0.0 Distance Slack = 0.0
- Ka2 Peaks Present Ka2/Ka1 Ratio = 0.5 X-Ray Polarization = 1.0

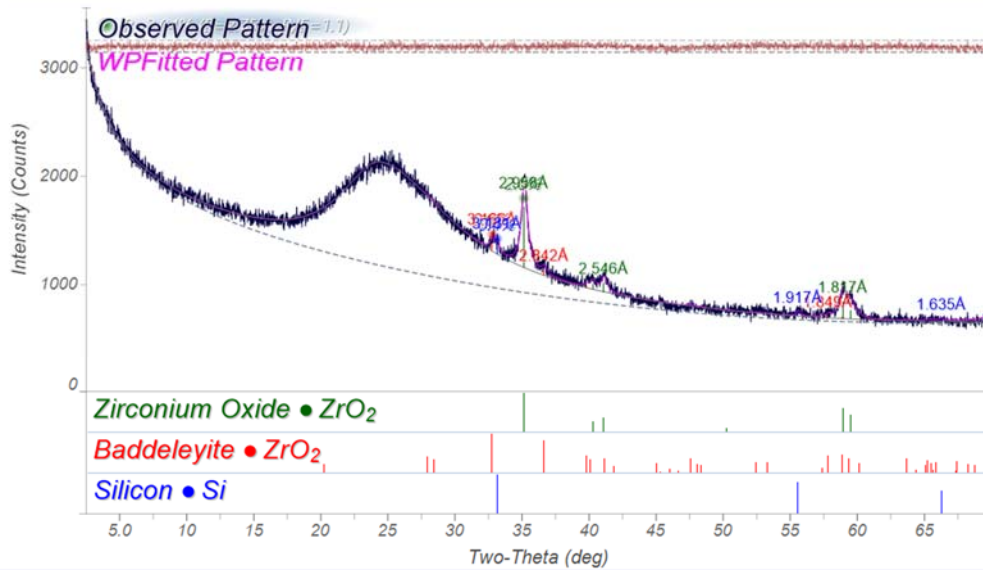
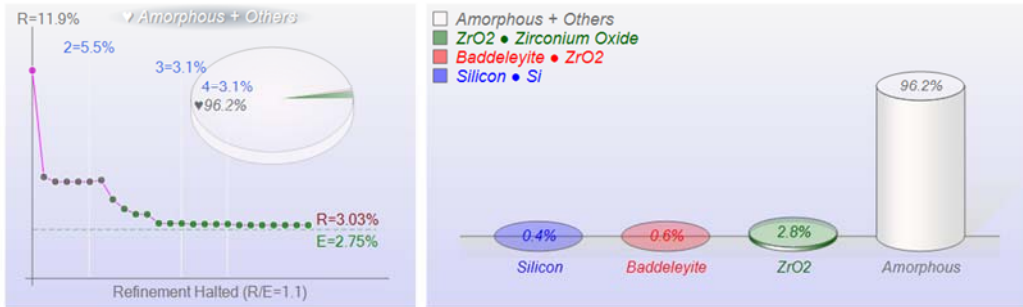
Geometry: Diffractometer Lp Fitted-Range: 2.5° - 70.0° BG-Model: Polynomial (2) λ : 1.78899 Å (Co)

PSF: pseudo-Voigt Broadening: Individual FWHM Curve Instrument: Constant FWHM = 0.1°

Phase ID (3)	Chemical Formula	PDF-#	Wt%	RIR	μ
Zirconium Oxide	ZrO ₂	04-005-4207	2.8	10.62	1000.2
Baddeleyite	ZrO ₂	04-004-4339	0.6	5.01	955.8
Silicon	Si	04-012-7888	0.4	4.91	218.2
Amorphous + Others	SiO ₂		96.2	2.50	

XRF(Wt%): ZrO₂=3.5%, SiO₂=97.0%

Refinement Halted (R/E=1.1), ♦ Round=4, Iter=6, P=23, R=3.04% (E=2.75%, EPS=0.5)



X:\XRD Data\Uedadiah\Series 1\SF1-A.xrdml

Friday, September 06, 2019, 1:14 PM • US Army Corp Engineers

Scan ID: SF1-B.xrdml

Scan Parameters: 2.511°/69.99°/0.01671°/219.71(s), φ=0.0°, I(p)=3380.0/548.0, Co(45kV,40mA), Thursday, November 10, 2016, 7

- Zero Offset = -0.0186 (0.0144) Displacement = 0.0 Distance Slack = 0.0
- Ka2 Peaks Present Ka2/Ka1 Ratio = 0.5 X-Ray Polarization = 1.0

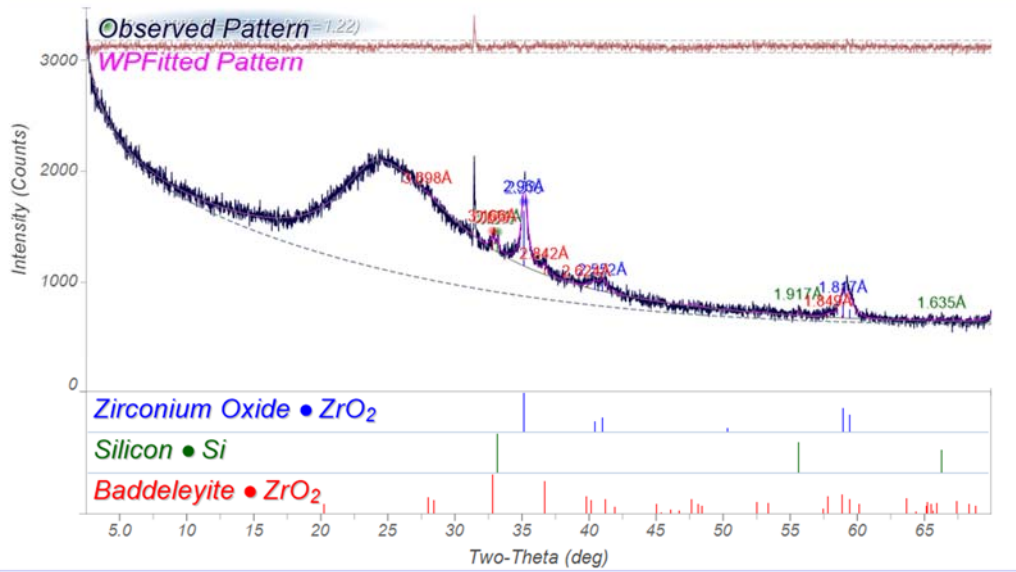
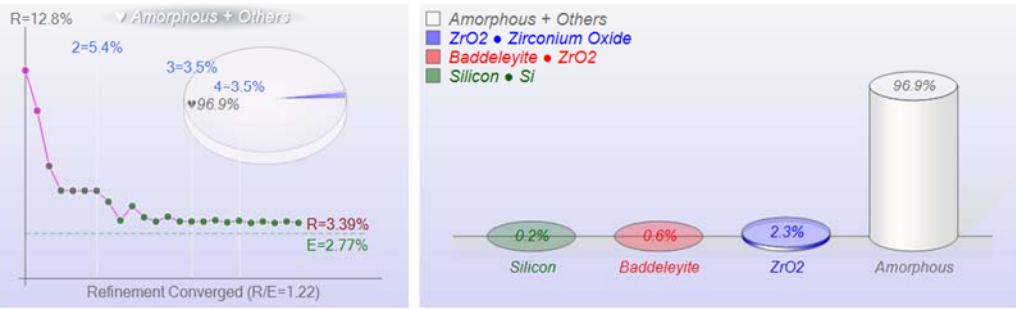
Geometry: Diffractometer Lp Fitted-Range: 2.5° - 70.0° BG-Model: Polynomial (3) λ: 1.78899 Å (Co)

PSF: pseudo-Voigt Broadening: Individual FWHM Curve Instrument: Constant FWHM = 0.1°

Phase ID (3)	Chemical Formula	PDF-#	Wt%	RIR	μ
Zirconium Oxide	ZrO ₂	04-005-4207	2.3	10.62	998.1
Silicon	Si	04-012-7888	0.2	4.91	218.2
Baddeleyite	ZrO ₂	04-004-4339	0.6	5.01	955.8
Amorphous + Others	SiO ₂		96.9	2.50	

XRF(Wt%): ZrO2=2.9%, SiO2=97.3%

Refinement Converged (R/E=1.22), Round=4, Iter=4, P=24, R=3.38% (E=2.77%, EPS=0.5)



X:\XRD Data\Uedadiah\Series 1\SF1-B.xrdml

Friday, September 06, 2019, 1:24 PM • US Army Corp Engineers

Scan ID: SF1-C.xrdml

Scan Parameters: 2.511°/69.99°/0.01671°/219.71(s), $\phi=0.0^\circ$, $I(p)=3749.0/490.0$, Co(45kV,40mA), Thursday, November 10, 2016, 9

- Zero Offset = -0.0555 (0.0122) Displacement = 0.0 Distance Slack = 0.0
- Ka2 Peaks Present Ka2/Ka1 Ratio = 0.5 X-Ray Polarization = 1.0

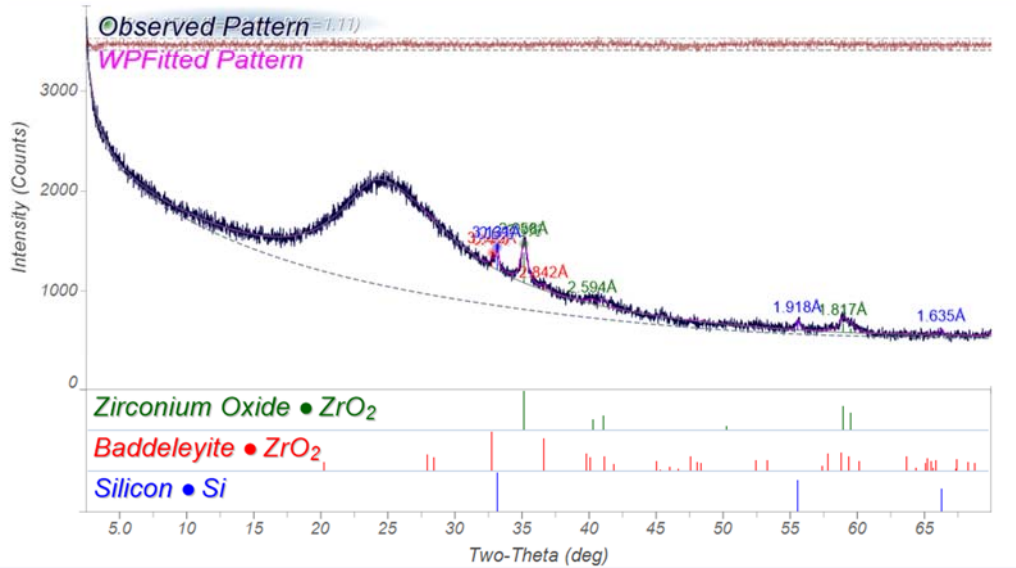
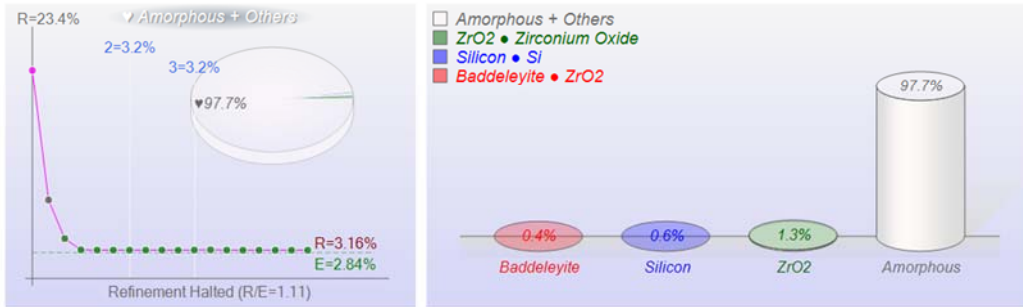
Geometry: Diffractometer Lp Fitted-Range: 2.5° - 70.0° BG-Model: Polynomial (5) λ : 1.78899 Å (Co)

PSF: pseudo-Voigt Broadening: Individual FWHM Curve Instrument: Constant FWHM = 0.1°

Phase ID (3)	Chemical Formula	PDF-#	Wt%	RIR	μ
Zirconium Oxide	ZrO ₂	04-005-4207	1.3	10.62	1000.2
Baddeleyite	ZrO ₂	04-004-4339	0.4	5.01	955.8
Silicon	Si	04-012-7888	0.6	4.91	218.1
Amorphous + Others	SiO ₂		97.7	2.50	

XRF(Wt%): ZrO₂=1.7%, SiO₂=98.9%

Refinement Halted (R/E=1.11), ♦ Round=3, Iter=6, P=25, R=3.15% (E=2.84%, EPS=0.5)



X:\XRD Data\Uedadiah\Series 1\SF1-C.xrdml

Friday, September 06, 2019, 1:15 PM • US Army Corp Engineers

Scan ID: SF2-A.xrdml

Scan Parameters: 2.511°/69.99°/0.01671°/219.71(s), $\phi=0.0^\circ$, $I(p)=3366.0/282.0$, Co(45kV,40mA), Thursday, November 10, 2016, 1

- Zero Offset = 0.0372 (0.0249) Displacement = 0.0 Distance Slack = 0.0
- Ka2 Peaks Present Ka2/Ka1 Ratio = 0.5 X-Ray Polarization = 1.0

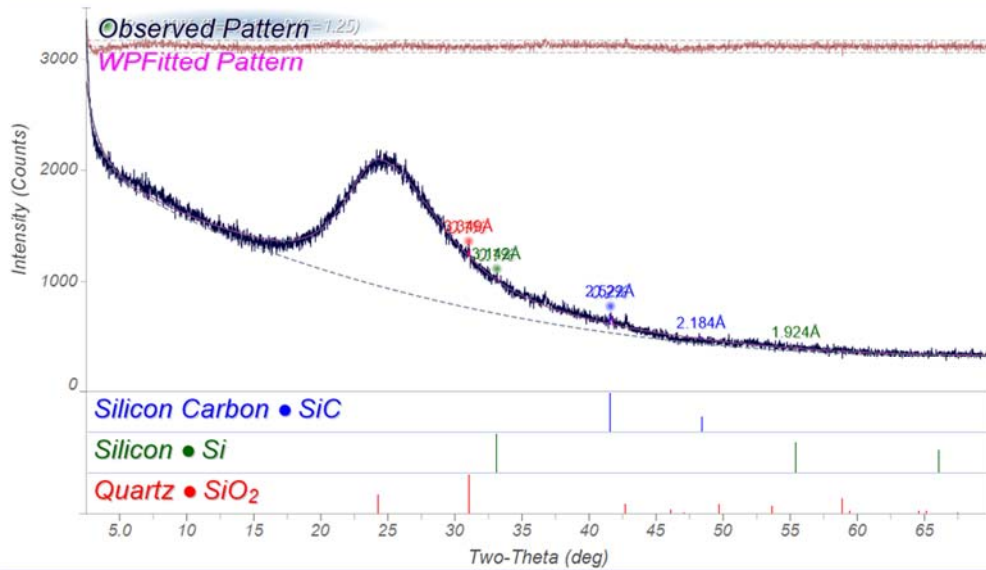
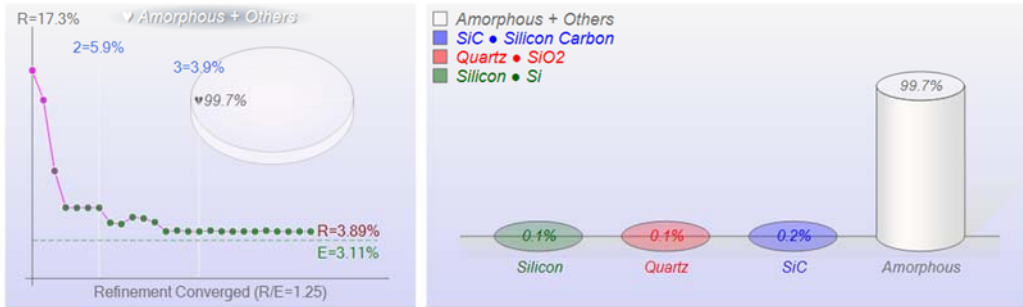
Geometry: Diffractometer Lp Fitted-Range: 2.5° - 70.0° BG-Model: Polynomial (3) λ : 1.78899 Å (Co)

PSF: pseudo-Voigt Broadening: Individual FWHM Curve Instrument: Constant FWHM = 0.1°

Phase ID (3)	Chemical Formula	PDF-#	Wt%	RIR	μ
Silicon Carbon	SiC	04-002-9070	0.2	3.79	215.6
Silicon	Si	04-012-7888	0.1	4.91	215.9
Quartz	SiO ₂	01-089-1961	0.1	4.06	139.9
Amorphous + Others	SiO ₂		99.7	2.50	

XRF(Wt%): SiO₂=100.2%, CO₂=0.2%

Refinement Converged (R/E=1.25), \blacklozenge Round=3, Iter=4, P=21, R=3.89% (E=3.11%, EPS=0.5)



X:\XRD Data\Uedadiah\Series 1\SF2-A.xrdml

Friday, September 06, 2019, 1:00 PM • US Army Corp Engineers

Scan ID: SF2-B.xrdml

Scan Parameters: 2.511°/69.99°/0.01671°/219.71(s), φ=0.0°, I(p)=4225.0/298.0, Co(45kV,40mA), Friday, November 11, 2016, 1:12

- Zero Offset = -0.0931 (0.0535) Displacement = 0.0 Distance Slack = 0.0
- Ka2 Peaks Present Ka2/Ka1 Ratio = 0.5 X-Ray Polarization = 1.0

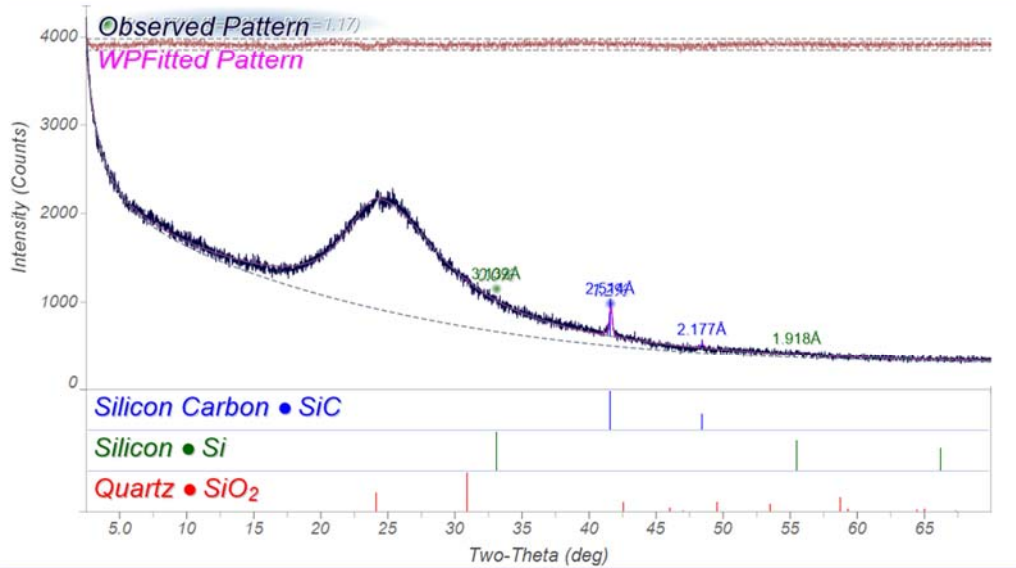
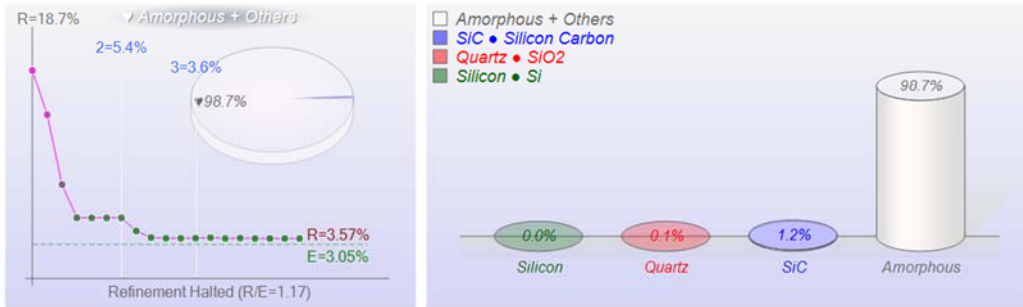
Geometry: Diffractometer Lp Fitted-Range: 2.5° - 70.0° BG-Model: Polynomial (3) λ: 1.78899 Å (Co)

PSF: pseudo-Voigt Broadening: Individual FWHM Curve Instrument: Constant FWHM = 0.1°

Phase ID (3)	Chemical Formula	PDF-#	Wt%	RIR	μ
Silicon Carbon (?)	SiC	04-002-9070	1.2	3.79	217.7
Silicon	Si	04-012-7888	0.0	4.91	217.9
Quartz	SiO ₂	01-089-1961	0.1	4.06	139.9
Amorphous + Others	SiO ₂		98.7	2.50	

XRF(Wt%): SiO₂=100.7%, CO₂=1.3%

Refinement Halted (R/E=1.17), ♦ Round=3, Iter=6, P=22, R=3.57% (E=3.05%, EPS=0.5)



X:\XRD Data\Uedadiah\Series 1\SF2-B.xrdml

Friday, September 06, 2019, 1:01 PM • US Army Corp Engineers

Scan ID: SF2-C.xrdml

Scan Parameters: 2.511°/69.99°/0.01671°/219.71(s), φ=0.0°, I(p)=3864.0/295.0, Co(45kV,40mA), Friday, November 11, 2016, 3:13

- Zero Offset = -0.0324 (0.0081) Displacement = 0.0 Distance Slack = 0.0
- Ka2 Peaks Present Ka2/Ka1 Ratio = 0.5 X-Ray Polarization = 1.0

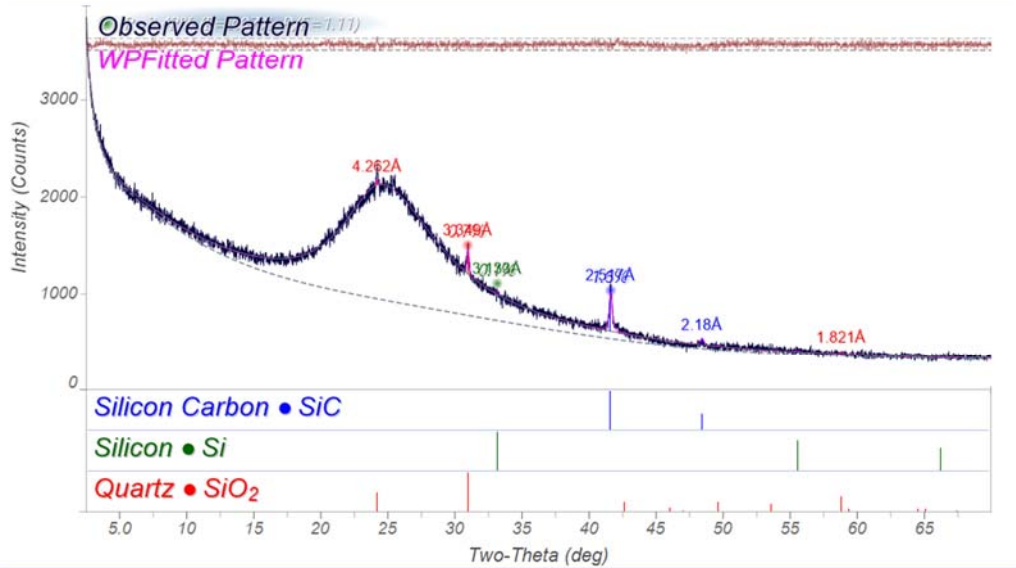
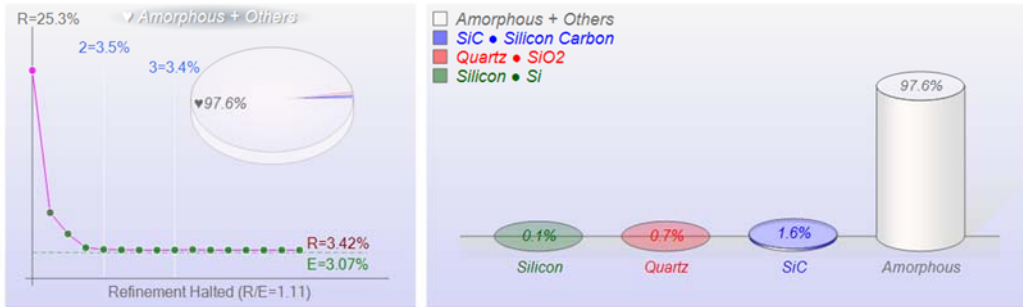
Geometry: Diffractometer Lp Fitted-Range: 2.5° - 70.0° BG-Model: Polynomial (6) λ: 1.78899 Å (Co)

PSF: pseudo-Voigt Broadening: Individual FWHM Curve Instrument: Constant FWHM = 0.1°

Phase ID (3)	Chemical Formula	PDF-#	Wt%	RIR	μ
Silicon Carbon (?)	SiC	04-002-9070	1.6	3.79	216.8
Silicon	Si	04-012-7888	0.1	4.91	217.7
Quartz (?)	SiO ₂	01-089-1961	0.7	4.06	139.9
Amorphous + Others	SiO ₂		97.6	2.50	

XRF(Wt%): SiO₂=100.9%, CO₂=1.8%

Refinement Halted (R/E=1.11), ♦ Round=3, Iter=6, P=25, R=3.42% (E=3.07%, EPS=0.5)



X:\XRD Data\Uedadiah\Series 1\SF2-C.xrdml

Friday, September 06, 2019, 1:02 PM • US Army Corp Engineers

Scan ID: SF3-A.xrdml

Scan Parameters: 2.511°/69.99°/0.01671°/219.71(s), $\phi=0.0^\circ$, $I(p)=3860.0/384.0$, Co(45kV,40mA), Friday, November 11, 2016, 5:14

- Zero Offset = 0.2436 (0.0144) Displacement = 0.0 Distance Slack = 0.0
- Ka2 Peaks Present Ka2/Ka1 Ratio = 0.5 X-Ray Polarization = 1.0

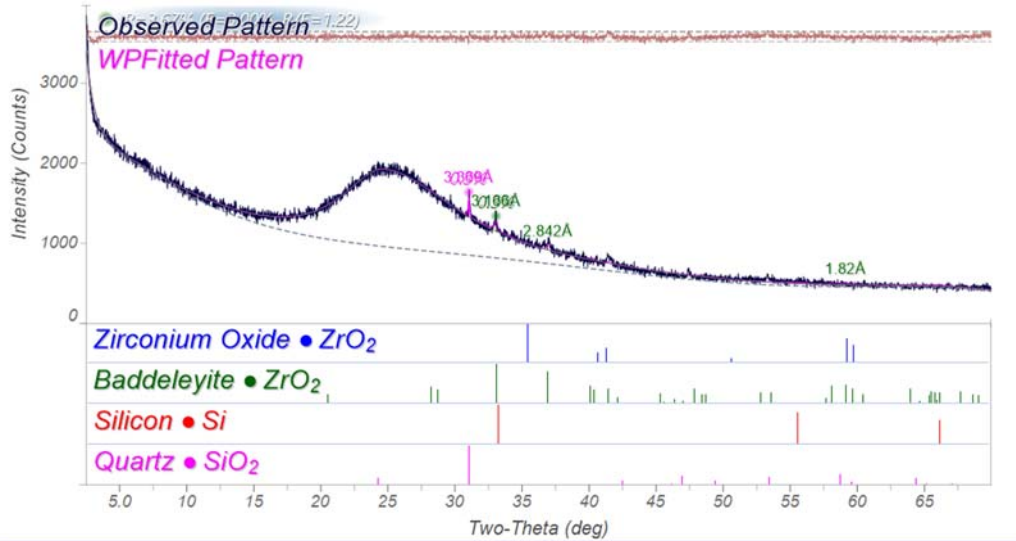
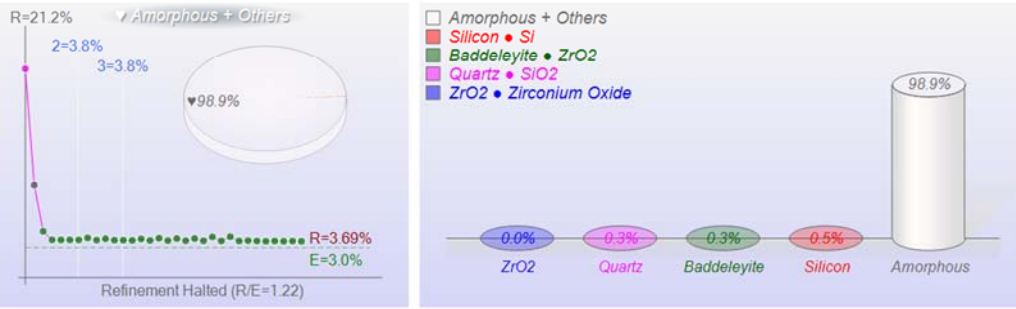
Geometry: Diffractometer Lp Fitted-Range: 2.5° - 70.0° BG-Model: Polynomial (5) λ : 1.78899 Å (Co)

PSF: pseudo-Voigt Broadening: Individual FWHM Curve Instrument: Constant FWHM = 0.1°

Phase ID (4)	Chemical Formula	PDF-#	Wt%	RIR	μ
Zirconium Oxide	ZrO ₂	04-005-4207	0.0	10.62	999.4
Baddeleyite (?)	ZrO ₂	04-004-4339	0.3	5.01	955.8
Silicon	Si	04-012-7888	0.5	4.91	214.8
Quartz (PO) (?)	SiO ₂	04-008-4821	0.3	4.34	137.2
Amorphous + Others	SiO ₂		98.9	2.50	

XRF(Wt%): ZrO₂=0.3%, SiO₂=100.3%

Refinement Halted (R/E=1.22), ♦ Round=3, Iter=6, P=28, R=3.67% (E=3.00%, EPS=0.5)



X:\XRD Data\Uedadiah\Series 1\SF3-A.xrdml

Friday, September 06, 2019, 1:26 PM • US Army Corp Engineers

Scan ID: SF3-B.xrdml

Scan Parameters: 2.511°/69.99°/0.01671°/219.71(s), $\phi=0.0^\circ$, $I(p)=4257.0/372.0$, Co(45kV,40mA), Friday, November 11, 2016, 7:15

- Zero Offset = -0.0359 (0.0046) Displacement = 0.0 Distance Slack = 0.0
- Ka2 Peaks Present Ka2/Ka1 Ratio = 0.5 X-Ray Polarization = 1.0

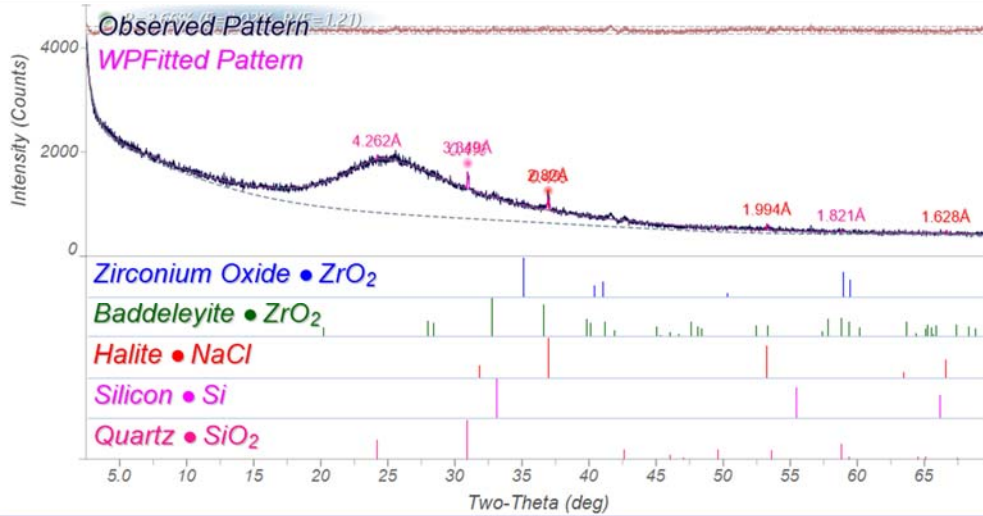
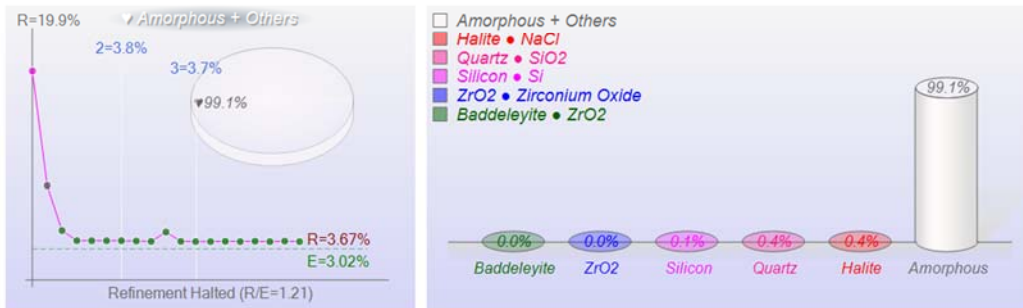
Geometry: Diffractometer Lp Fitted-Range: 2.5° - 70.0° BG-Model: Polynomial (5) λ : 1.78899 Å (Co)

PSF: pseudo-Voigt Broadening: Individual FWHM Curve Instrument: Constant FWHM = 0.1°

Phase ID (5)	Chemical Formula	PDF-#	Wt%	RIR	μ
Zirconium Oxide (?)	ZrO ₂	04-005-4207	0.0	10.62	999.4
Baddeleyite	ZrO ₂	04-004-4339	0.0	5.01	955.8
Halite (?)	NaCl	04-002-1178	0.4	5.21	250.9
Silicon	Si	04-012-7888	0.1	4.91	217.3
Quartz	SiO ₂	01-089-1961	0.4	4.06	139.9
Amorphous + Others	SiO ₂		99.1	2.50	

XRF(Wt%): ZrO₂=0.0%, SiO₂=99.7%, Na₂O=0.2%

Refinement Halted (R/E=1.21), Round=3, Iter=6, P=28, R=3.66% (E=3.02%, EPS=0.5)



Scan ID: SF3-C.xrdml

Scan Parameters: 2.511°/69.99°/0.01671°/219.71(s), $\phi=0.0^\circ$, $I(p)=4323.0/380.0$, Co(45kV,40mA), Friday, November 11, 2016, 9:16

- Zero Offset = 0.0292 (0.0096) Displacement = 0.0 Distance Slack = 0.0
- Ka2 Peaks Present Ka2/Ka1 Ratio = 0.5 X-Ray Polarization = 1.0

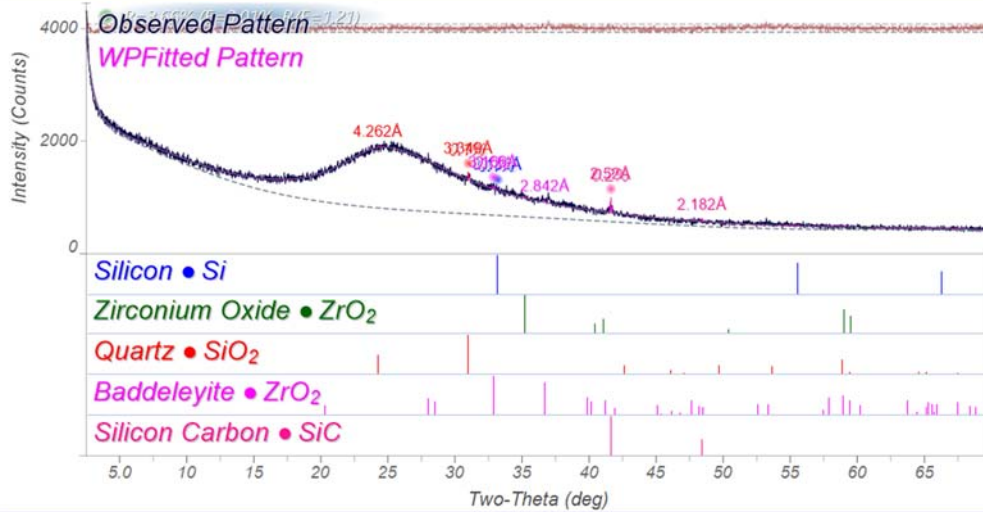
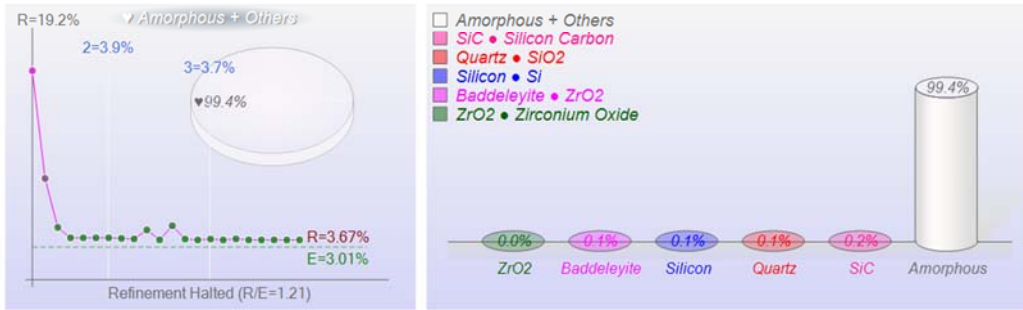
Geometry: Diffractometer Lp Fitted-Range: 2.5° - 70.0° BG-Model: Polynomial (5) λ : 1.78899 Å (Co)

PSF: pseudo-Voigt Broadening: Individual FWHM Curve Instrument: Constant FWHM = 0.1°

Phase ID (5)	Chemical Formula	PDF-#	Wt%	RIR	μ
Silicon	Si	04-012-7888	0.1	4.91	217.4
Zirconium Oxide	ZrO ₂	04-005-4207	0.0	10.62	999.4
Quartz	SiO ₂	01-089-1961	0.1	4.06	139.9
Baddeleyite	ZrO ₂	04-004-4339	0.1	5.01	955.8
Silicon Carbon (?)	SiC	04-002-9070	0.2	3.79	216.3
Amorphous + Others	SiO ₂		99.4	2.50	

XRF(Wt%): ZrO₂=0.1%, SiO₂=100.1%, CO₂=0.3%

Refinement Halted (R/E=1.21), Round=3, Iter=6, P=28, R=3.66% (E=3.01%, EPS=0.5)



X:\XRD Data\Uedadiah\Series 1\SF3-C.xrdml

Friday, September 06, 2019, 1:35 PM • US Army Corp Engineers

Scan ID: SF4-A.xrdml

Scan Parameters: 2.511°/69.99°/0.01671°/219.71(s), $\phi=0.0^\circ$, $I(p)=2975.0/298.0$, Co(45kV,40mA), Wednesday, June 14, 2017, 2:32

- Zero Offset = -0.0908 (0.0266) Displacement = 0.0 Distance Slack = 0.0
- Ka2 Peaks Present Ka2/Ka1 Ratio = 0.5 X-Ray Polarization = 1.0

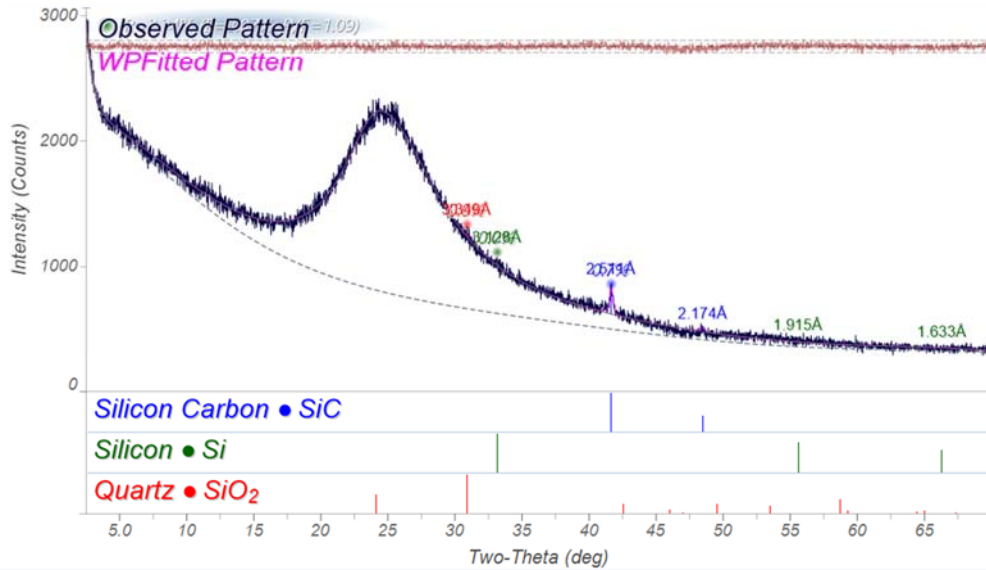
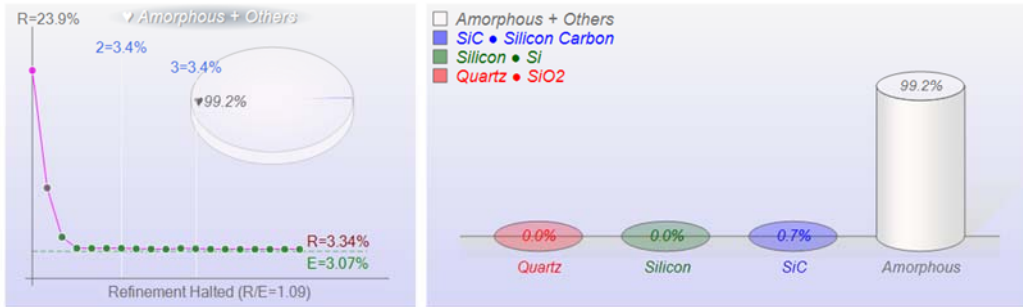
Geometry: Diffractometer Lp Fitted-Range: 2.5° - 70.0° BG-Model: Polynomial (5) λ : 1.78899 Å (Co)

PSF: pseudo-Voigt Broadening: Individual FWHM Curve Instrument: Constant FWHM = 0.1°

Phase ID (3)	Chemical Formula	PDF-#	Wt%	RIR	μ
Silicon Carbon	SiC	04-002-9070	0.7	3.79	218.4
Silicon	Si	04-012-7888	0.0	4.91	218.9
Quartz (?)	SiO ₂	01-089-1961	0.0	4.06	139.9
Amorphous + Others	SiO ₂		99.2	2.50	

XRF(Wt%): SiO₂=100.4%, CO₂=0.8%

Refinement Halted (R/E=1.09), Round=3, Iter=6, P=24, R=3.34% (E=3.07%, EPS=0.5)



X:\XRD Data\Uedadiah\Series 1\SF4-A.xrdml

Friday, September 06, 2019, 1:03 PM • US Army Corp Engineers

Scan ID: SF5-A.xrdml

Scan Parameters: 2.511°/69.99°/0.01671°/219.71(s), φ=0.0°, I(p)=1626.0/292.0, Co(45kV,40mA), Friday, November 16, 2018, 4:04

- Zero Offset = -0.0675 (0.0186) Displacement = 0.0 Distance Slack = 0.0
- Ka2 Peaks Present Ka2/Ka1 Ratio = 0.5 X-Ray Polarization = 1.0

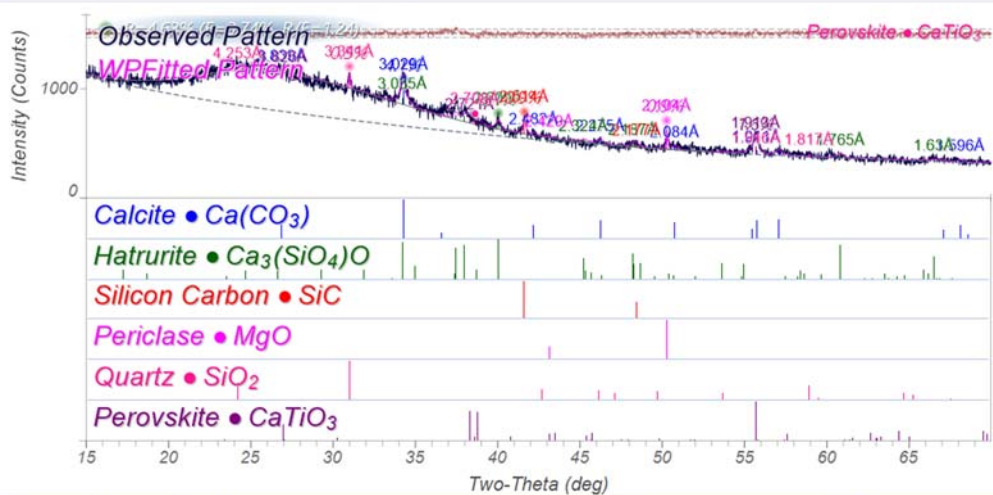
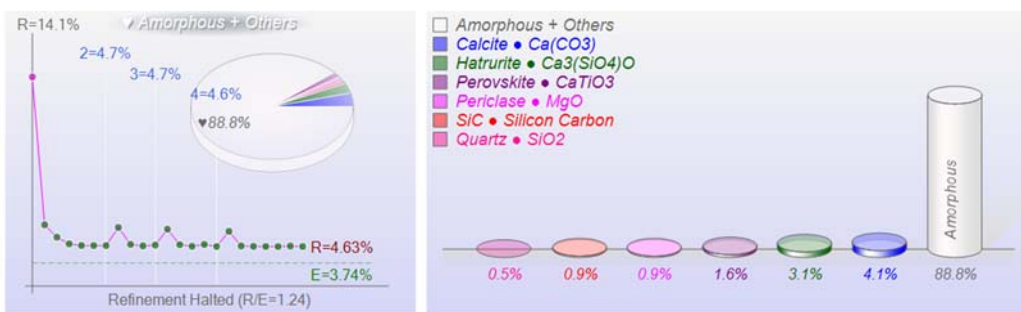
Geometry: Diffractometer Lp Fitted-Range: 15.0° - 70.0° BG-Model: Polynomial (5) λ: 1.78899 Å (Co)

PSF: pseudo-Voigt Broadening: Individual FWHM Curve Instrument: Constant FWHM = 0.1°

Phase ID (6)	Chemical Formula	PDF-#	Wt%	RIR	μ
Calcite	Ca(CO ₃)	04-012-8072	4.1	3.03	292.1
Hatruite (?)	Ca ₃ (SiO ₄)O	04-011-1393	3.1	1.27	459.9
Silicon Carbon	SiC	04-002-9070	0.9	3.79	217.5
Periclase	MgO	04-012-3469	0.9	3.34	154.4
Quartz	SiO ₂	04-012-0490	0.5	4.27	140.9
Perovskite (PO) (?)	CaTiO ₃	04-007-5451	1.6	2.55	752.6
Amorphous + Others	SiO ₂		88.8	2.50	

XRF(Wt%): TiO₂=0.9%, CaO=5.3%, SiO₂=91.5%, MgO=0.9%, CO₂=2.8%

Refinement Halted (R/E=1.24), Round=4, Iter=6, P=41, R=4.63% (E=3.74%, EPS=0.5)



X:\XRD Data\Jedariah\Series 1\SF5-A.xrdml

Friday, September 06, 2019, 1:47 PM • US Army Corp Engineers

Scan ID: SF5-B.xrdml

Scan Parameters: 2.511°/69.99°/0.01671°/219.71(s), φ=0.0°, I(p)=2768.0/279.0, Co(45kV,40mA), Friday, November 04, 2016, 9:25

- Zero Offset = -0.0853 (0.0076) Displacement = 0.0 Distance Slack = 0.0
- Ka2 Peaks Present Ka2/Ka1 Ratio = 0.5 X-Ray Polarization = 1.0

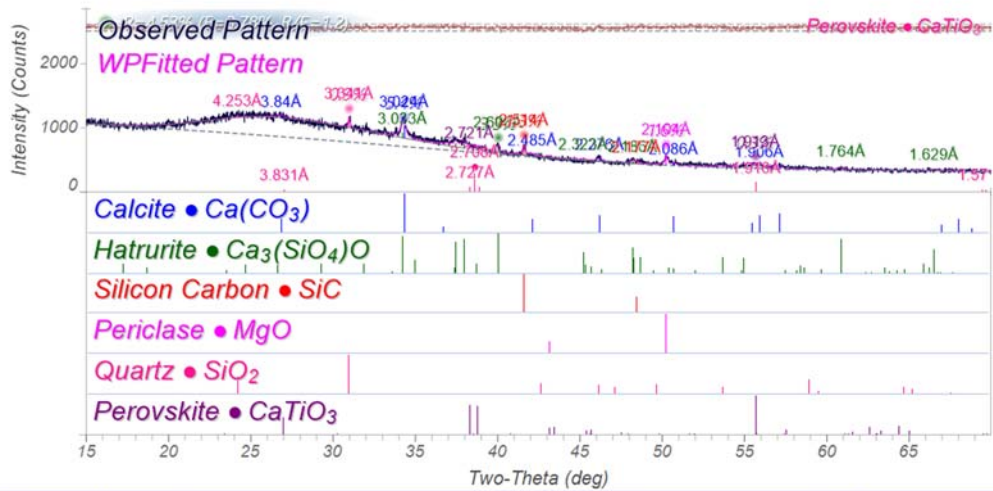
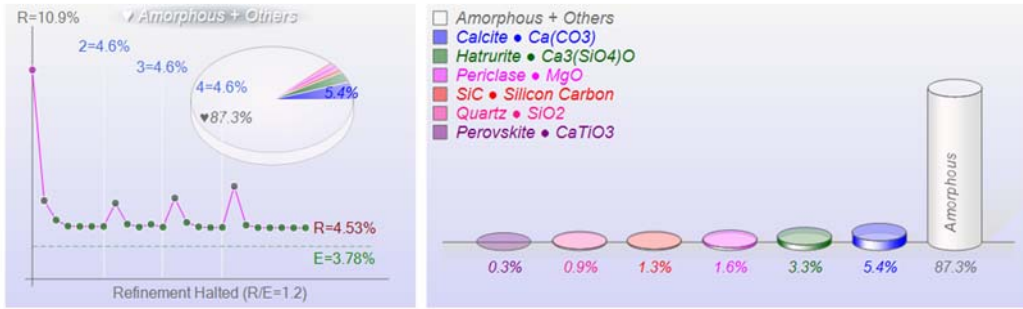
Geometry: Diffractometer Lp Fitted-Range: 15.0° - 70.0° BG-Model: Polynomial (5) λ: 1.78899 Å (Co)

PSF: pseudo-Voigt Broadening: Individual FWHM Curve Instrument: Constant FWHM = 0.1°

Phase ID (6)	Chemical Formula	PDF-#	Wt%	RIR	μ
Calcite	Ca(CO ₃)	04-012-8072	5.4	3.03	292.5
Hatruite (?)	Ca ₃ (SiO ₄)O	04-011-1393	3.3	1.27	460.4
Silicon Carbon	SiC	04-002-9070	1.3	3.79	217.6
Periclase	MgO	04-012-3469	1.6	3.34	154.4
Quartz	SiO ₂	04-012-0490	0.9	4.27	140.9
Perovskite (PO)	CaTiO ₃	04-007-5451	0.3	2.55	752.6
Amorphous + Others	SiO ₂		87.3	2.50	

XRF(Wt%): TiO₂=0.2%, CaO=5.5%, SiO₂=91.0%, MgO=1.6%, CO₂=3.7%

Refinement Halted (R/E=1.2), ♦ Round=4, Iter=6, P=36, R=4.53% (E=3.78%, EPS=0.5)



X:\XRD Data\Jedaliah\Series 1\SF5-B.xrdml

Friday, September 06, 2019, 1:55 PM • US Army Corp Engineers

Scan ID: SF6-A.xrdml

Scan Parameters: 2.511°/69.99°/0.01671°/219.71(s), $\phi=0.0^\circ$, $I(p)=3518.0/312.0$, Co(45kV,40mA), Friday, November 11, 2016, 11:1

- Zero Offset = -0.0533 (0.0472) Displacement = 0.0 Distance Slack = 0.0
- Ka2 Peaks Present Ka2/Ka1 Ratio = 0.5 X-Ray Polarization = 1.0

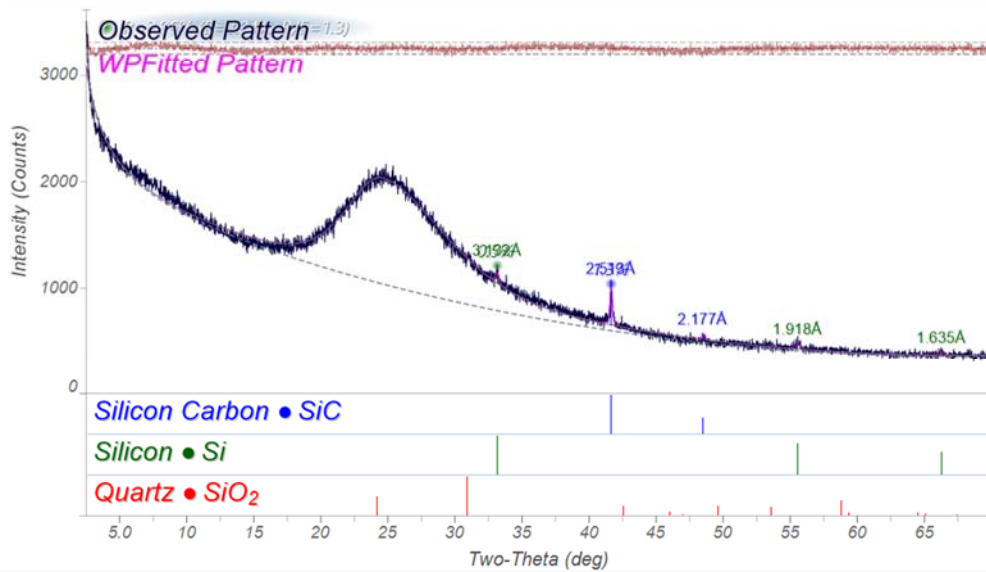
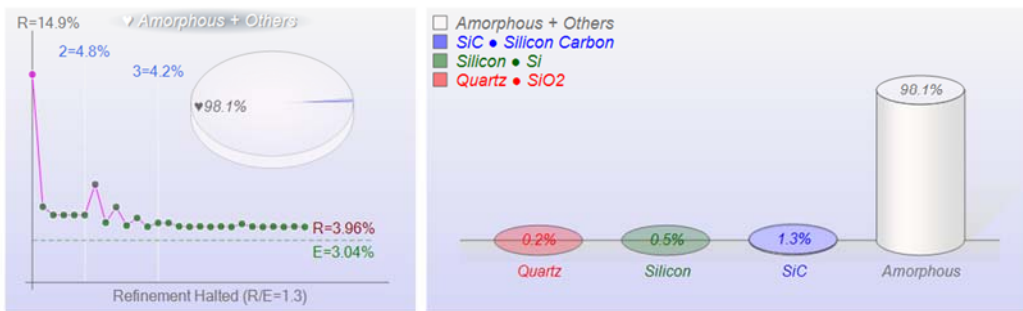
Geometry: Diffractometer Lp Fitted-Range: 2.5° - 70.0° BG-Model: Polynomial (2) λ : 1.78899 Å (Co)

PSF: pseudo-Voigt Broadening: Individual FWHM Curve Instrument: Constant FWHM = 0.1°

Phase ID (3)	Chemical Formula	PDF-#	Wt%	RIR	μ
Silicon Carbon (?)	SiC	04-002-9070	1.3	3.79	217.8
Silicon	Si	04-012-7888	0.5	4.91	218.1
Quartz	SiO ₂	01-089-1961	0.2	4.06	139.9
Amorphous + Others	SiO ₂		98.1	2.50	

XRF(Wt%): SiO₂=101.2%, CO₂=1.4%

Refinement Halted (R/E=1.3), ♦ Round=3, Iter=6, P=21, R=3.96% (E=3.04%, EPS=0.5)



X:\XRD Data\Uedadiah\Series 1\SF6-A.xrdml

Friday, September 06, 2019, 12:43 PM • US Army Corp Engineers

Scan ID: SF6-B.xrdml

Scan Parameters: 2.511°/69.99°/0.01671°/219.71(s), $\phi=0.0^\circ$, $I(p)=3841.0/329.0$, Co(45kV,40mA), Friday, November 11, 2016, 1:18

- Zero Offset = -0.003 (?) Displacement = 0.0 Distance Slack = 0.0
- Ka2 Peaks Present Ka2/Ka1 Ratio = 0.5 X-Ray Polarization = 1.0

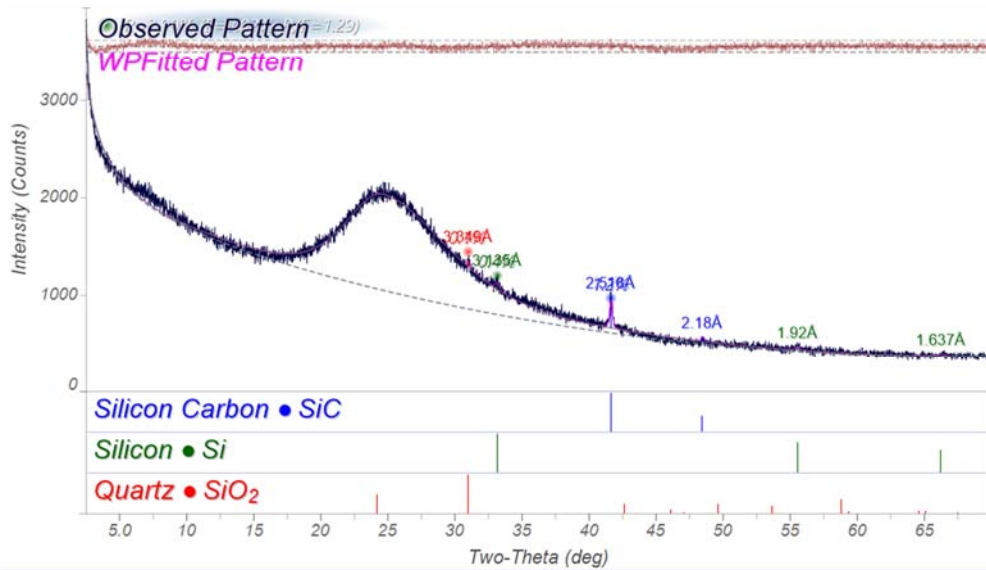
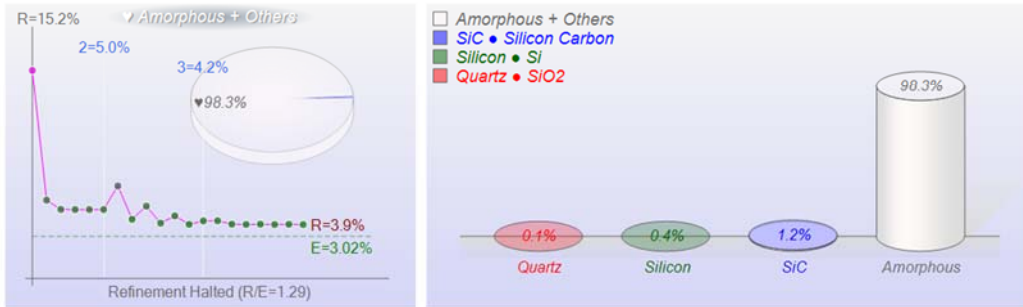
Geometry: Diffractometer Lp Fitted-Range: 2.5° - 70.0° BG-Model: Polynomial (2) λ : 1.78899 Å (Co)

PSF: pseudo-Voigt Broadening: Individual FWHM Curve Instrument: Constant FWHM = 0.1°

Phase ID (3)	Chemical Formula	PDF-#	Wt%	RIR	μ
Silicon Carbon (?)	SiC	04-002-9070	1.2	3.79	216.7
Silicon	Si	04-012-7888	0.4	4.91	217.4
Quartz	SiO ₂	01-089-1961	0.1	4.06	139.9
Amorphous + Others	SiO ₂		98.3	2.50	

XRF(Wt%): SiO2=101.0%, CO2=1.3%

Refinement Halted (R/E=1.29), ♦ Round=3, Iter=6, P=21, R=3.9% (E=3.02%, EPS=0.5)



X:\XRD Data\Jedadiah\Series 1\SF6-B.xrdml

Friday, September 06, 2019, 12:44 PM • US Army Corp Engineers

Scan ID: SF6-C.xrdml

Scan Parameters: 2.511°/69.99°/0.01671°/219.71(s), $\phi=0.0^\circ$, $I(p)=4546.0/312.0$, Co(45kV,40mA), Friday, November 11, 2016, 3:19

- Zero Offset = 0.0313 (0.0097) Displacement = 0.0 Distance Slack = 0.0
- Ka2 Peaks Present Ka2/Ka1 Ratio = 0.5 X-Ray Polarization = 1.0

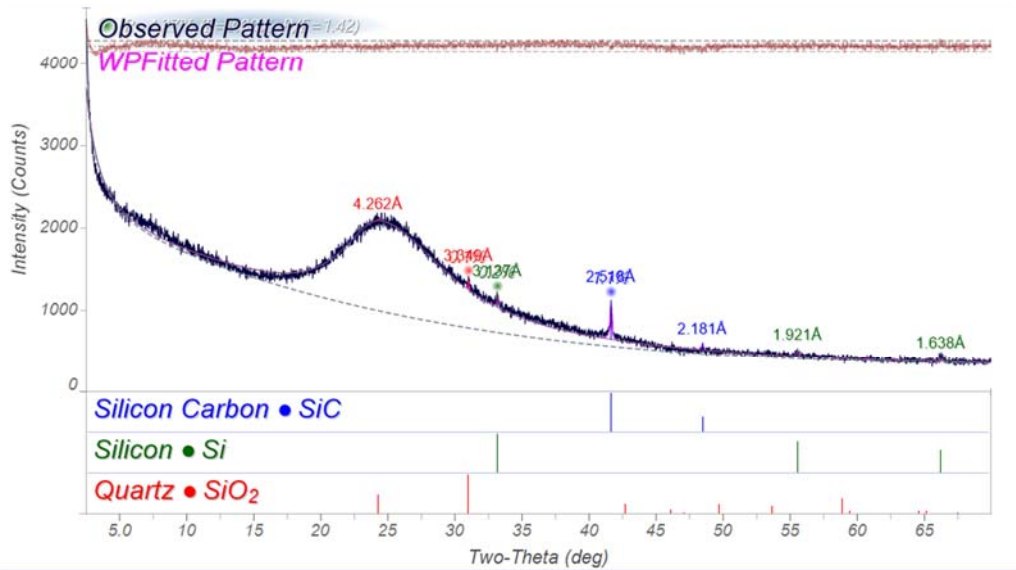
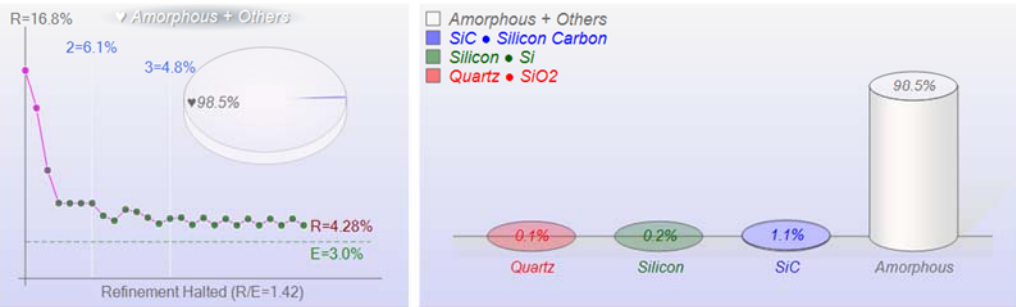
Geometry: Diffractometer Lp Fitted-Range: 2.5° - 70.0° BG-Model: Polynomial (3) λ : 1.78899 Å (Co)

PSF: pseudo-Voigt Broadening: Individual FWHM Curve Instrument: Constant FWHM = 0.1°

Phase ID (3)	Chemical Formula	PDF-#	Wt%	RIR	μ
Silicon Carbon (?)	SiC	04-002-9070	1.1	3.79	216.5
Silicon	Si	04-012-7888	0.2	4.91	217.1
Quartz	SiO ₂	01-089-1961	0.1	4.06	139.9
Amorphous + Others	SiO ₂		98.5	2.50	

XRF(Wt%): SiO2=100.8%, CO2=1.2%

Refinement Halted (R/E=1.42), ♦ Round=3, Iter=11, P=22, R=4.27% (E=3.00%, EPS=0.5)



X:\XRD Data\Uedadiah\Series 1\SF6-C.xrdml

Friday, September 06, 2019, 12:44 PM • US Army Corp Engineers

SF7-A

WPF Report

Scan ID: SF7-A.xrdml • SF7-A

Scan Parameters: 2.511°/69.99°/0.01671°/219.71(s), $\phi=0.0^\circ$, $I(p)=3717.0/314.0$, Co(45kV,40mA), Friday, September 06, 2019, 10:...

- Zero Offset = -0.0103 (0.0323) Displacement = 0.0 Distance Slack = 0.0
- Ka2 Peaks Present Ka2/Ka1 Ratio = 0.5 X-Ray Polarization = 1.0

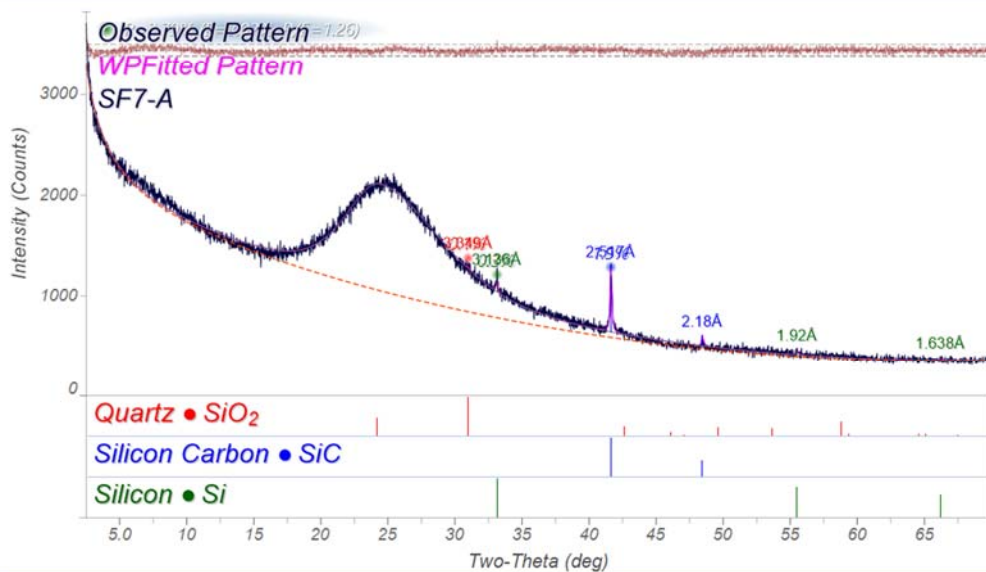
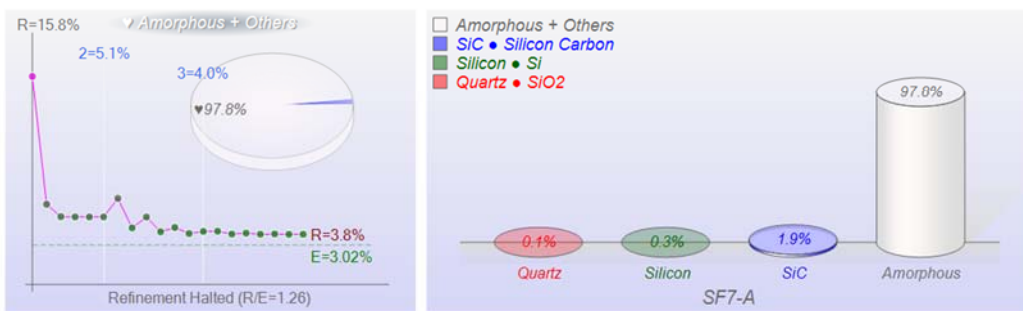
Geometry: Diffractometer Lp Fitted-Range: 2.5° - 70.0° BG-Model: Polynomial (2) λ : 1.78899 Å (Co)

PSF: pseudo-Voigt Broadening: Individual FWHM Curve Instrument: Constant FWHM = 0.1°

Phase ID (3)	Chemical Formula	PDF-#	Wt%	RIR	μ
Quartz	SiO ₂	01-089-1961	0.1	4.06	139.9
Silicon Carbon	SiC	04-002-9070	1.9	3.79	216.8
Silicon (?)	Si	04-012-7888	0.3	4.91	217.2
Amorphous + Others	SiO ₂		97.8	2.50	

XRF(Wt%): SiO2=101.2%, CO2=2.0%

Refinement Halted (R/E=1.26), ♦ Round=3, Iter=6, P=21, R=3.79% (E=3.02%, EPS=0.5)



X:\XRD Data\Uedadiah\Series 1\SF7-A.xrdml

Friday, September 06, 2019, 10:39 AM • US Army Corp Engineers

Scan ID: SF7-B.xrdml • SF7-B

Scan Parameters: 2.511°/69.99°/0.01671°/219.71(s), $\phi=0.0^\circ$, $I(p)=3566.0/310.0$, Co(45kV,40mA), Friday, September 06, 2019, 10:...

- Zero Offset = -0.005 (0.0027)
- Displacement = 0.0
- Distance Slack = 0.0
- Ka2 Peaks Present
- Ka2/Ka1 Ratio = 0.5
- X-Ray Polarization = 1.0

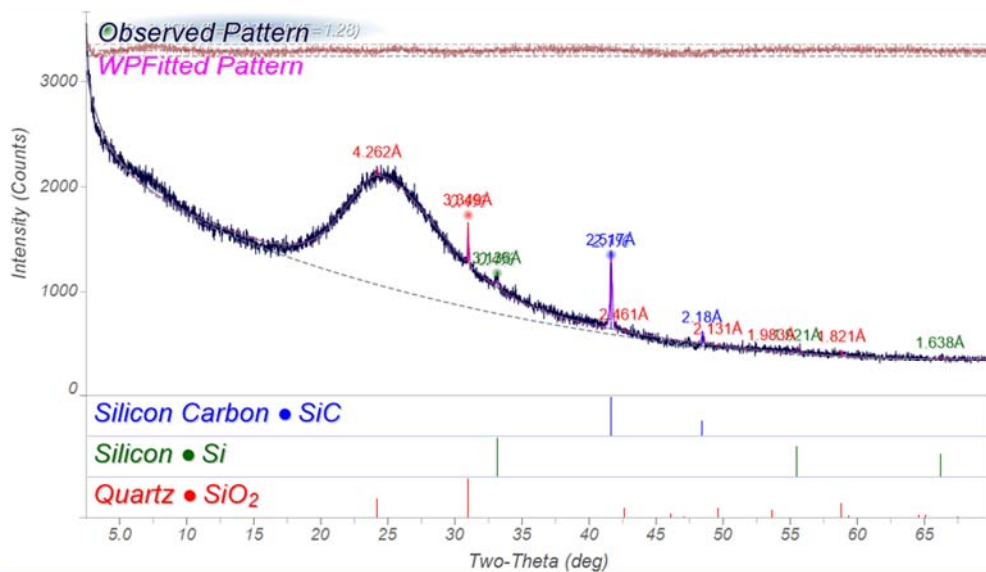
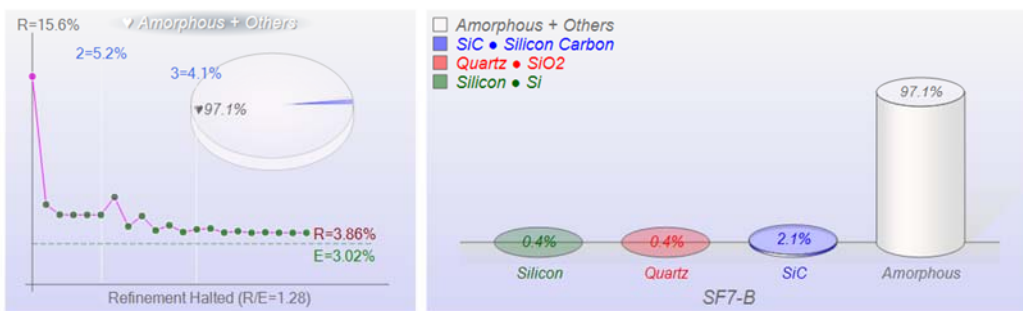
Geometry: Diffractometer Lp Fitted-Range: 2.5° - 70.0° BG-Model: Polynomial (2) λ : 1.78899 Å (Co)

PSF: pseudo-Voigt Broadening: Individual FWHM Curve Instrument: Constant FWHM = 0.1°

Phase ID (3)	Chemical Formula	PDF-#	Wt%	RIR	μ
Silicon Carbon (?)	SiC	04-002-9070	2.1	3.79	216.9
Silicon	Si	04-012-7888	0.4	4.91	217.1
Quartz	SiO ₂	01-089-1961	0.4	4.06	139.9
Amorphous + Others	SiO ₂		97.1	2.50	

XRF(Wt%): SiO₂=101.4%, CO₂=2.3%

Refinement Halted (R/E=1.28), ♦ Round=3, Iter=7, P=21, R=3.86% (E=3.02%, EPS=0.5)



Scan ID: SF7-C.xrdml • SF7-C

Scan Parameters: 2.511°/69.99°/0.01671°/219.71(s), $\phi=0.0^\circ$, $I(p)=3686.0/305.0$, Co(45kV,40mA), Friday, September 06, 2019, 10:00

- Zero Offset = -0.061 (0.0136) Displacement = 0.0 Distance Slack = 0.0
- Ka2 Peaks Present Ka2/Ka1 Ratio = 0.5 X-Ray Polarization = 1.0

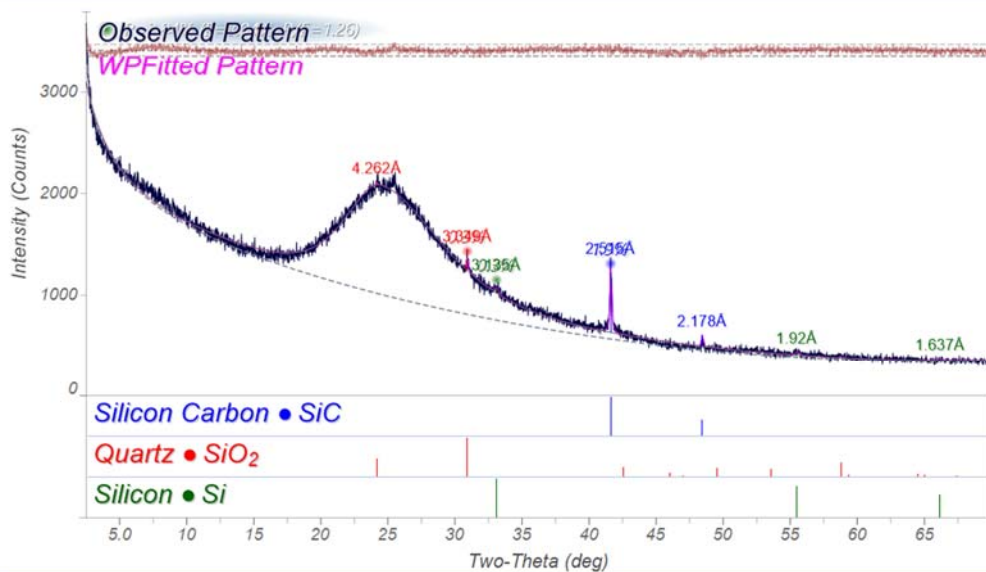
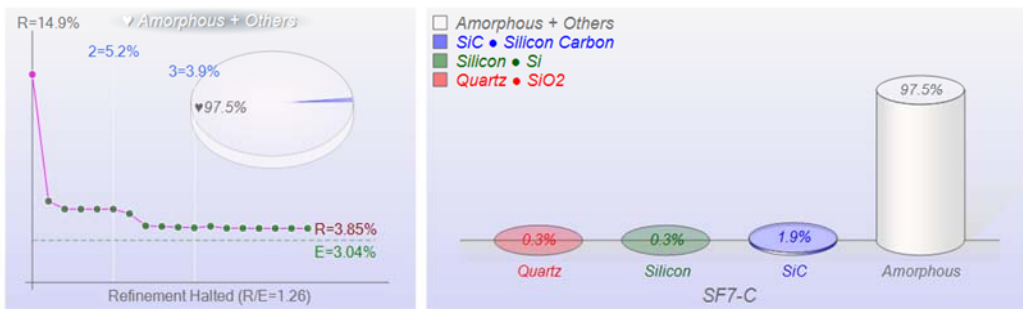
Geometry: Diffractometer Lp Fitted-Range: 2.5° - 70.0° BG-Model: Polynomial (2) λ : 1.78899 Å (Co)

PSF: pseudo-Voigt Broadening: Individual FWHM Curve Instrument: Constant FWHM = 0.1°

Phase ID (3)	Chemical Formula	PDF-#	Wt%	RIR	μ
Silicon Carbon (?)	SiC	04-002-9070	1.9	3.79	217.3
Quartz	SiO ₂	01-089-1961	0.3	4.06	139.9
Silicon	Si	04-012-7888	0.3	4.91	217.4
Amorphous + Others	SiO ₂		97.5	2.50	

XRF(Wt%): SiO2=101.3%, CO2=2.1%

Refinement Halted (R/E=1.26), ♦ Round=3, Iter=6, P=21, R=3.84% (E=3.04%, EPS=0.5)



X:\XRD Data\Jedadiah\Series 1\SF7-C.xrdml

Friday, September 06, 2019, 10:43 AM • US Army Corp Engineers

Scan ID: SF8-A.xrdml

Scan Parameters: 2.511°/69.99°/0.01671°/219.71(s), $\phi=0.0^\circ$, $I(p)=2966.0/293.0$, Co(45kV,40mA), Monday, July 11, 2016, 6:10 PM

- Zero Offset = -0.0466 (0.0079) Displacement = 0.0 Distance Slack = 0.0
- Ka2 Peaks Present Ka2/Ka1 Ratio = 0.5 X-Ray Polarization = 1.0

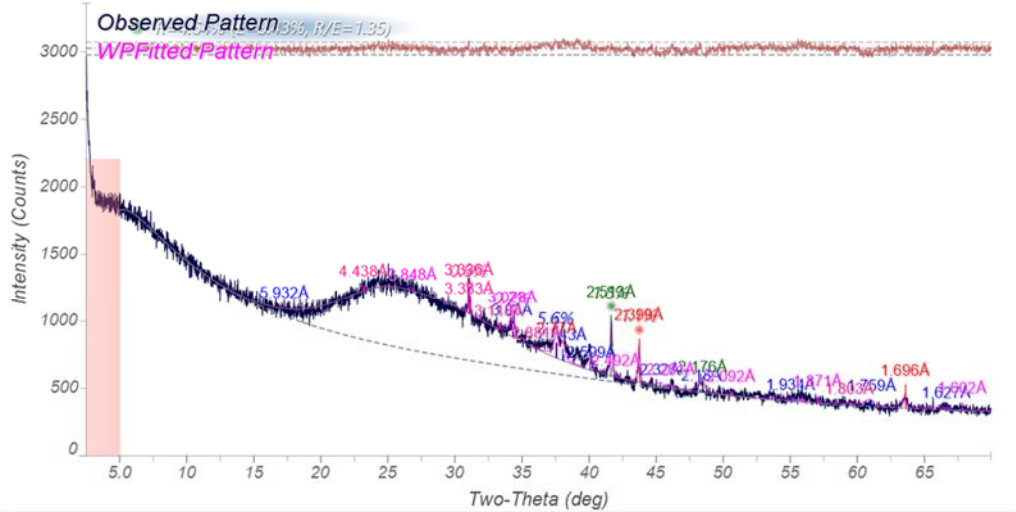
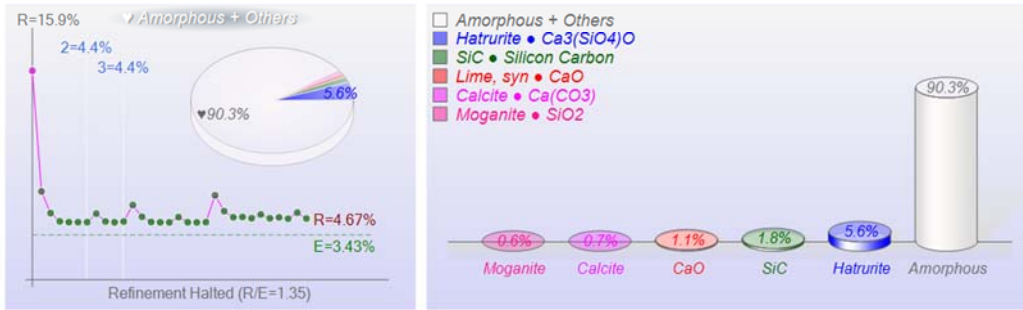
Geometry: Diffractometer Lp Fitted-Range: 5.0° - 70.0° BG-Model: Polynomial (5) λ : 1.78899 Å (Co)

PSF: pseudo-Voigt Broadening: Individual FWHM Curve Instrument: Constant FWHM = 0.1°

Phase ID (5)	Chemical Formula	PDF-#	Wt% (ESD)	RIR	μ
Hatrite (?)	<chem>Ca3(SiO4)O</chem>	04-014-9801	5.6 (0.4)	1.03	462.7
Silicon Carbon	<chem>SiC</chem>	04-002-9070	1.8 (0.1)	3.79	218.0
Lime, syn	<chem>CaO</chem>	04-003-7161	1.1 (0.1)	4.96	602.6
Calcite (?)	<chem>Ca(CO3)</chem>	04-012-0489	0.7 (0.1)	3.16	290.9
Moganite (PO)	<chem>SiO2</chem>	04-007-2116	0.6 (0.3)	1.27	138.9
Amorphous + Others	<chem>SiO2</chem>		90.3 (6.7)	2.50	

XRF(Wt%): CaO=5.5%, SiO2=95.1%, CO2=2.3%

Refinement Halted (R/E=1.35), Round=3, Iter=10, P=41, R=4.64% (E=3.43%, EPS=0.5)

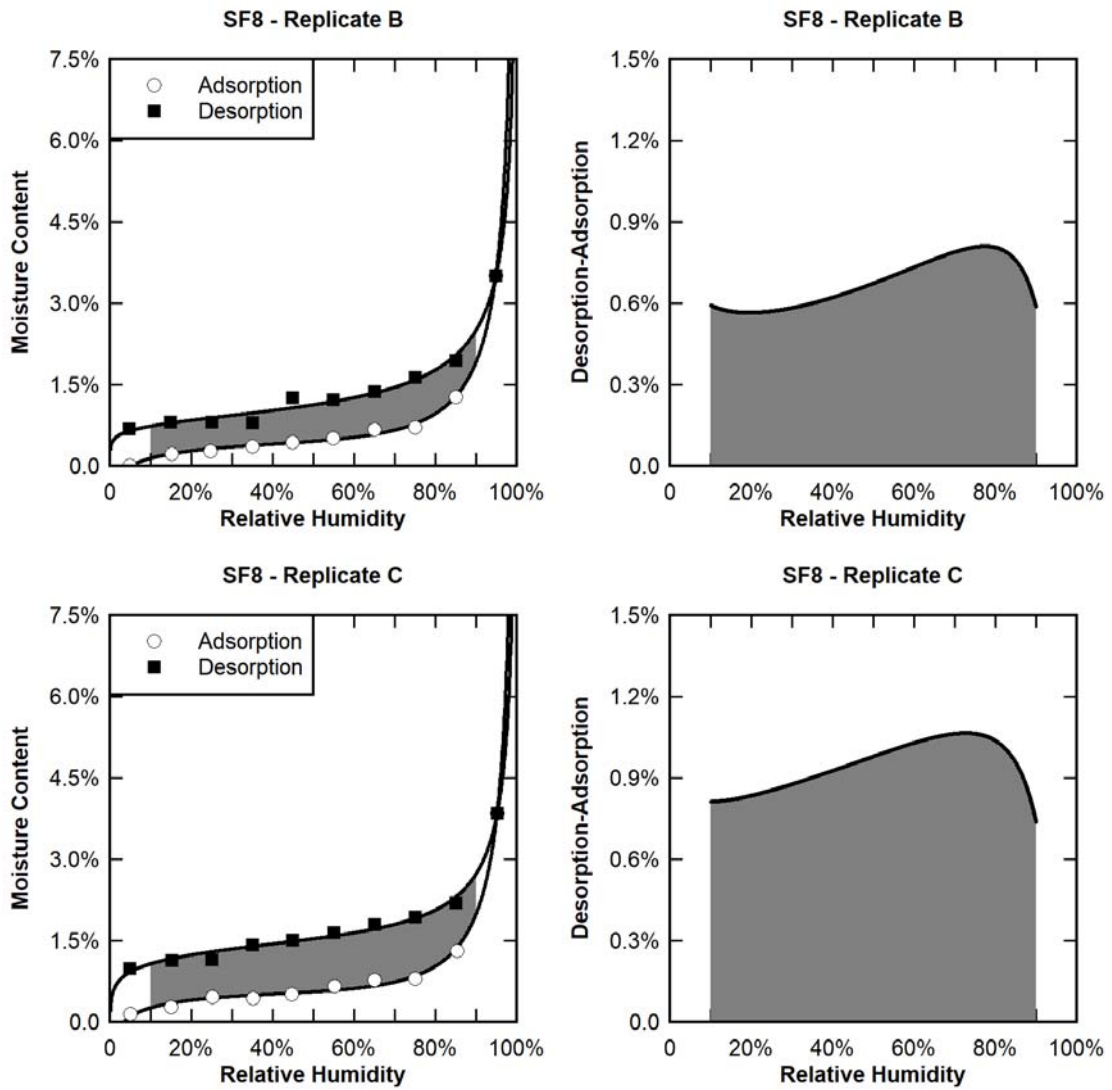


X:\XRD Data\JedadahSeries 1\SF8-A.xrdml

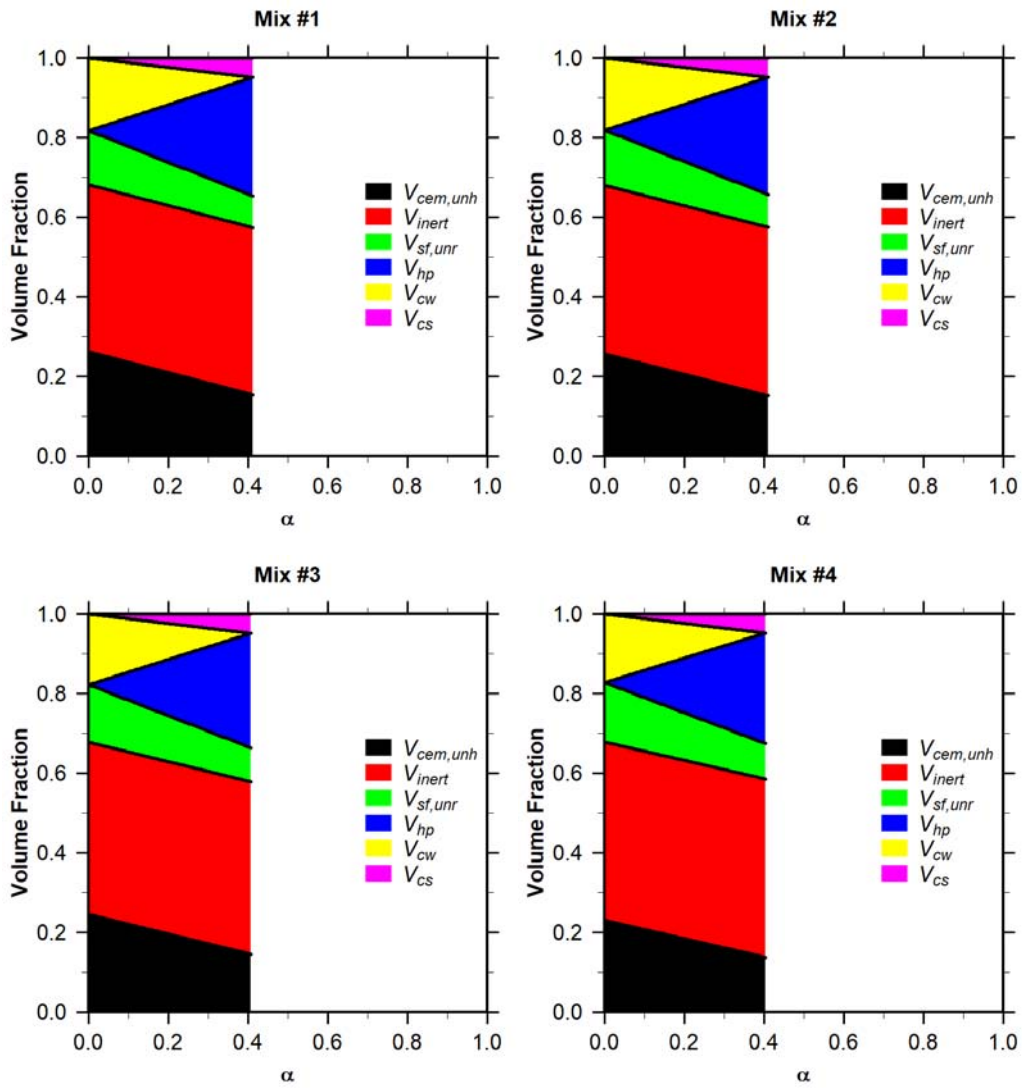
Wednesday, September 11, 2019, 9:06 AM • US Army Corp Engineers

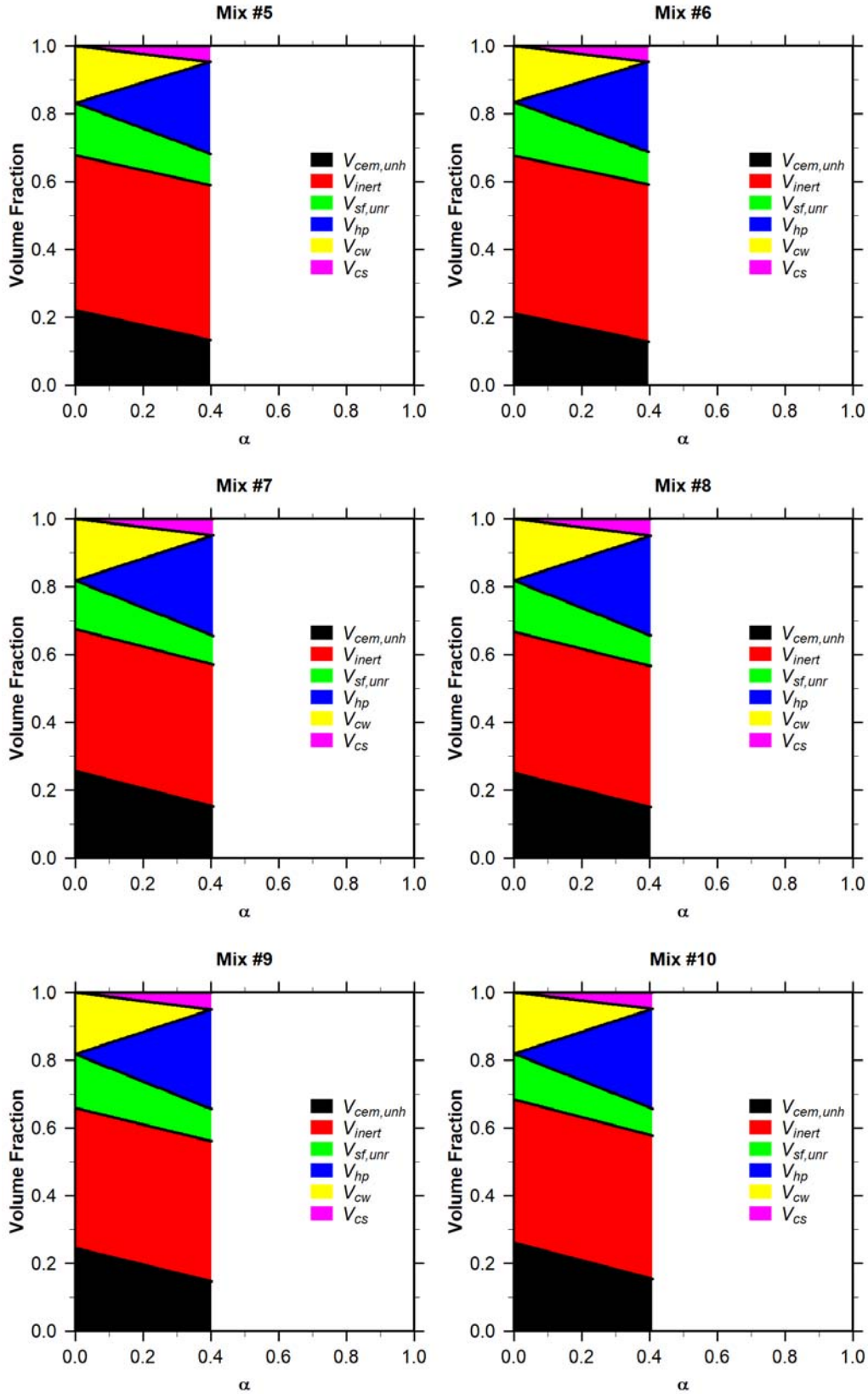
APPENDIX C. DYNAMIC VAPOR SORPTION ANALYSIS

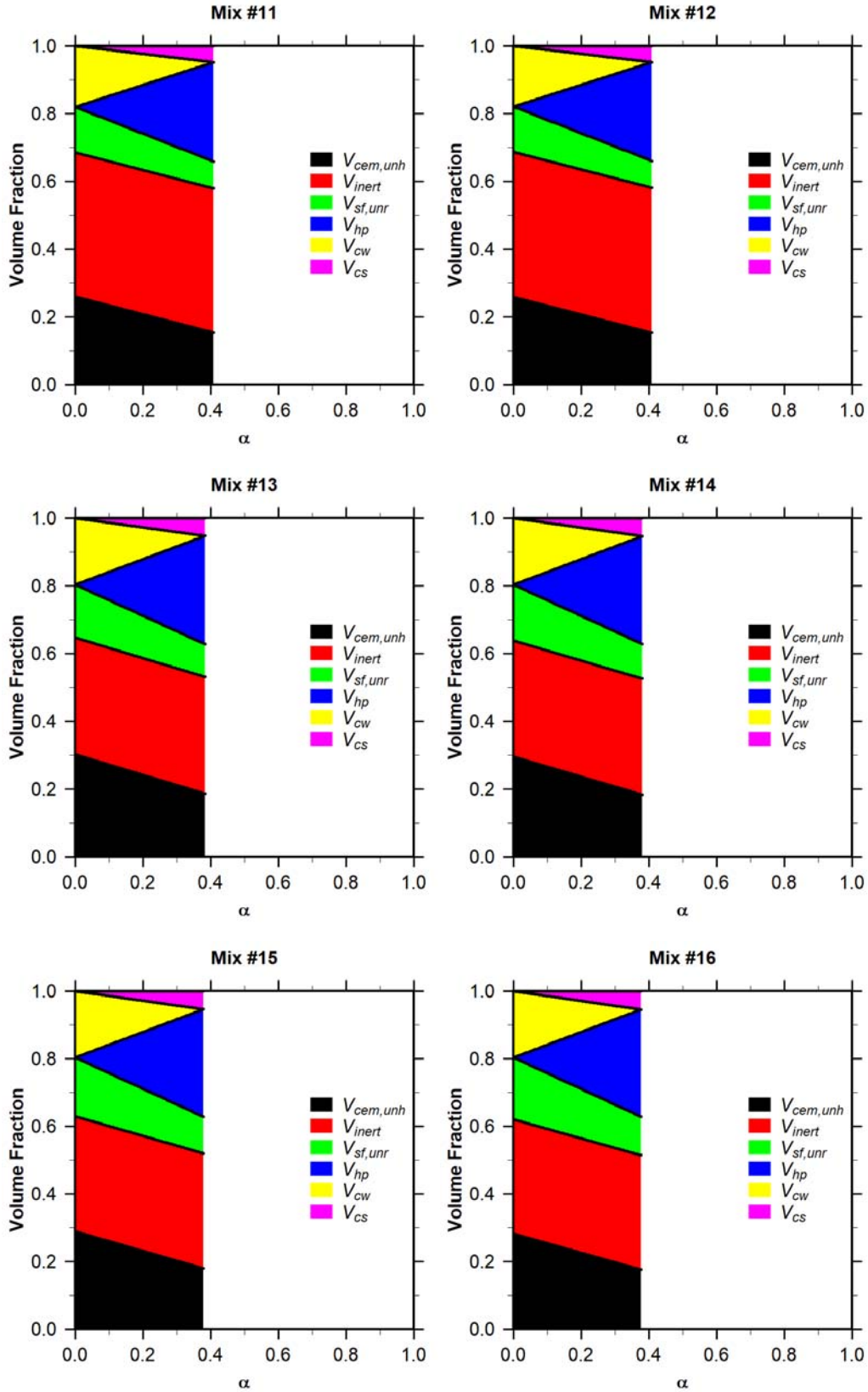
This appendix includes additional dynamic vapor sorption data and hysteresis area analysis for replicates of materials not included in Chapter 2.

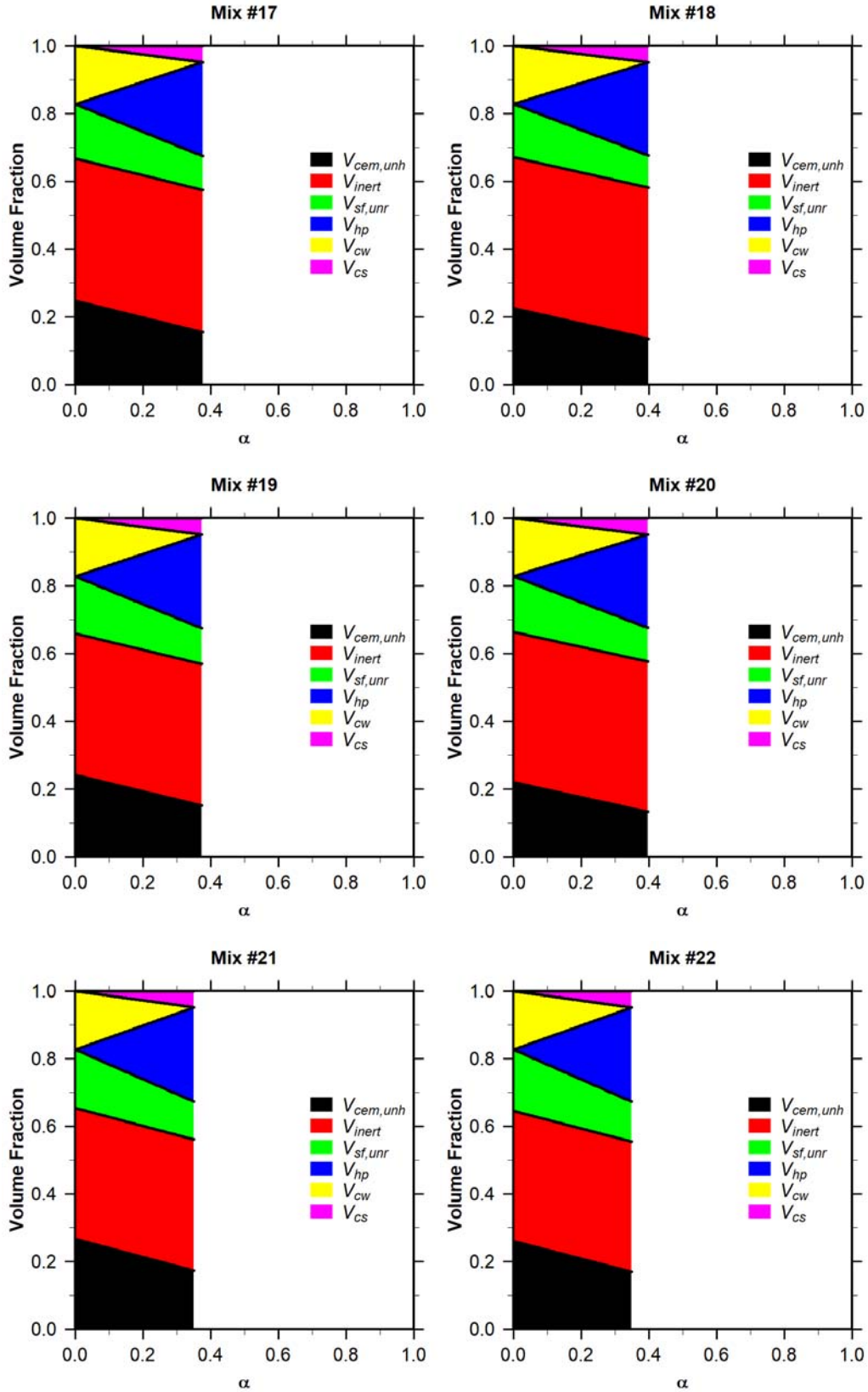


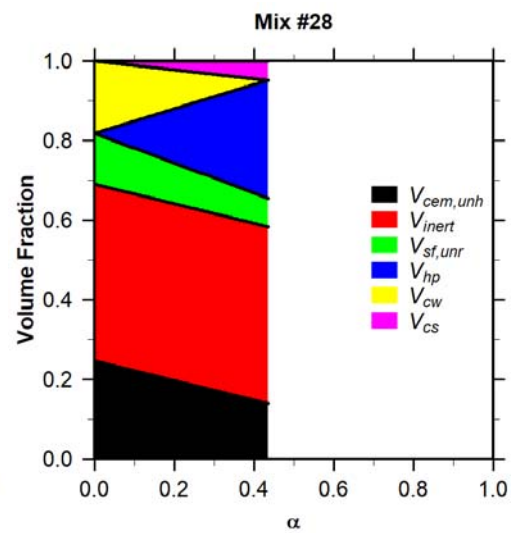
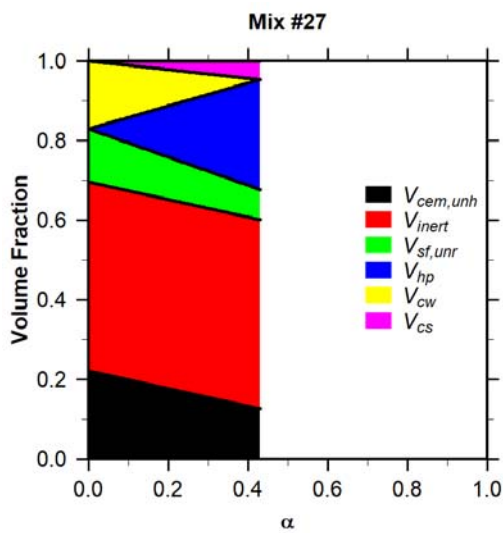
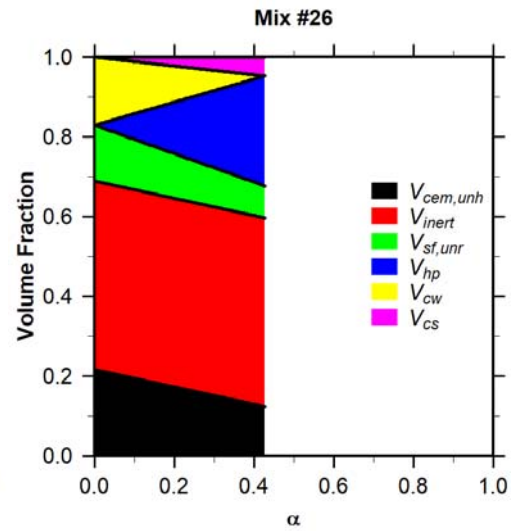
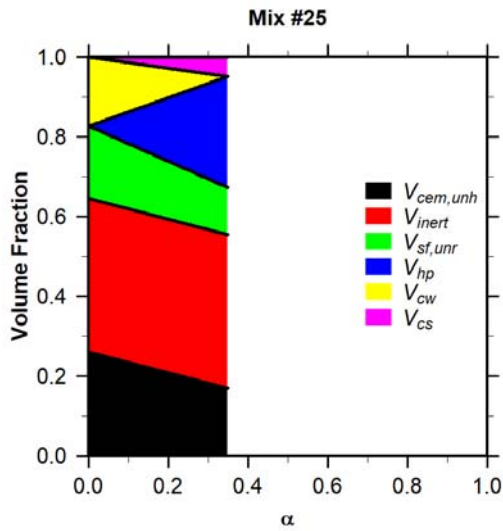
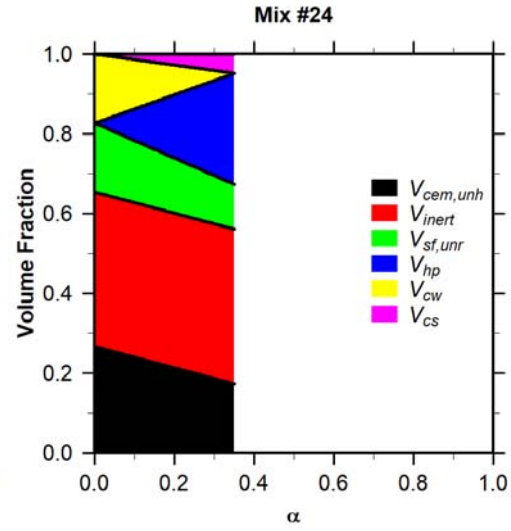
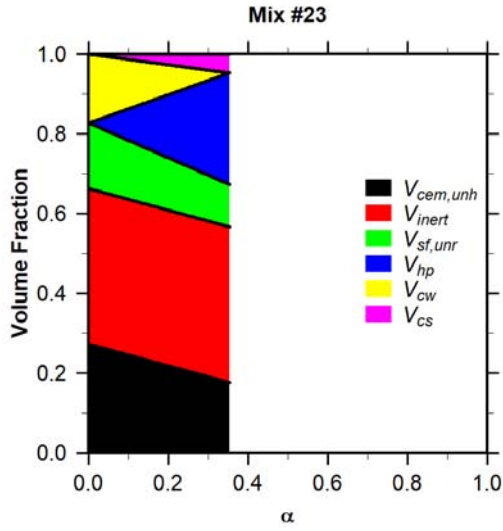
APPENDIX D. POWERS-BROWNYARD HYDRATION MODEL RESULTS

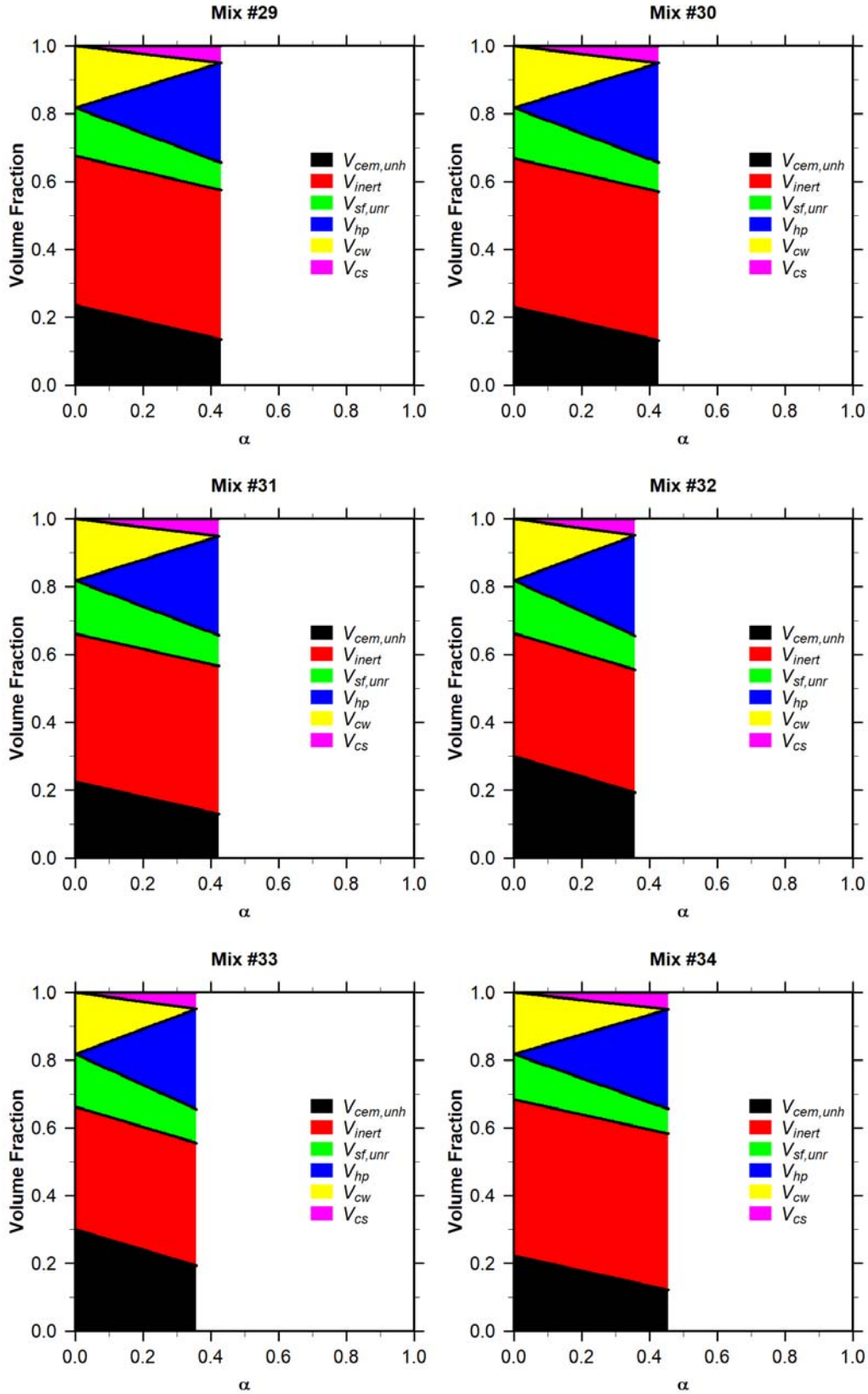


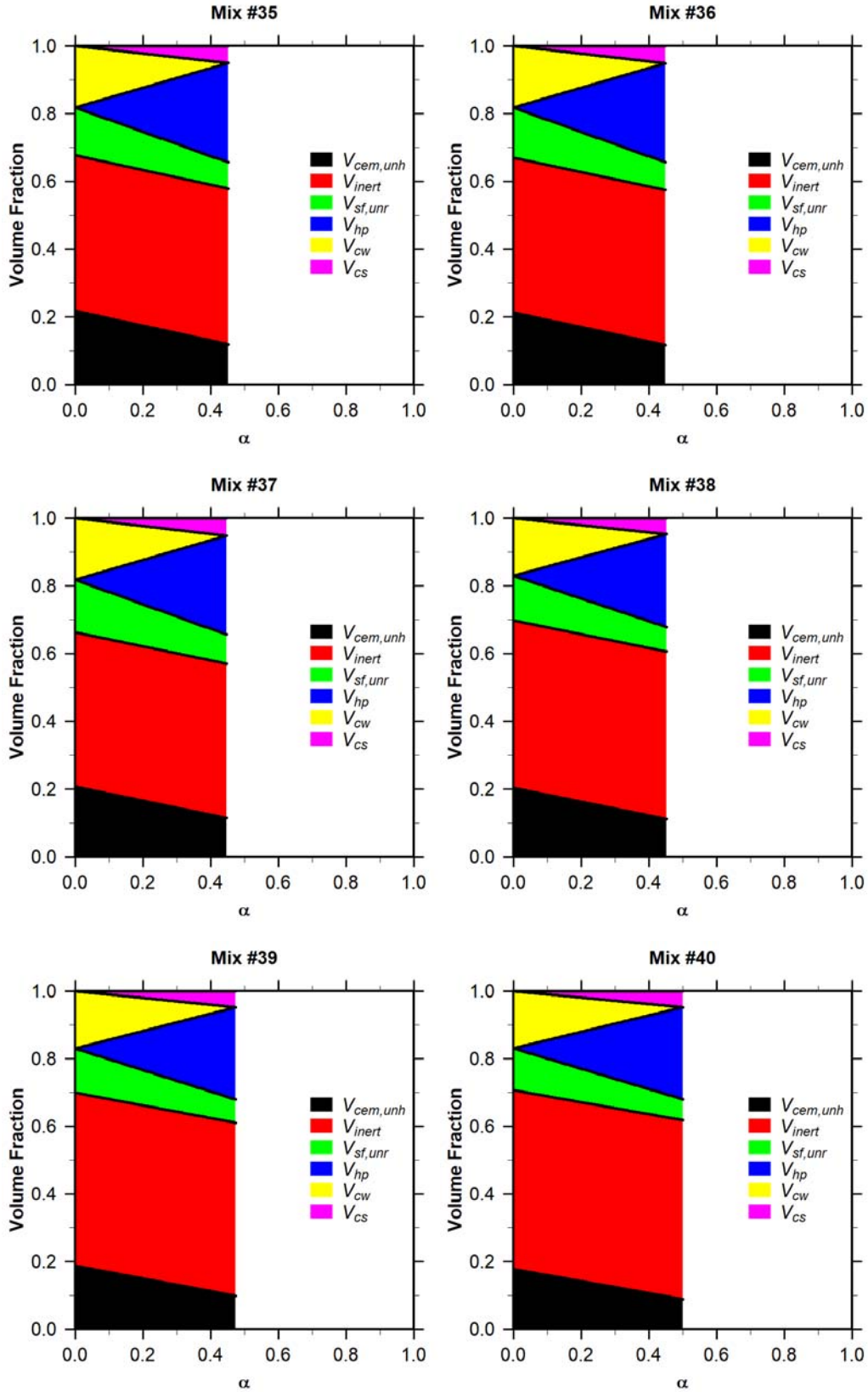


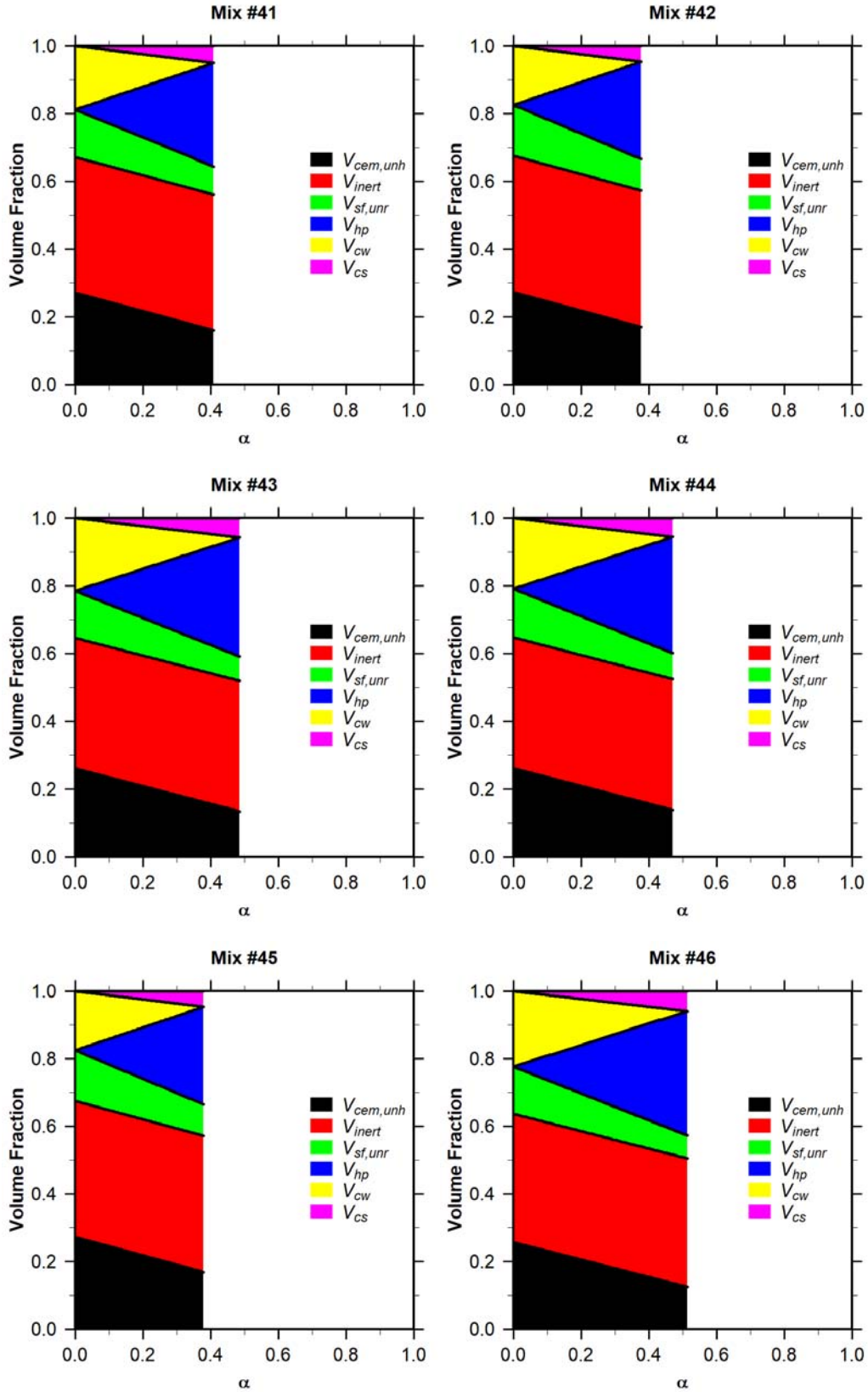


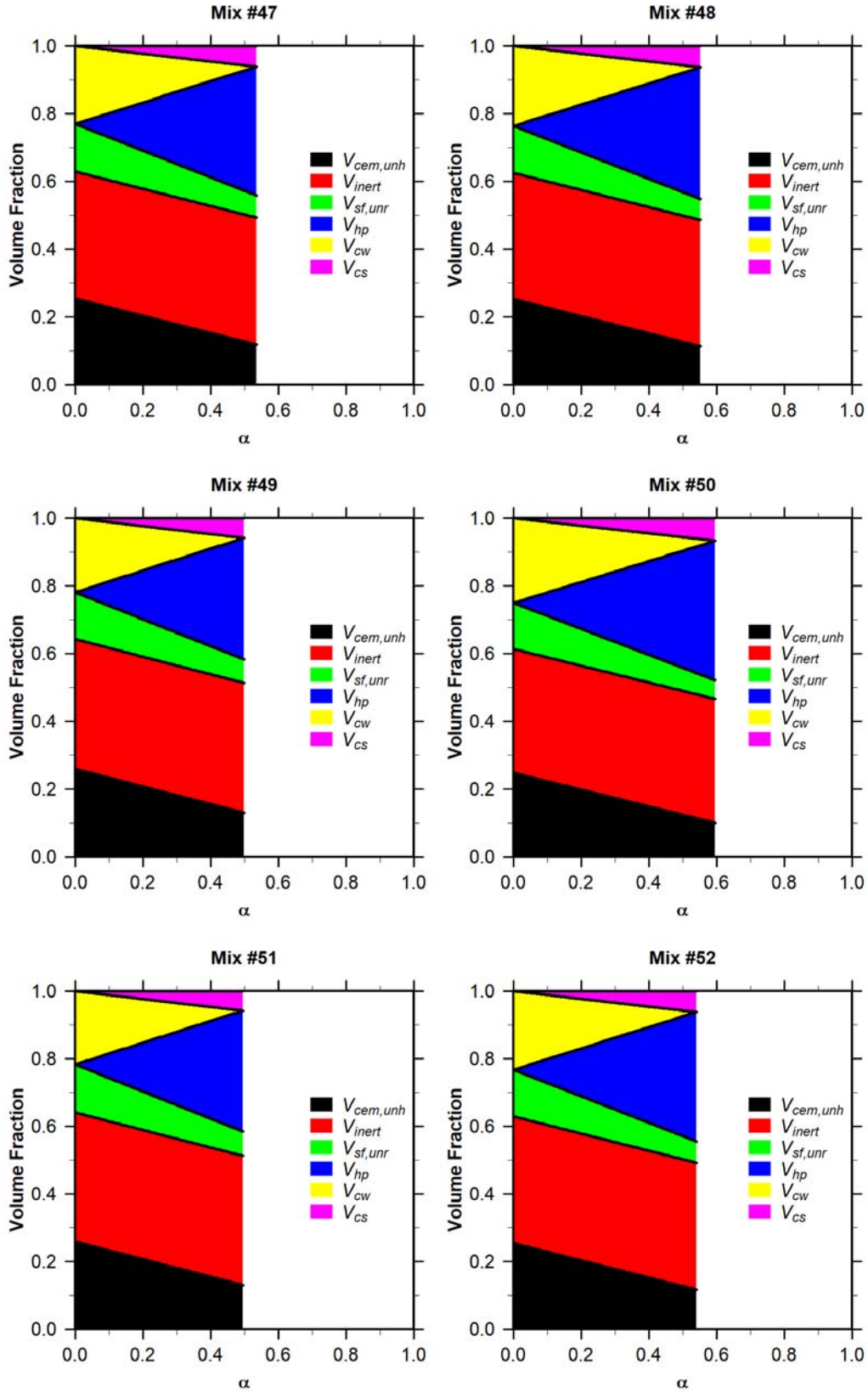


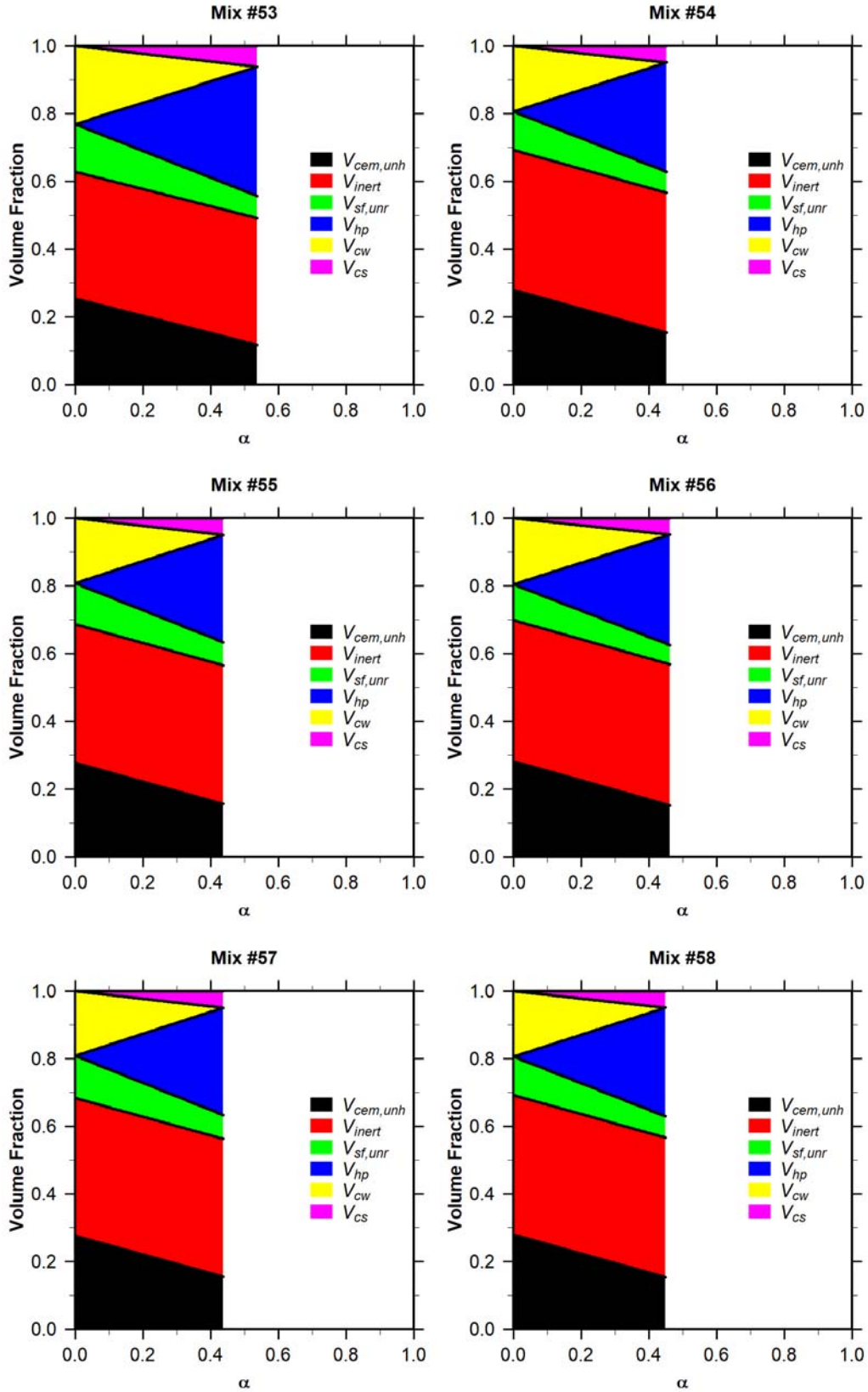


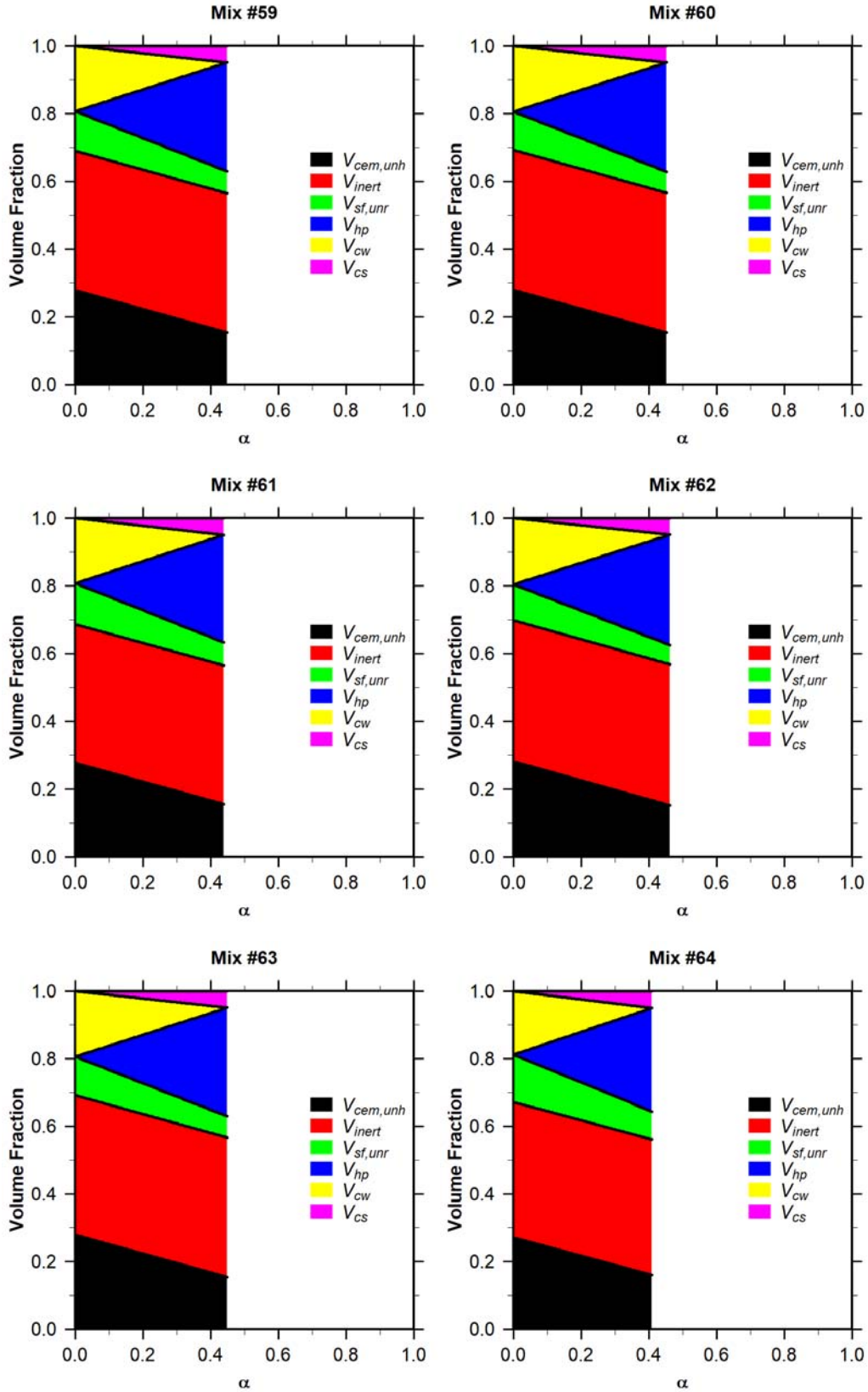


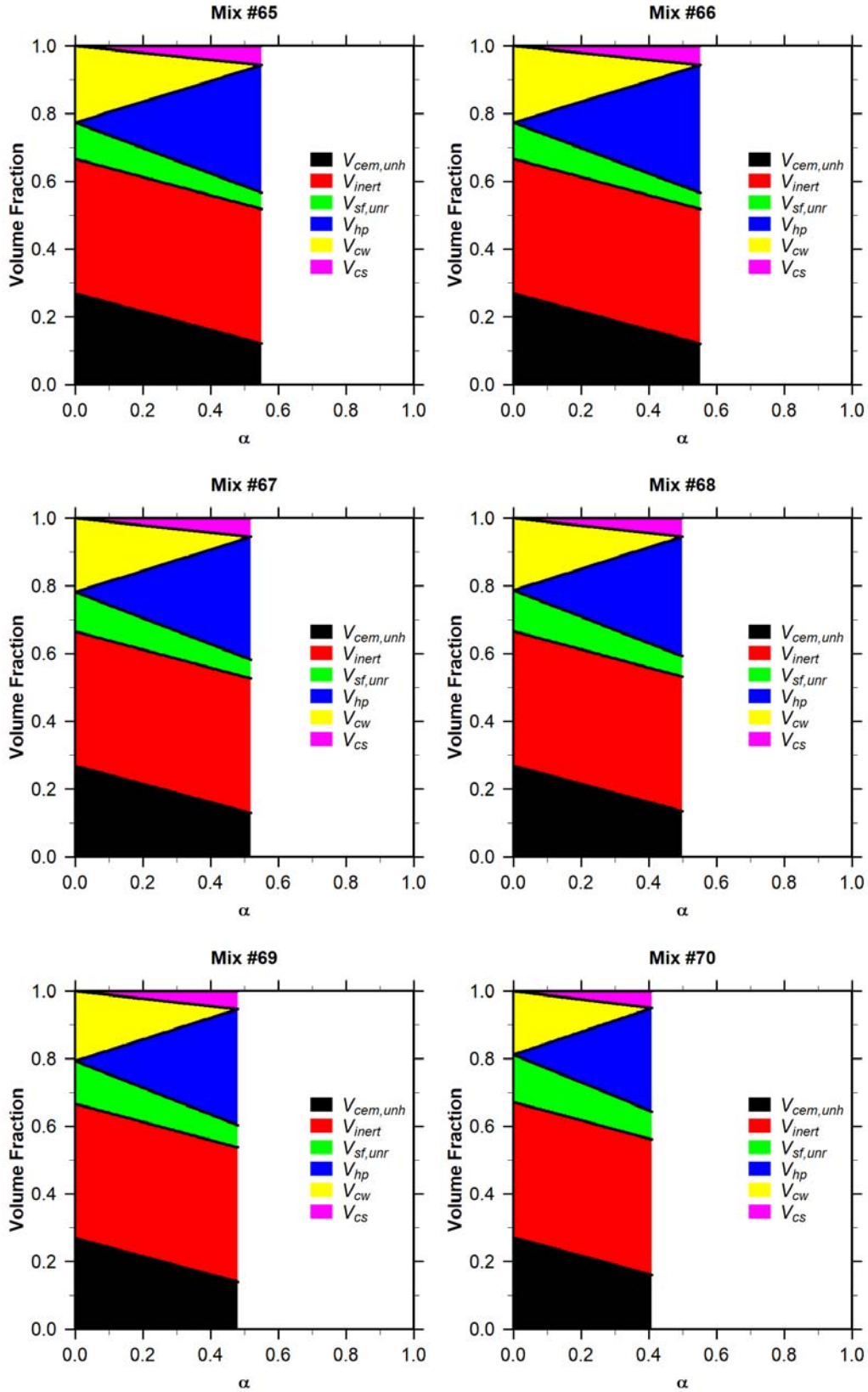


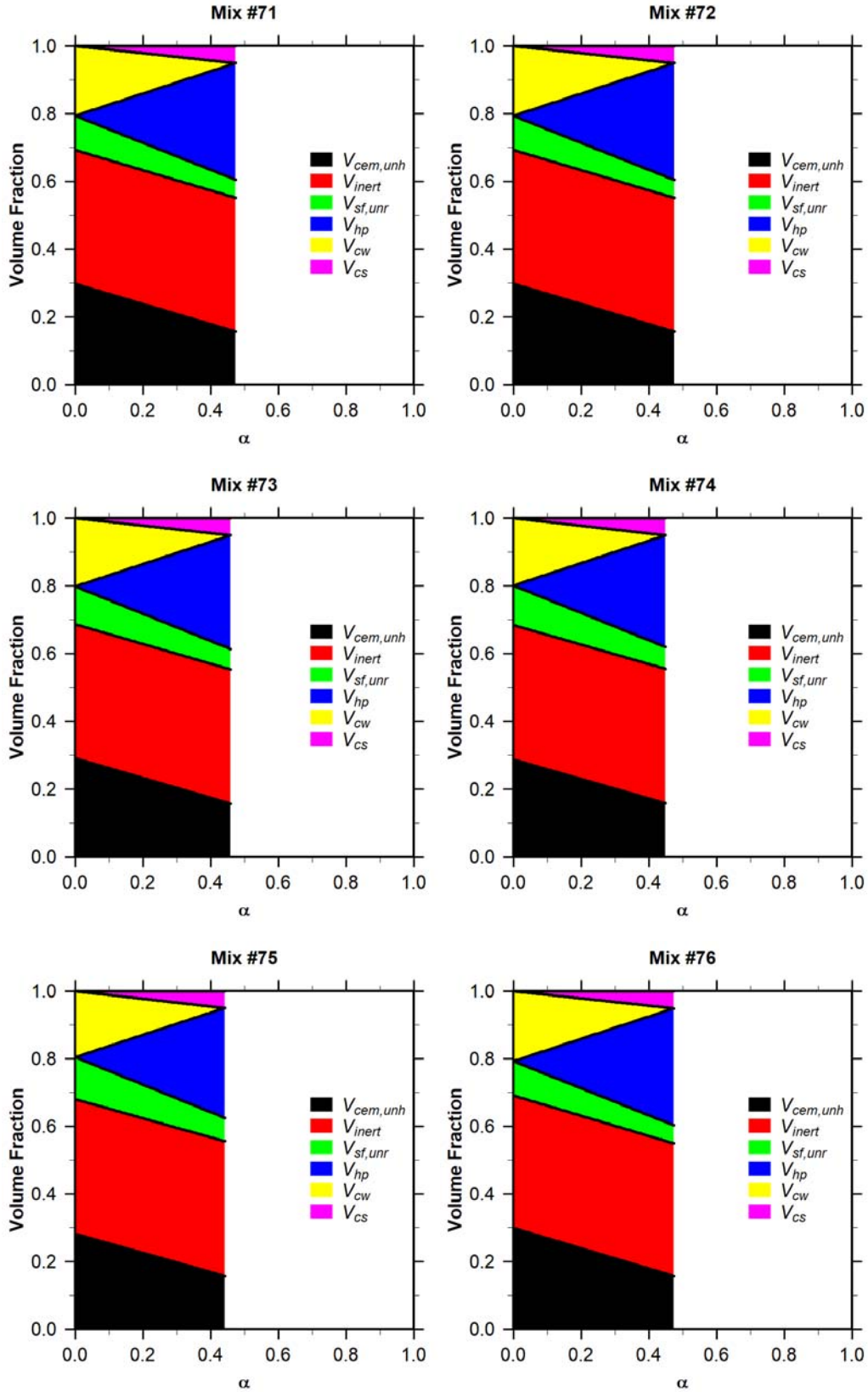


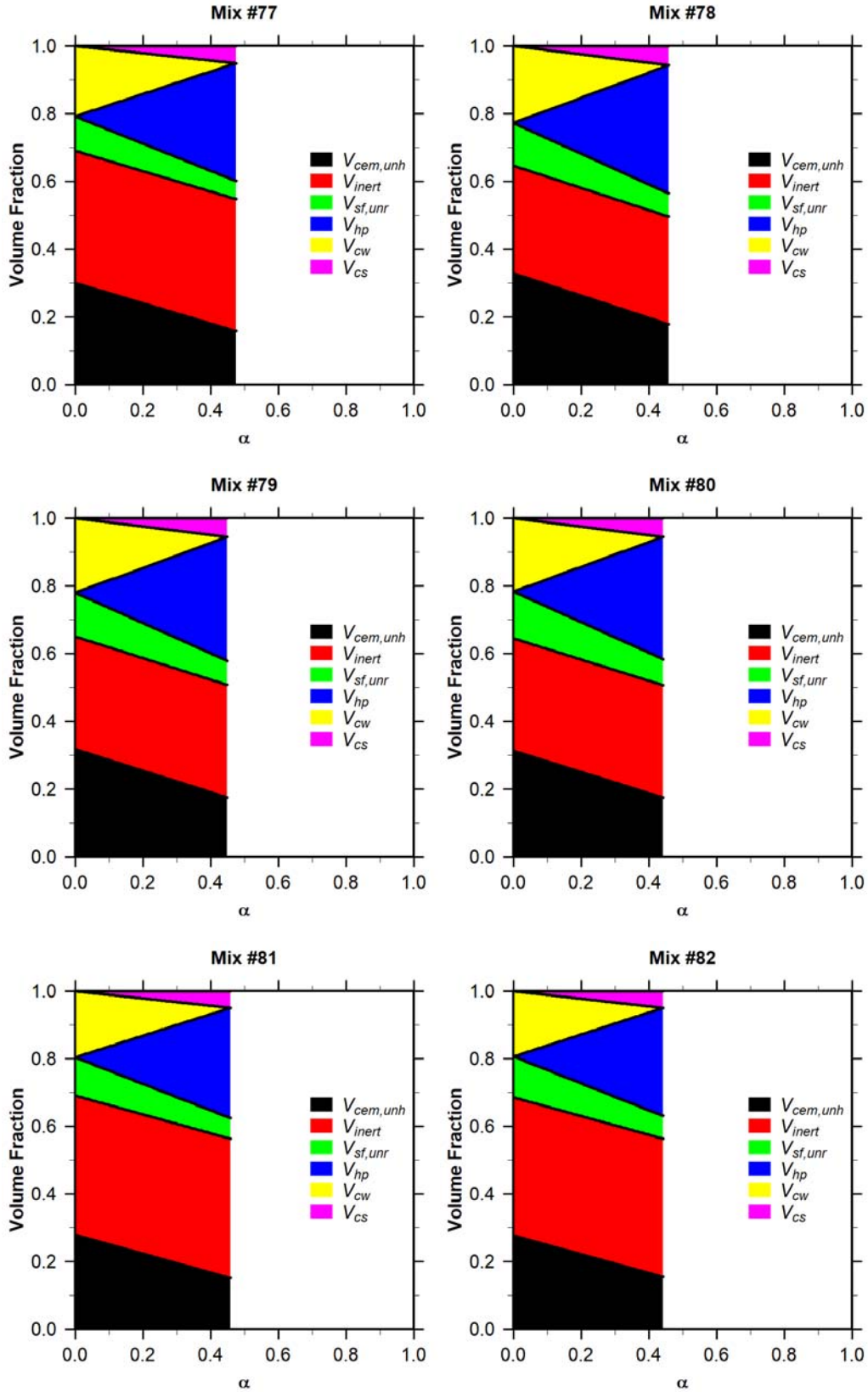












REFERENCES

- [1] ASTM International, "ASTM C1437-15 Standard Test Method for Flow of Hydraulic Cement Mortar," ASTM International, West Conshohocken, PA, 2015.
- [2] J. F. Burroughs, T. S. Rushing, D. A. Scott and B. A. Williams, "Analyzing Effects of Varied Silica Fume Sources within Baseline UHPC," in *Proceedings of the First International Interactive Symposium on UHPC*, Des Moines, IA, 2016.
- [3] American Concrete Institute, "ACI Concrete Terminology," American Concrete Institute, Farmington Hills, MI, 2016.
- [4] ACI Committee 234, "Guide for the Use of Silica Fume in Concrete," in *ACI Manual of Concrete Practice 2009*, C. R. Bischof, Ed., Farmington Hills, MI, American Concrete Institute, 2009, pp. 234R-1 - 234R-63.
- [5] C. Bernhardt, "SiO₂-Stov som Cementtilsetning (SiO₂ Dust as an Admixture to Cement)," *Betongen Idag*, vol. 17, no. 2, pp. 29-53, 1952.
- [6] A. Buck and J. Burkes, "Characterization and Reactivity of Silica Fume," in *3rd International Conference on Cement Microscopy, International Cement Microscopy Association*, Duncanville, TX, 1981.
- [7] T. Holland, A. Krysa, M. Luther and T. Liu, "Miscellaneous Paper SL-86-14 Abrasion-Erosion Evaluation of Concrete Mixtures for Still Basin Repairs, Kinzua Dam, Pennsylvania," U.S. Army Waterways Experiment Station, Vicksburg, Mississippi, 1986.
- [8] H. G. Russell and B. A. Graybeal, "Ultra-High Performance Concrete: A State-of-the-Art Report for the Bridge Community," Federal Highway Administration, McLean, VA, 2013.
- [9] Rasheeduzzafar and S. Hussain, "Effect of Microsilica and Blast Furnace Slag on Pore Solution Composition and Alkali-Silica Reaction," *Cement & Concrete Composites*, vol. 13, pp. 219-225, 1991.
- [10] A. Boddy, R. Hooton and M. Thomas, "The effect of the silica content of silica fume on its ability to control alkali-silica reaction," *Cement and Concrete Research*, vol. 33, pp. 1263-1268, 2003.

- [11] S. Whatley, P. Suraneni, V. Jafari Azad, O. Isgor and J. Weiss, "Mitigation of calcium oxychloride formation in cement pastes using undensified silica fume," *Journal of Materials in Civil Engineering*, vol. 29, no. 10, 2017.
- [12] L. Singh, A. Goel, S. Bhattacharyya, S. Ahalawat, U. Sharma and G. Mishra, "Effect of nanosilica on chloride permeability in cement mortar," *Advances in Cement Research*, vol. 27, no. 7, pp. 399-408, 2015.
- [13] V. Papadakis, "Experimental investigation and theoretical modeling of silica fume activity in concrete," *Cement and Concrete Research*, vol. 29, pp. 79-86, 1999.
- [14] J. Larbi, A. Fraay and J. Bijen, "The chemistry of the pore fluid of silica fume-blended cement systems," *Cement and Concrete Research*, vol. 20, pp. 506-516, 1990.
- [15] Z. Rong, W. Sun, H. Xiao and W. Wang, "Effect of silica fume and fly ash on hydration and microstructure evolution of cement based composites at low water-binder ratios," *Construction and Building Materials*, vol. 51, pp. 446-450, 2014.
- [16] J. Rossen, B. Lothenbach and K. Scrivener, "Composition of C-S-H in pastes with increasing levels of silica fume addition," *Cement and Concrete Research*, vol. 75, pp. 14-22, 2015.
- [17] A. Muller, K. Scrivener, J. Skibsted, A. Gajewicz and P. McDonald, "Influence of silica fume on the microstructure of cement pastes: new insights from ^1H NMR relaxometry," *Cement and Concrete Research*, vol. 74, pp. 116-125, 2015.
- [18] E. Kishar, D. Ahmed and M. Mohammed, "Hydration of portland cement in presence of silica fume," *Advances in Cement Research*, vol. 22, no. 3, pp. 143-148, 2010.
- [19] M.-H. Zhang and O. Gjorv, "Effect of silica fume on cement hydration in low porosity cement pastes," *Cement and Concrete Research*, vol. 21, pp. 800-808, 1991.
- [20] M. Sanjuan, C. Argiz, J. Galvez and A. Moragues, "Effect of silica fume fineness on the improvement of portland cement strength performance," *Construction and Building Materials*, vol. 96, pp. 55-64, 2015.
- [21] P. Suraneni and J. Weiss, "Examining the pozzolanicity of supplementary cementitious materials using isothermal calorimetry and thermogravimetric analysis," *Cement and Concrete Composites*, vol. 83, pp. 273-278, 2017.

- [22] T. Oertel, F. Hutter, U. Helbig and G. SEXTL, "Amorphous silica in ultra-high performance concrete: first hour of hydration," *Cement and Concrete Research*, vol. 58, pp. 131-142, 2014.
- [23] G. Quercia, A. Lazaro, J. Geus and H. Brouwers, "Characterization of morphology and texture of several amorphous nano-silica particles used in concrete," *Cement & Concrete Composites*, no. 44, pp. 77-92, 2013.
- [24] L. Singh, A. Goel, S. Bhattacharyya, U. Sharma and G. Mishra, "Hydration Studies of Cementitious Materials using Silica Nanoparticles," *Journal of Advanced Concrete Technology*, vol. 13, pp. 345-354, 2015.
- [25] M. Davraz and L. Gunduz, "Engineering properties of amorphous silica as a new natural pozzolan for use in concrete," *Cement and Concrete Research*, vol. 35, pp. 1251-1261, 2005.
- [26] N. Neithalath, J. Persun and A. Hossain, "Hydration in high-performance cementitious systems containing vitreous calcium aluminosulfate or silica fume," *Cement and Concrete Research*, no. 39, pp. 473-481, 2009.
- [27] M. Vandamme, F.-J. Ulm and P. Fonollosa, "Nanogranular packing of C-S-H at substoichiometric conditions," *Cement and Concrete Research*, vol. 40, pp. 14-26, 2010.
- [28] D.-Y. Lei, L.-P. Guo, W. Sun, J. Liu and X.-L. Guo, "A new dispersing method on silica fume and its influence on the performance of cement-based materials," *Construction and Building Materials*, vol. 115, pp. 716-726, 2016.
- [29] Z. Wu, C. Shi and K. Khayat, "Influence of silica fume content on microstructure development and bond to steel fiber in ultra-high strength cement-based materials," *Cement and Concrete Composites*, vol. 71, pp. 97-109, 2016.
- [30] Z. Zhang, B. Zhang and P. Yan, "Comparative study of effect of raw and densified silica fume in the paste, mortar and concrete," *Construction and Building Materials*, vol. 105, pp. 82-93, 2016.
- [31] Z. Zhang, B. Zhang and P. Yan, "Hydration and microstructures of concrete containing raw or densified silica fume at different curing conditions," *Construction and Building Materials*, vol. 121, pp. 483-490, 2016.

- [32] T. C. Powers and T. L. Brownyard, "Studies on the physical properties of hardened portland cement paste," *Bulletin*, vol. 22, 1948.
- [33] P. Lura, O. M. Jensen and K. van Breugel, "Autogenous shrinkage in high-performance cement paste: an evaluation of basic mechanisms," *Cement and Concrete Research*, vol. 33, pp. 223-232, 2003.
- [34] K. Habel, M. Viviani, E. Denarie and E. Bruhwiler, "Development of the mechanical properties of an ultra-high performance fiber reinforced concrete (UHPFRC)," *Cement and Concrete Research*, vol. 36, pp. 1362-1370, 2006.
- [35] V. Jafari Azad, P. Suraneni, O. B. Isgor and W. J. Weiss, "Interpreting the pore structure of hydrating cement phases through a synergistic use of the Powers-Brownyard model, hydration kinetics, and thermodynamic calculations," *Advances in Civil Engineering Materials*, vol. 6, no. 1, pp. 1-16, 2017.
- [36] X.-Y. Wang, "Properties prediction of ultra high performance concrete using blended cement hydration model," *Construction and Building Materials*, vol. 64, pp. 1-10, 2014.
- [37] J. Yajun and J. Cahyadi, "Simulation of silica fume blended cement hydration," *Materials and Structures*, vol. 37, pp. 397-404, 2004.
- [38] ASTM International, "ASTM C143/C143M-15a Standard Test Method for Slump of Hydraulic-Cement Concrete," ASTM International, West Conshohocken, PA, 2015.
- [39] ASTM International, "ASTM C939/C939M-16a Standard Test Method for Flow of Grout for Preplaced-Aggregate Concrete (Flow Cone Method)," ASTM International, West Conshohocken, PA, 2015.
- [40] C. F. Ferraris and F. de Larrard, "Modified Slump Test to Measure Rheological Parameters of Fresh Concrete," *Cement, Concrete, and Aggregates*, vol. 20, no. 2, pp. 241-247, 1998.
- [41] M. Nehdi and M.-A. Rahman, "Estimating rheological properties of cement pastes using various rheological models for different test geometry, gap and surface friction," *Cement and Concrete Research*, vol. 34, pp. 1993-2007, 2004.
- [42] L. Senff, D. Hotza, W. Repette, V. Ferreira and J. Labrincha, "Rheological characterisation of cement pastes with nanosilica, silica fume and superplasticizer additions," *Advances in Applied Ceramics*, vol. 109, no. 4, pp. 213-218, 2010.

- [43] C. F. Ferraris, "Measurement of rheological properties of cement paste: a new approach," in *Proceedings of Role of Admixtures in High Performance Concrete, RILEM International Symposium*, Monterey, Mexico, 1999.
- [44] G. Mei, H. Yang and C. Lu, "Coupled effects of silica fume and time after water addition on rheology of fresh concrete," *Magazine of Concrete Research*, vol. 67, no. 14, pp. 762-770, 2015.
- [45] A. Kwan and H. Wong, "Effects of packing density, excess water and solid surface area on flowability of cement paste," *Advances in Cement Research*, vol. 20, no. 1, pp. 1-11, 2008.
- [46] J. Chen, W. Fung and A. Kwan, "Effects of CSF on strength, rheology and cohesiveness of cement paste," *Construction and Building Materials*, no. 35, pp. 979-987, 2012.
- [47] G. Lu, K. Wang and T. J. Rudolphi, "Modeling rheological behavior of highly flowable mortar using concepts of particle and fluid mechanics," *Cement and Concrete Composites*, vol. 30, pp. 1-12, 2008.
- [48] H. Vikan, H. Justnes, F. Winnefeld and R. Figi, "Correlating cement characteristics with rheology of paste," *Cement and Concrete Research*, vol. 37, pp. 1502-1511, 2007.
- [49] A. Mohammed, "Vipulanandan model for the rheological properties with ultimate shear stress of oil well cement modified with nanoclay," *Egyptian Journal of Petroleum*, vol. 27, no. 3, pp. 335-347, 2018.
- [50] C. Vipulanandan and A. Mohammed, "Rheological properties of piezoresistive smart cement slurry modified with iron-oxide nanoparticles for oil-well applications," *Journal of Testing and Evaluation*, vol. 45, no. 6, pp. 2050-2060, 2017.
- [51] M. Benaicha, X. Roguiez, O. Jalbaud, Y. Burtschell and A. Alaoui, "Influence of silica fume and viscosity modifying agent on the mechanical and rheological behavior of self compacting concrete," *Construction and Building Materials*, vol. 84, pp. 103-110, 2015.
- [52] J. Plank, C. Schroefl, M. Gruber, M. Lesti and R. Sieber, "Effectiveness of Polycarboxylate Superplasticizers in Ultra-High Strength Concrete: The Importance of PCE Compatibility with Silica Fume," *Journal of Advanced Concrete Technology*, vol. 7, no. 1, pp. 5-12, 2009.

- [53] H. Vikan and H. Justnes, "Rheology of cementitious paste with silica fume or limestone," *Cement and Concrete Research*, vol. 37, pp. 1512-1517, 2007.
- [54] A. Kwan, W. Fung and H. Wong, "Water film thickness, flowability and rheology of cement-sand mortar," *Advances in Cement Research*, vol. 22, no. 1, pp. 3-14, 2010.
- [55] L. G. Li and A. K. Kwan, "Concrete mix design based on water film thickness and paste film thickness," *Cement & Concrete Composites*, vol. 39, pp. 33-42, 2013.
- [56] K. Wille, A. E. Naaman and G. J. Parra-Montesinos, "Ultra-High Performance Concrete with Compressive Strength Exceeding 150 MPa (22 ksi): A Simpler Way," *ACI Materials Journal*, vol. 108, no. 1, pp. 46-54, 2011.
- [57] Z. Wu, K. H. Khayat and C. Shi, "Changes in rheology and mechanical properties of ultra-high performance concrete with silica fume content," *Cement and Concrete Research*, vol. 123, 2019, in press.
- [58] K. Wille and C. Boisvert-Cotulio, "Material efficiency in the design of ultra-high performance concrete," *Construction and Building Materials*, vol. 86, pp. 33-43, 2015.
- [59] M. Alkaysi and S. El-Tawil, "Effects of variations in the mix constituents of ultra high performance concrete (UHPC) on cost and performance," *Materials and Structures*, vol. 49, pp. 4185-4200, 2016.
- [60] ASTM International, "ASTM C150/C150M-19a Standard Specification for Portland Cement," ASTM International, West Conshohocken, PA, 2019.
- [61] ASTM International, "ASTM C1240 Standard Specification for Silica Fume Used in Cementitious Mixtures," ASTM International, West Conshohocken, PA, 2015.
- [62] ASTM International, "ASTM D4254-16 Standard Test Methods for Minimum Index Density and Unit Weight of Soils and Calculation of Relative Density," ASTM International, West Conshohocken, PA, 2016.
- [63] ASTM International, "ASTM C1069-09(2014) Standard Test Method for Specific Surface Area of Alumina or Quartz by Nitrogen Adsorption," ASTM International, West Conshohocken, PA, 2014.

- [64] ASTM International, "ASTM C204-18e1 Standard Test Methods for Fineness of Hydraulic Cement by Air-Permeability Apparatus," ASTM International, West Conshohocken, PA, 2018.
- [65] ASTM International, "ASTM C127-15 Standard Test Method for Relative Density (Specific Gravity) and Absorption of Coarse Aggregate," ASTM International, West Conshohocken, PA, 2015.
- [66] ASTM International, "ASTM C128-15 Standard Test Method for Relative Density (Specific Gravity) and Absorption of Fine Aggregate," ASTM International, West Conshohocken, PA, 2015.
- [67] H. Brouwers, "The work of Powers and Brownyard revisited: Part 1," *Cement and Concrete Research*, vol. 34, pp. 1697-1716, 2004.
- [68] ASTM International, "Standard Specification for Portland Cement," ASTM International, West Conshohocken, PA, 2019.
- [69] ASTM International, "ASTM C114-18 Standard Test Methods for Chemical Analysis of Hydraulic Cement," ASTM International, West Conshohocken, PA, 2018.
- [70] P. Stutzman, A. Heckert, A. Tebbe and S. Leigh, "Uncertainty in Bogue-calculated phase composition of hydraulic cements," *Cement and Concrete Research*, Vols. 61-62, pp. 40-48, 2014.
- [71] ASTM International, "ASTM C109/C109M-16a Standard Test Method for Compressive Strength of Hydraulic Cement Mortars (Using 2-in. or [50-mm] Cube Specimens)," ASTM International, West Conshohocken, PA, 2016.
- [72] ASTM International, "ASTM C1749-17a Standard Guide for Measurement of the Rheological Properties of Hydraulic Cementitious Paste Using a Rotational Rheometer," ASTM International, West Conshohocken, PA, 2017.
- [73] M. Cyr, C. Legrand and M. Mouret, "Study on the shear thickening effect of superplasticizers on the rheological behaviour of cement pastes containing or not mineral additives," *Cement and Concrete Research*, vol. 30, no. 9, pp. 1477-1483, 200.